Properties and applications of copper halide-chalcogenoether and -chalcogenone networks and functional materials

Adrien Schlachter, Pierre Harvey

Properties and Applications of Copper Halide-Chalcogenoether and -Chalcogenone Networks and Functional Materials

*Adrien Schlachter and Pierre D. Harvey**

Département de chimie, Université de Sherbrooke, Sherbrooke, PQ, Canada, J1K 2R1.

Graphic Art

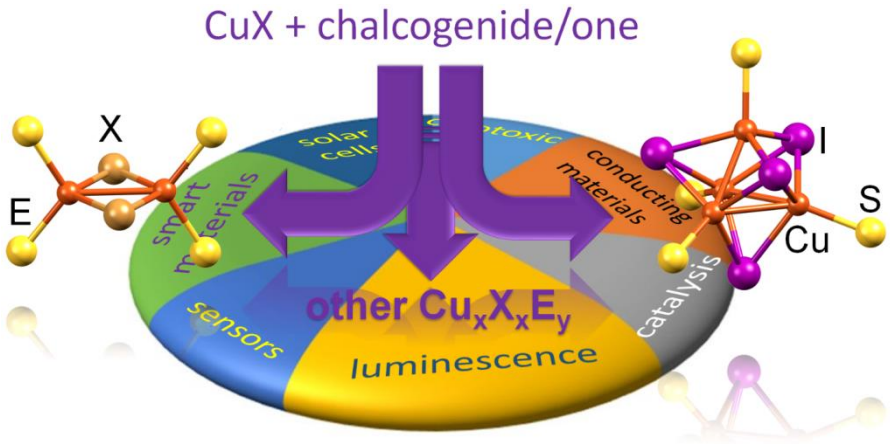

ABSTRACT: When copper(I) halide salts react with various mono- and poly-chalcogenoether and -chalcogenone ligands, two general shapes of neutral polynuclear $Cu_xX_xE_y$ species (E = S, Se, Te; X = Cl, Br, I; x = 2-8) are formed within the resulting 0-3D coordination materials. These polymetallic forms exhibit either *globular* and *quasi-planar* motifs, mainly closed cubane $Cu_4I_4S_4$ and rhomboid $Cu_2X_2S_4$, respectively, but not exclusively. Depending on the shape of these polynuclear species and the dimensionality of the network, their properties and applications are profoundly different. These materials include luminescent and electroactive materials, small molecules sensing, thermo-, electro- and photocatalysts, therapeutic and antibacterial species, electrically conducting solids, solar cells and light emitting diodes, and functional and stimuli-responsive materials (such as self-healing). Specific properties such as occurrence of solid-to-solid phase transition and thermo- and mechano-chromism have also been observed. This work summarizes these properties and applications and presents their current research directions.

TABLE OF CONTENT

1. INTRODUCTION

The early investigations of Ford and his collaborators on the luminescent cubane-shaped $Cu_4I_4L_4$ clusters and some related derivatives (L = N- and P-donor ligand),[1] which was also concurrently expanded to hydroxo-derivatives (*i.e.* X = OH),[2] readily motivated many other research groups to explore the design of new $Cu_xX_xL_y$ species, notably for X = Cl, Br, I, x = 2 to 8, and $4 < y < 8$. The particularly intense luminescence properties, namely for the copper iodide-based salt, were extensively exploited to design a large range of stimuli-responsive, functional and smart materials. These materials are built with upon both discrete clusters and complexes (0D-) and coordination polymers (1D-, 2D-, 3D-). The Cu_xX_x cores are often called secondary building units (SBUs) inside the coordination polymers.[3–5] Indeed, the occasionally observed large emission quantum yields permitted the fabrication of light emitting diodes (OLED), including white OLED.[4] The design of stimuli-responsive luminescent materials, induced by a change in temperature and pressure, is often driven by the adaptability of the skeleton of the $Cu_xX_xL_y$ central species, often accompanied by a change in Cu•••Cu distances. This phenomenon is well known for the $Cu_4I_4L_4$ clusters where the two extreme geometries, *stella quadrangular* and *closed cubane*, have been observed by X-ray crystallography and are directly linked to their corresponding photophysical properties (**Figure 1**).[1] Beside these two stimuli-driven properties, light- (*i.e.* upon irradiation), solvato- (or vapor-), and mechano-chromic materials were also reported.[4,5] In the cases of coordination polymers, such changes in luminescence responses can be induced or accompanied by a solid-to-solid phase transition.[4] In addition, the design of nanomaterials and composites was also performed.[5]

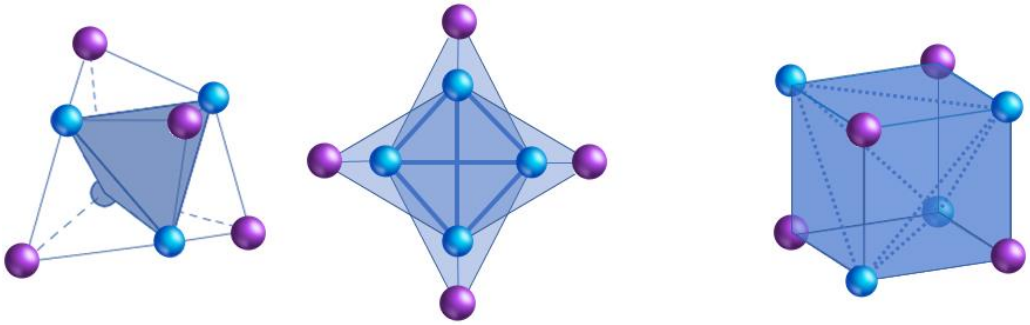

stella quadrangular *closed cubane*

Figure 1. Representations of the two extreme cases of SBU geometry for the $Cu_4I_4L_4$ SBU.

The obvious extension of the $Cu_xX_xL_y$-based functional materials is for L = S-donor (*i.e.* thioethers or a thione), Se- and Te-donor ligands. Their emergence is rather recent (**Figure 2**), but nonetheless, they exhibit rich electronic, opto-electronic, redox, and mechanical properties, as their main traits are their rich emission and electrochemical activities. Hence, the design of a large brochette of new functional materials have also been recently investigated, namely during the past decade. Moreover, many cytotoxicity studies have also been reported showing a good activity. Quite remarkably, while both P- and S-donors are considered *soft* ligands, this similitude stops here as the resulting structures of their SBUs, and the dimensionality of the coordination polymers differ quite significantly. Indeed for the P-donor ligands, the resulting SBU geometry consists largely of the closed $Cu_4I_4P_4$ cubane, whereas the S-donor-containing materials exhibit quite a large spread of SBU motifs based on a recent series of structural surveys conducted by us.[6–8] Several examples involving the CuI salt are provided in **Figure 3**. In addition, the $Cu_xX_xP_y$ species (X = Cl, Br, I) are overwhelmingly reported as 0D complexes, whereas the $Cu_xX_xS_y$ species (X = Cl, Br, I) are mostly found within coordination polymers, mainly 1D- and 2D-materials.[6–8] Consequently, these major differences in SBU geometries and network structures lead inevitably to significant differences in SBU-based properties in the solid state such as electric conductivity and mechanical properties for examples.

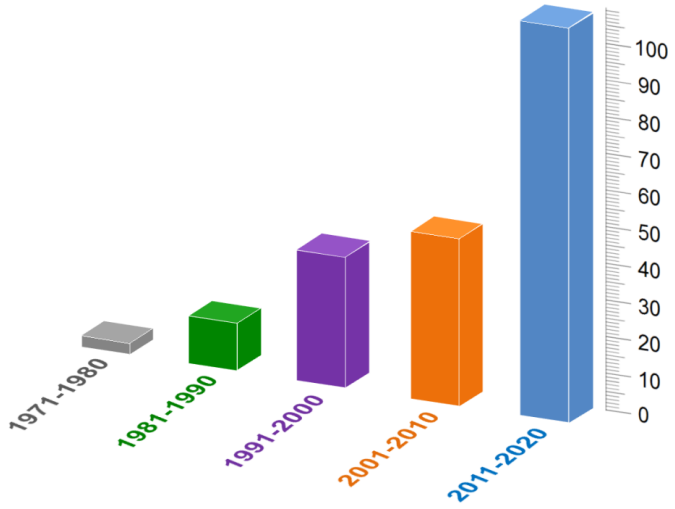

Figure 2. Time evolution of the number of articles reporting the chemistry of the $Cu_xX_xS_y$ (X = Cl, Br, I) complexes and coordination polymers species built upon chalcogenoethers and chalcogenones .

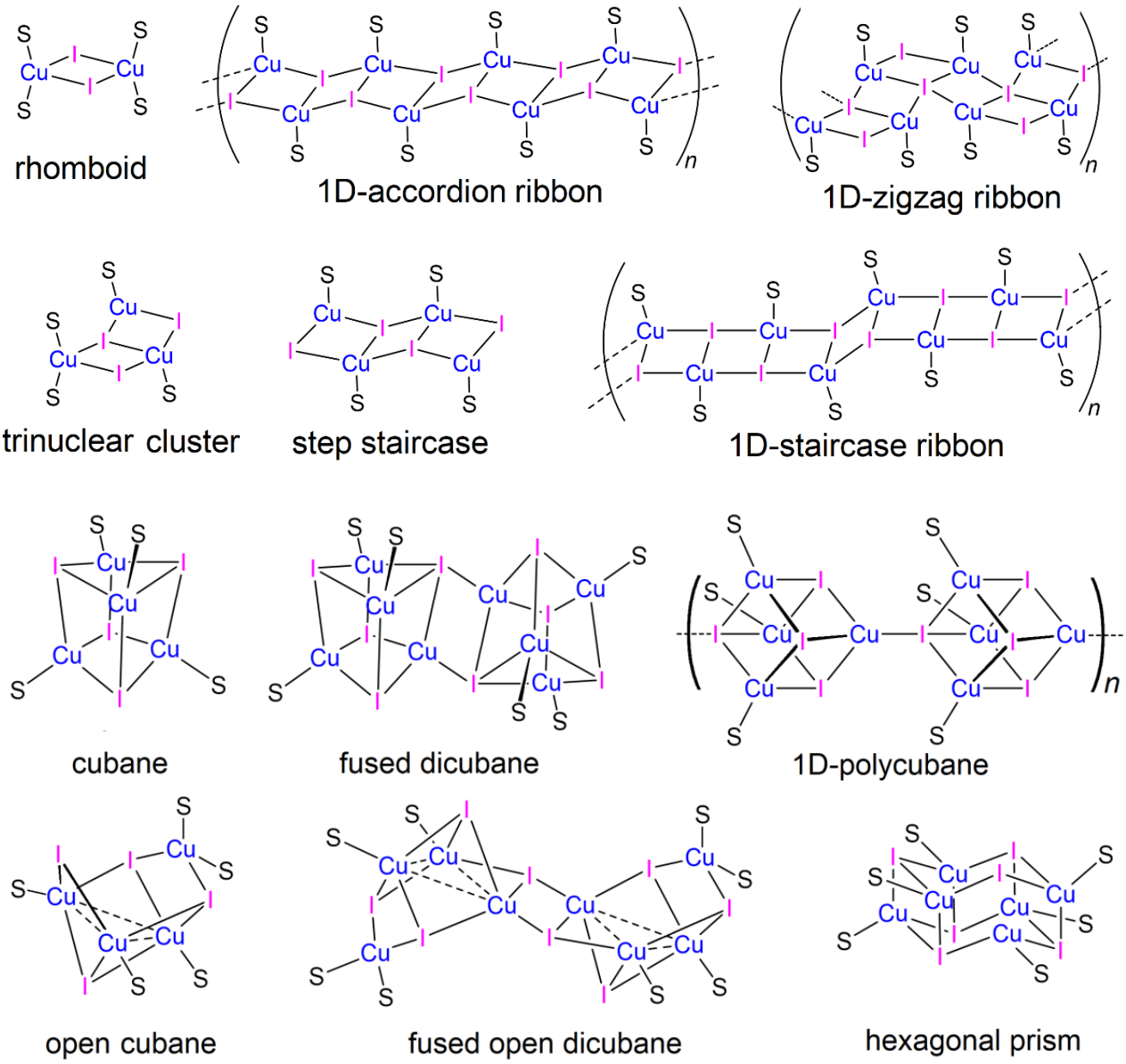

Figure 3. Structures of the various SBUs or 0D complexes encountered for neutral $Cu_xI_xS_y$ motifs; top, *quasi-planar*, bottom, *globular*. Note that this list is not exhaustive.

This review describes and analyses the properties and applications of functional materials issued from the emerging $Cu_xX_xE_y$-based chemistry (X = Cl, Br, I; E = S-, Se-, Te-donor ligands; x = 2-8; $4 < y < 8$). Examples of applications include small molecules sensing, thermo-, electro- and photo-catalysis, therapeutic and antibacterial activities, electrical conductivity, solar cells and light emitting diodes, and as self-healing and stimuli-responsive materials.

2. Properties of the $Cu_xX_xE_y$-containing complexes and Coordination polymers

The list of ligands and codes employed throughout this review is provided in **Figure 4**.

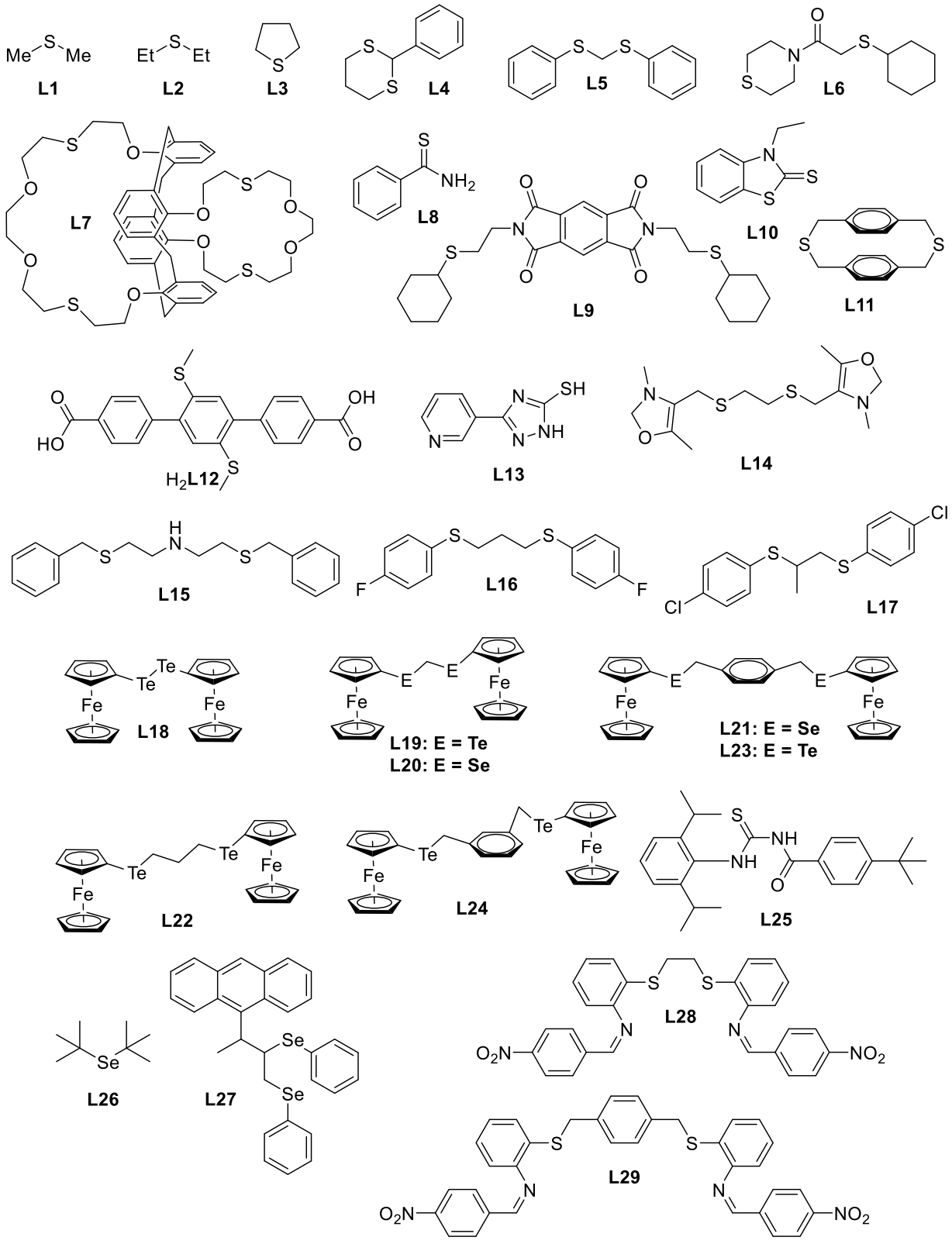

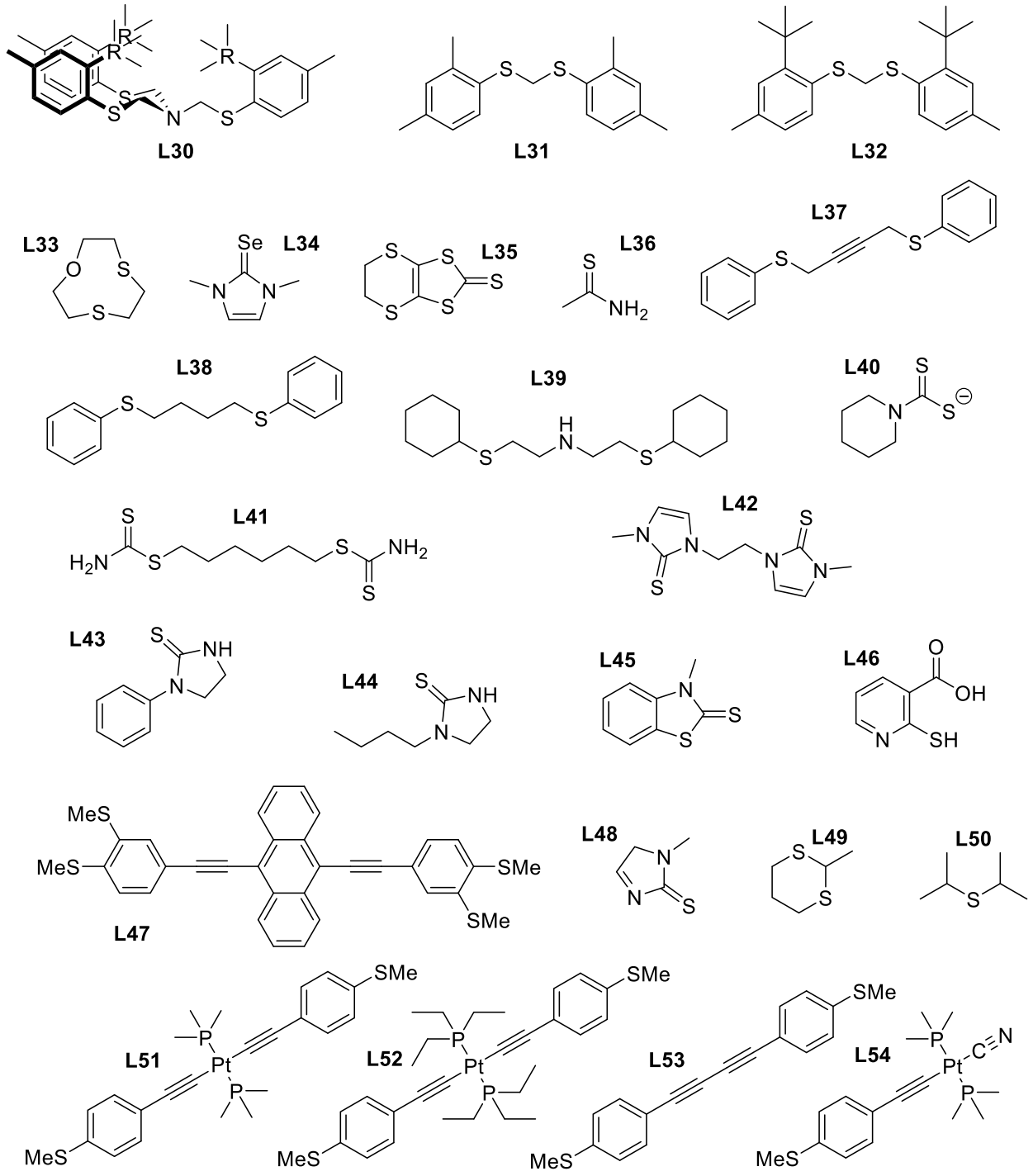

Figure 4. Structures and codes of ligands used in this review.

2.1. Formation of emissive $Cu_xI_xS_y$ species at the CuI crystal surface

Pike *et al.* reported the adsorption of various small thioether and amine molecules, including Me_2S (**L1**), Et_2S (**L2**) and tetrahydrothiophene, THT (**L3**), onto γ-CuI films and examined the emission response of the surface modified materials at 298 and 77 K.[9] The emission colors (**Figure 5a**) and spectra data (**Figure 5b**, **Table 1**) clearly differ depending on the thioether. The authors made a primary tentative to link the emission spectra of these modified surfaces and the observed emission properties generally encountered from neutral $Cu_xI_xS_y$ species. Namely between closed cubanes, which are often characterized by a high and a low energy emission bands and large Stokes shifts, and from stair step polymers. Scanning electron microscopy and optical microscopy of unexposed and exposed γ-CuI films indicated that the film thicknesses were approximately 1 μm and exhibited nearly continuous film coverage. The comparison of the powder X-ray diffraction (PXRD) patterns before and after exposures revealed a difference in the CuI surface morphology where some degree of crystallinity was lost, presumably due to a recrystallization upon CuI binding. This trait readily indicates that the observed phenomena was a surface one. Their initial interpretation was that the emissive species were different than the commonly encountered $Cu_4I_4S_4$ cubane, and most likely of larger dimension, and that computer modeling was necessary to understand these phenomena. This hypothesis is plausible because emissive $Cu_xI_xS_y$ species may also be of various motifs different from the common $Cu_4I_4S_4$ cubane as shown in **Figure 3**. Subsequently, this same group has indeed studied the adsorption of **L1** onto CuI and CuI/AgI nanoparticles (diameters varying from 18 ± 3 to 45 ± 6 Å) and performed computational studies on cation terminated surfaces (**Figure 5c**).[10] The result is that Me_2S (**L1**) was able to penetrate the surface and be embedded under a layer of CuI. The initial process involved the adsorption of **L1** onto the surface, followed by the displacement of substrate atom by **L1** (embedding) thus corresponding to an intermediary state (**Figure 5d**), and the formation of the final species at the surface as Cu_4I_4(**L1**)$_3$ identified by the comparison of the PXRD patterns with an authentic sample.

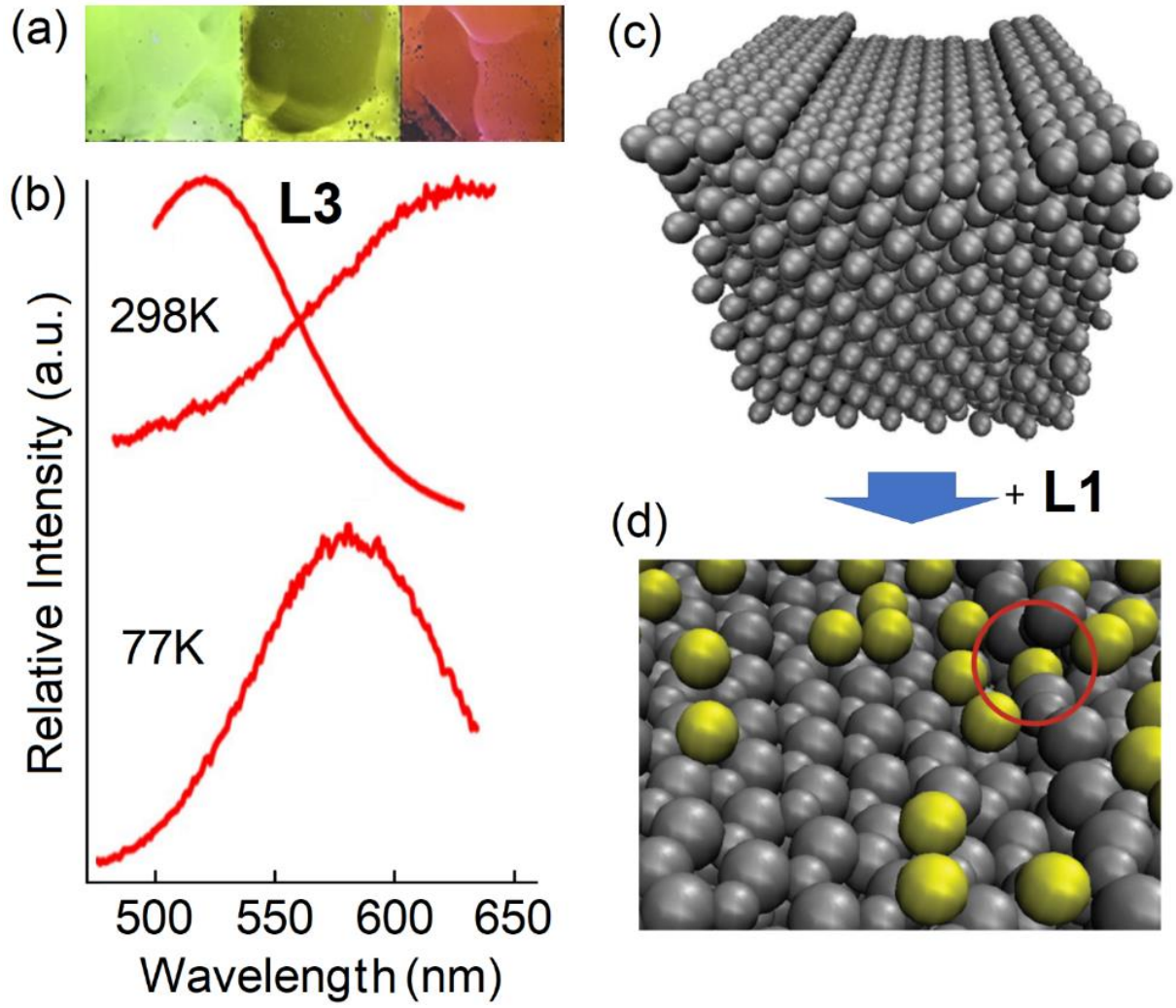

Figure 5. (a) Photograph of CuI films on a glass previously exposed to vapors of **L1** (left), **L2** (middle), and **L3** (right) under UV-irradiation (365 nm). (b) Emission spectra of CuI films (previously exposed to vapors of **L3**) at 298 and 77 K (λ_{exc} = 365 nm). (c) Model used to perform the molecular dynamic study of a homometallic (111) surface of γ-CuI containing 2436 cation sites and two steps to address the **L1** adsorption. All atoms are in grey color. (d) Results from the simulation calculations where a **L1** molecule is embedded into the surface of a surface step (red circle). The sulfur atoms are yellow, and the Me groups are not shown for simplicity. The other atoms are in grey color. Adapted with the permissions from *Inorg. Chem. Commun.*, 2014, **40**, 18–2,[9] and from *Phys. Chem. Chem. Phys.*, 2020, **22**, 11296–11306.[10] Copyright (2014) with permission of Elsevier. Copyright (2020) Royal Chemical Society.

It was also interesting to note that the process was accelerated when the nanoparticles incorporated AgI. The PXRD indicated that the lattice structure was not dramatically perturbed. However, one suspects that because of the difference in cation radii (0.91 *vs* 1.29 Å), defaults in the surface steps are created thus allowing for faster embedding. It is noteworthy that the crystal structures of the Ag-S linked of $[Ag_4I_4(\mathbf{L3})_4]$[11,12] is known, but there was no evidence for Ag- or AgCu-containing products. This is consistent with the fact that these species such as $Ag_2I_2S_4$ rhomboids[13,14] and polymeric $Ag_xI_xS_x$,[15] as well as their heterobimetallic hybrids,[16] are extremely rare.

Table 1. Luminescence data of the CuI-adducts of **L1**, **L2**, and **L3**.[9]

	298 K			77 K		
	λ_{exc}, nm	λ_{emi}, nm	Stokes, cm^{-1}	λ_{exc}, nm	λ_{emi}, nm	Stokes, cm^{-1}
L1	308	546				
L2	326	590				
L3	336	530 620	10 900 13 600	330	582	13 100

Note that these λ_{emi} values are consistent to what is generally observed for $Cu_4I_4S_4$ cubanes.

These basic investigations may have some incidence on the understanding of the possible primary steps of heterogeneous catalysis involving CuI and thioethers, as well as those occurring in homogenous media, such as those described below.

2.2. Solid-to-solid phase transition

The solid-to-solid phase transitions are processes that respond to changes mainly in temperature or pressure. A recent example includes the seemingly non-emissive 1D coordinated polymer $[Cu_2I_2(CH_3CN)_2(\mathbf{L4})]_n$ (**L4** = 2-phenyl-1,3-dithiane; **Figure 6**).[17] The X-ray structure was investigated at different temperatures between 100 and 300 K, and between 200 and 250 K, a phase transition resulting in change of the space group from triclinic $P\bar{1}$ to monoclinic $P2_1/m$, was observed. This process is accompanied by a change in Cu•••Cu separations of 2.6731(7) and 2.7114(7) Å (200 K) to a single distance of 2.7003(6) Å. This phase transition was also confirmed by differential scanning calorimetry, DSC, in which exothermic and endothermic processes were observed at -52 °C and -58 °C, upon cooling and heating, respectively.

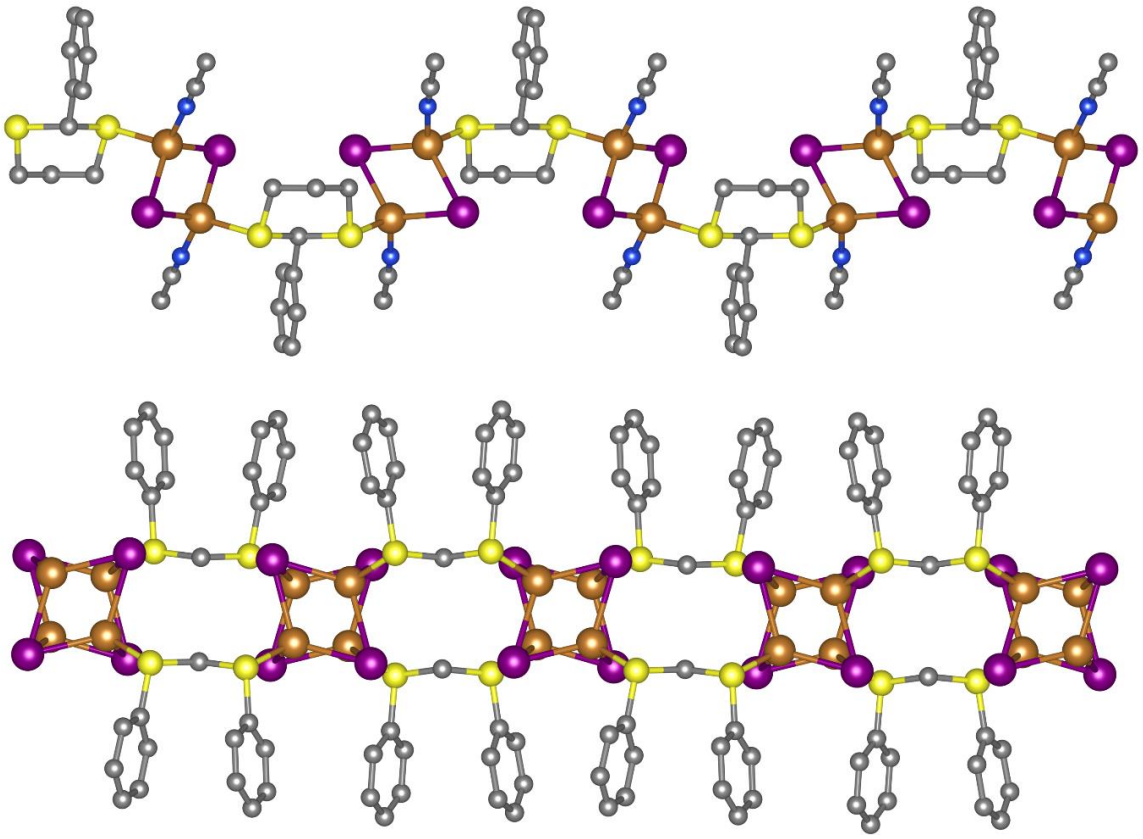

Figure 6. Top: X-ray structure of the 1D coordination polymer $[Cu_2I_2(CH_3CN)_2(\mathbf{L4})]_n$ at 250 K. Bottom: X-ray structure of the 1D coordination polymer $[Cu_4I_4(\mathbf{L5})_2]_n$ at 115 K. Cu, orange; N, blue; I, purple; S, yellow; C, grey. The images were reproduced using the cif files from the Cambridge Crystallographic Data Centre; CCDC numbers: 1886854 and 974324.

In a similar fashion going from 115 to 235 K, the X-ray structure of the cubane-containing 1D coordination polymer $[Cu_4I_4(L\mathbf{5})_2]_n$ (**L5** = $PhSCH_2SPh$; **Figure 6**) undergoes a phase change going from *C*2/c (115 K) to $P2_1/c$ (195 K).[18] The topology of the polymer does not change, except that the polymer becomes more zigzagging upon warming, but more strikingly, the process is accompanied by the loss of a 2-fold symmetry plane in the crystal (**Figure 7**). The mean Cu•••Cu separation, d(Cu•••Cu), and Cu_4 tetrahedron volume, V(Cu_4), increase monotonically with the temperature, as expected, but these increases are more rapid for the high temperature phase (note that there are breaks in the lines d(Cu•••Cu) and V(Cu_4) *vs* temperature whereas these breaks are not present in the graphs for other related polymers). Strikingly, there is no change in emission maxima (515 nm), and emission lifetime (τ_e = 1.0 and 1.2 μs) at 77 and 298 K, respectively, except for an impressive increase in bandwidth upon heating (75 *vs* 120 nm).

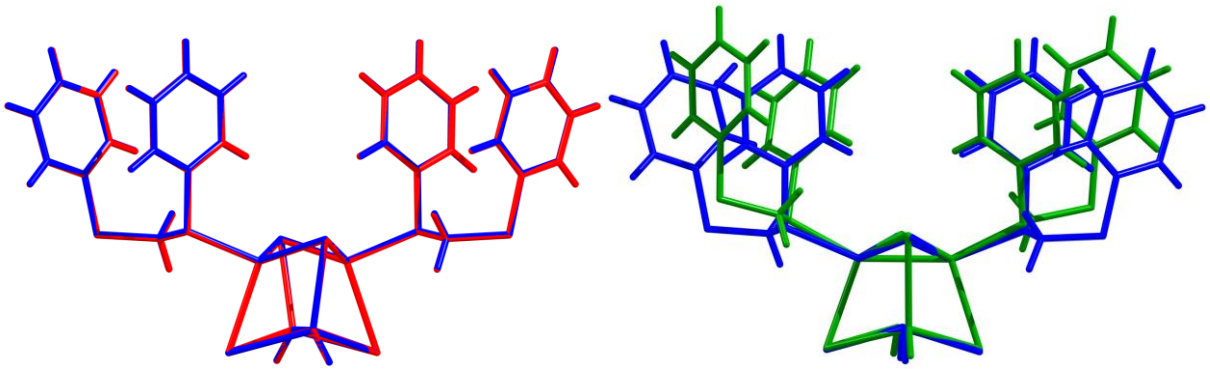

Figure 7. Comparison of a fragment of the $[Cu_4I_4(\mathbf{L5})_2]_n$ polymer (left: 115 and 195 K; right: 195 and 235 K). 115 K, blue, 195 K, red; 235 K, green. The images were reproduced using the cif files from the Cambridge Crystallographic Data Centre; CCDC numbers: 974324, 974326 and 974327.

The discrete and strongly luminescent cluster $Cu_4I_4(\mathbf{L3})_4$ (**L3** = THT = tetrahydrothiophene; **Figure 8**) exhibits a triclinic phase at 25 °C ($P\bar{1}$; thermodynamic product) and a yellow emission where the Cu•••Cu separations vary from 2.639(3) to 2.768(3) Å, which are considered normal distances.[19] This phase undergoes an endothermic transformation (based on DSC measurements) to monoclinic phase at 38°C ($P2_1/n$; kinetic product) where the Cu•••Cu separations vary from 2.673 to 2.837 Å. The latter exhibits an orange emission. This phase change is reversible and can be monitored by DSC (as mentioned) and emission spectroscopy, by which the thermochromism was pined down. At least two emission maxima (high and low energy bands) were depicted, as well as two τ_e values (about 15 and 9 μs, respectively) at 77 K. Upon grinding the monoclinic phase, part of the sample transforms into triclinic one, indicating that the latter one is the most stable phase.

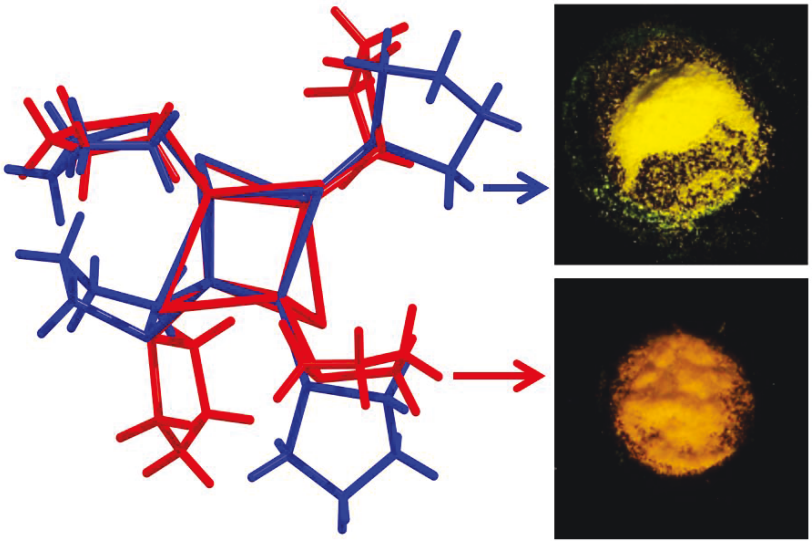

Figure 8. Left: Comparison of the Cu_4I_4(**L3**)$_4$ structure (red: 250 K; blue: 100 K). The image was reproduced using the cif files from the Cambridge Crystallographic Data Centre; CCDC numbers: 977483, 977482. Right: Photographs of the emissive phase samples of Cu_4I_4(**L3**)$_4$ under 365 nm excitation (up: low-temperature phase; bottom: high-temperature phase). Adapted from *Cryst. Growth Des.*, 2014, **14**, 1449–1458. Copyright (2014) American Chemical Society.

2.3. Luminescent Sensors

Earlier investigations reported by J. Kim and collaborators showed that the luminescence response was convenient tool to sensing a crystal change.[20] They prepared ligand **L6** and upon different synthesis conditions with CuI, they obtained 1D-[Cu_2I_2(**L6**)$_2$]$_n$, 2D-[Cu_4I_4(**L6**)$_2$]$_n$, and 1D-[Cu_4I_4(**L6**)$_2$]$_n$, identified by X-ray methods, and a material formulated as [Cu_4I_4(**L6**)$_2$(CH_3CN)(n-C_6H_{14})]$_n$. A crystal transformation was noticed between the non-luminescent 1D-[Cu_2I_2(**L6**)$_2$]$_n$ and emissive 2D-[Cu_4I_4(**L6**)$_2$]$_n$, where 1D-[Cu_2I_2(**L6**)$_2$]$_n$ became 2D-[Cu_4I_4(**L6**)$_2$]$_n$ upon heating the material (**Figure 11**). This transformation was accompanied by a conversion of the rhomboid Cu_2I_2 SBU, which is often weakly emissive, into the luminescent closed cubane Cu_4I_4 SBU. This reversed reaction can occur upon adding ligand in acetonitrile. In brief, these earlier studies showed that a drastic change in the SBU chromophore results in a sensitive change in emission properties.

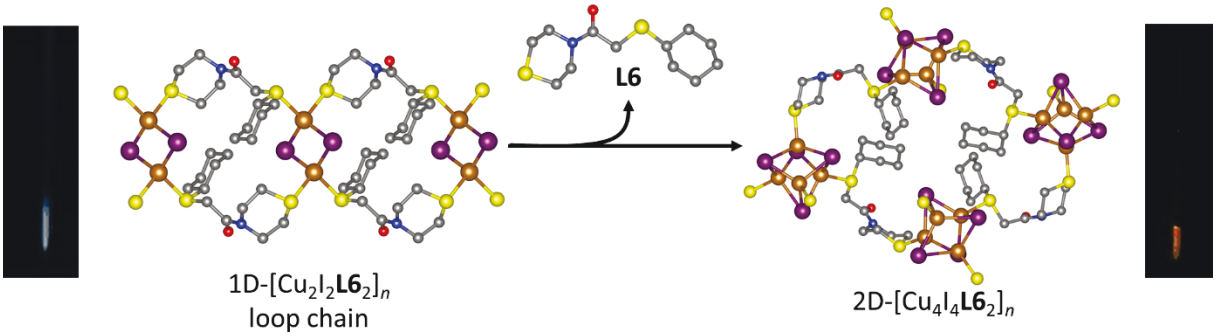

Figure 9. Solid state transformation of 1D-$[Cu_2I_2(\mathbf{L6})_2]_n$ (non-luminescent) into the emissive 2D-$[Cu_4I_4(\mathbf{L6})_2]_n$ upon heating (The inset are resulting luminescence). Cu, orange; N, blue; I, purple; S, yellow; O, red; C, grey. The images were reproduced using the cif files from the Cambridge Crystallographic Data Centre; CCDC numbers: 660768, 660759 and 660761. Adapted with permission from *Angew. Chem., Int. Ed*. 2008, **47**, 685-688. Copyright (2008) Wiley.

In parallel, this same group prepared the calix-[4]-arene ligand **L7** and upon different synthesis temperature, they obtained an emissive coordination polymer 1D-$[(Cu_2I_2)_2(\mathbf{L7})_2(Cu_4I_4)_2(\mathbf{L7})_2]_n$ at room temperature, and a non-emissive 1D-$[(Cu_3I_3)_2(\mathbf{L7})_2(CH_3CN)_2]_n$ at -10°C as revealed by X-ray crystallography (**Figure 10**).[21] Upon heating the latter coordination polymer at 175°C, a loss of CH_3CN takes place and this material becomes the luminescent 1D-$[(Cu_3I_3)_2(\mathbf{L7})_2]_n$ polymer. This rather subtle change in the SBU geometry also results in a drastic change in photophysical properties. The exposure of these last crystals to acetonitrile vapor, to verify reversibility was not attempted, but nonetheless this process could also serve as the basic concept of sensing solvent vapor.

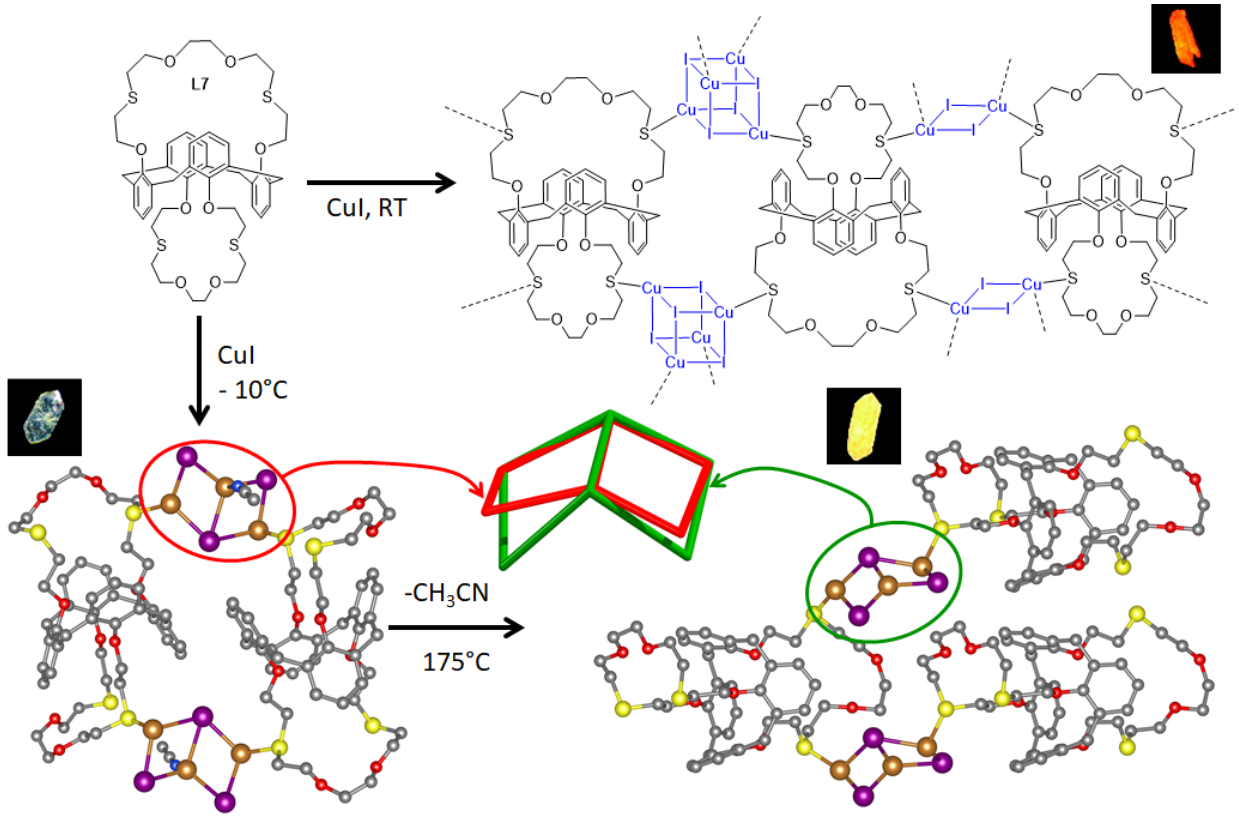

Figure 10. Obtention of emissive coordination polymer 1D-$[(Cu_2I_2)_2(\mathbf{L7})_2(Cu_4I_4)_2(\mathbf{L7})_2]_n$ and solid state transformation of non-emissive 1D-$[(Cu_3I_3)_2(\mathbf{L7})_2(CH_3CN)_2]_n$ into the emissive 1D-$[(Cu_3I_3)_2(\mathbf{L7})_2]_n$ polymer (The inset are resulting luminescence). Cu, orange; N, blue; I, purple; S, yellow; O, red; C, grey. The images were reproduced using the cif files from the Cambridge Crystallographic Data Centre; CCDC numbers: 695115 and 695116. Adapted with permission from *Angew. Chem., Int. Ed*. 2008, **47**, 685-688. Copyright (2008) Wiley.

Vaporchromism is the very basis for the sensing properties of these coordination polymers. Several examples of small molecule-responsive coordination polymers built upon copper halide-thioether and -thione networks have been reported during the past few years. For examples, Troyano *et al.* prepared a series of 1D coordination polymers from the direct reactions between **L8**, thiobenzamide (TBA) and CuX (X = Br, I) under room temperature conditions.[22] The resulting emissive polymers were characterized by X-ray crystallography as being [CuI(**L8**)•solvent]$_n$, $[Cu_3I_3(\mathbf{L8})_2]_n$ and [CuBr(**L8**)•solvent]$_n$ (**Figure 11** and **Figure 13**). The former (λ_{emi} = ~630 and ~635 nm; 100 K) and latter (λ_{emi} = 610-685 nm; 100 K) coordination polymers exhibit a vapour-responsive behaviour based on their luminescence responses to vapor. At 100 K, the luminescence

readily appears of various tints of red, pink and purple depending on the solvent. This solvent-responsive trait observable with naked eyes spectroscopically translates into a difference in emission band shape for [CuI(**L8**)•solvent]$_n$ (solvent = nothing, featureless; THF (tetrahydrofuran), presence of a shoulder). For [CuBr(**L8**)•solvent]$_n$ (at 100 K), the λ_{emi} values vary from 610 (no solvent) to 630 (THF) to 685 nm (Me_2CO) (**Figure 12**). These materials are also found semiconducting also making them multifunctional (**Table 2**).

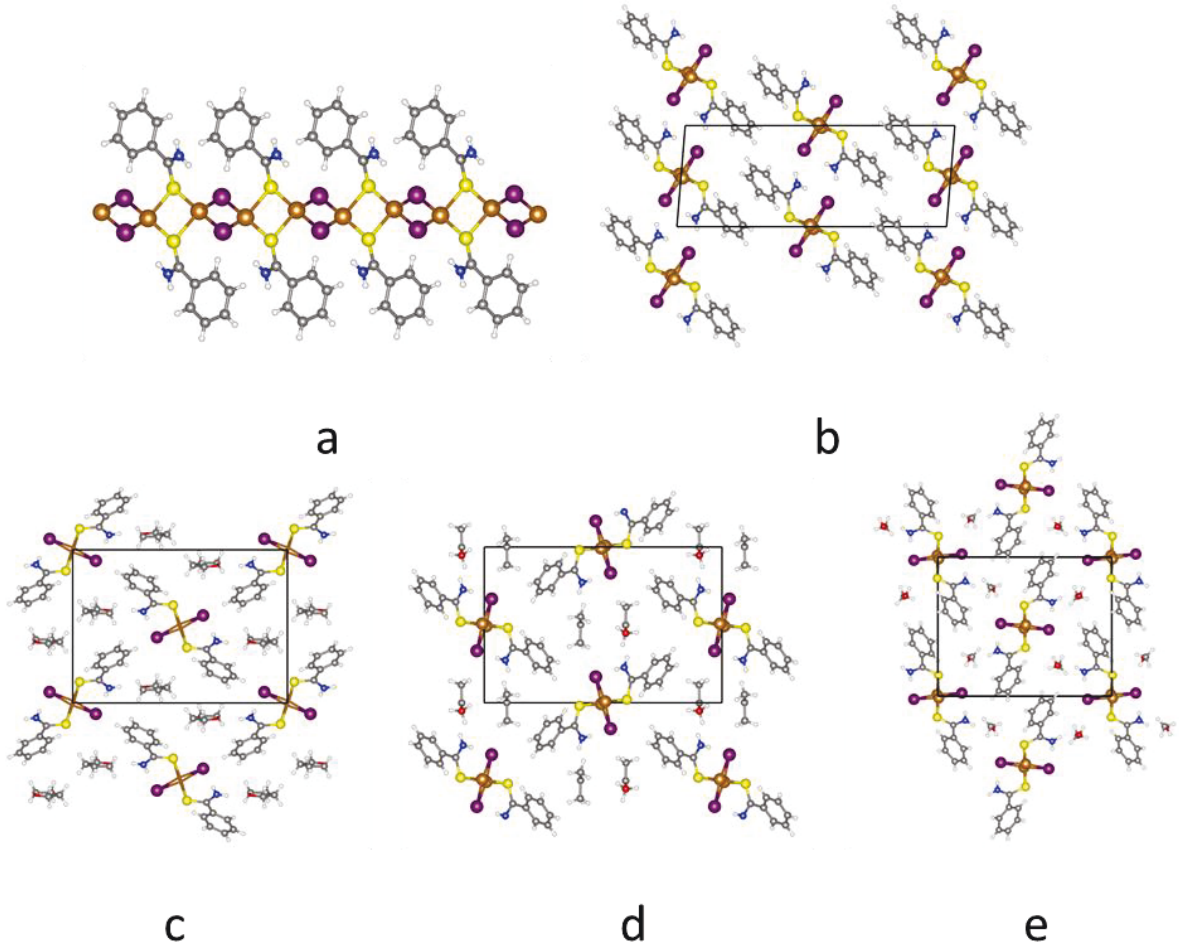

Figure 11. (a) Side view of [CuI(**L8**)•solvent]$_n$. Chain packing where solvent = nothing (b), THF (c; note: not emissive at 298 K), Me_2CO (d), MeOH (e). Cu, orange; I, purple; S, yellow; N, blue; O, red; C, grey; H, white. The images were reproduced using the cif files from the Cambridge Crystallographic Data Centre; CCDC numbers: 1835539 (a, b), 1835543 (c), 835541 (d), 1835545 (e).

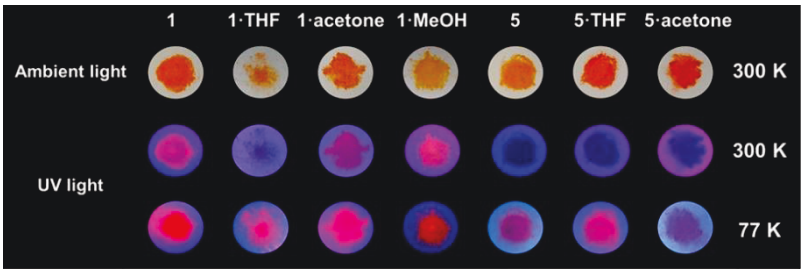

Figure 12. Photographs of solid samples of 1D-[CuI(**L8**)•solvent]$_n$, **1**·S (S = nothing; THF, acetone, MeOH), and [CuBr(**L8**)•solvent]$_n$, **5**·S (S = THF, acetone) under ambient light and UV-lamp irradiation at 356 nm at RT (300 K) and in liquid nitrogen (77 K). Reproduced with the permission of *Inorg. Chem.*, 2019, 58, 3290–3301. Copyright (2019) American Chemical Society.

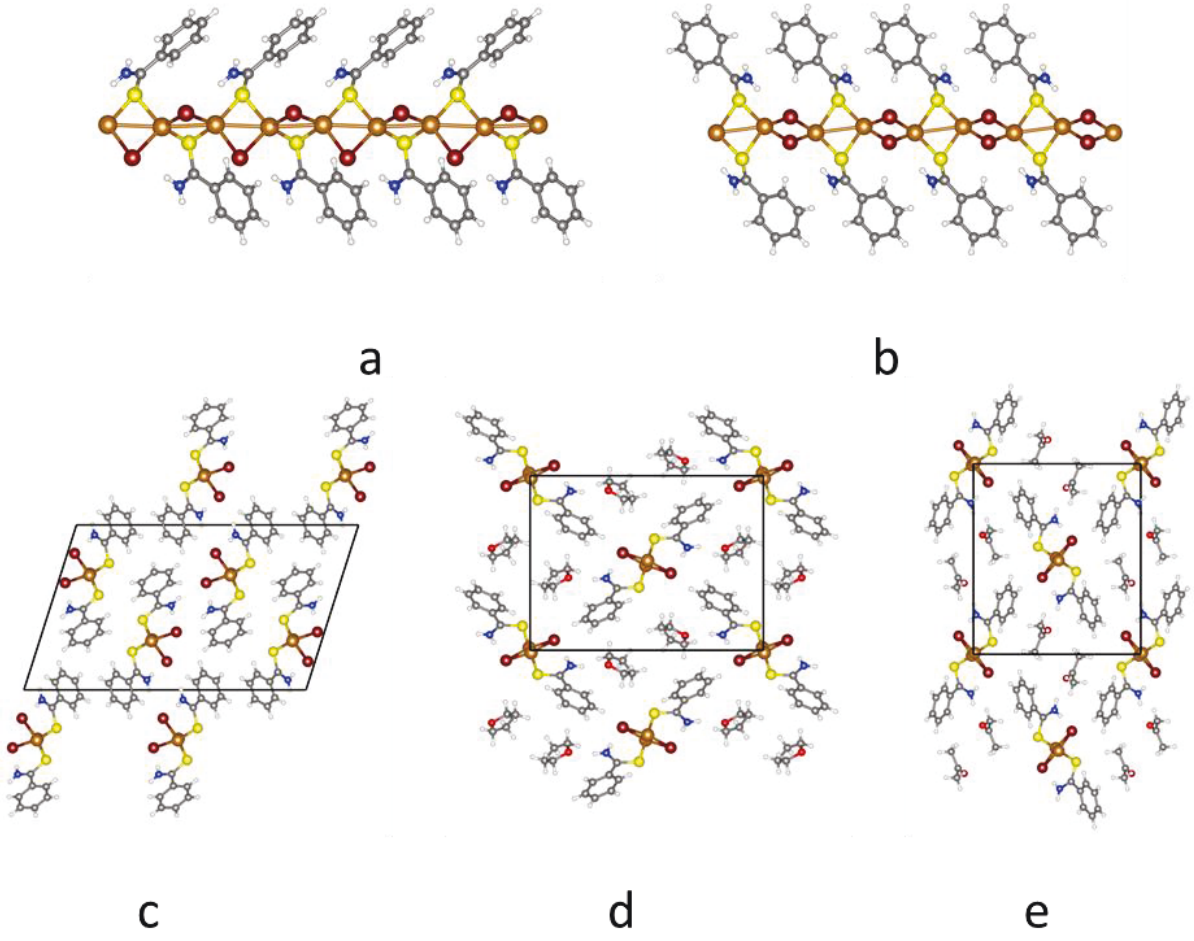

Figure 13. Side view of [CuBr(**L8**)]$_n$ (a) and [CuBr(**L8**)•solvent]$_n$ (b). Chain packing where solvent = nothing (c), THF (d), Me_2CO (e). Cu, orange; Br, brown; S, yellow; N, blue; O, red; C, grey; H, white. The images were reproduced using the cif files from the Cambridge

Crystallographic Data Centre; CCDC numbers: 1835552 (a, c), 1835555 (b), 1835555 (d), 1835554 (e).

Table 2. Electrical conductivity data for [CuI(**L8**)•solvent]$_n$ and [CuBr(**L8**)•solvent]$_n$ (using the two contact method).

298 K	[CuI(**L8**)•solvent]$_n$			[CuBr(**L8**)•solvent]$_n$		
solvent	none	Me_2CO	MeOH	none	THF	Me_2CO
form	pellet	crystal	crystal	pellet	crystal	crystal
conductivity, S.cm^{-1}	3.3×10^{-11}	1.3×10^{-8}	1.15×10^{-9}	3.6×10^{-8}	1.9×10^{-7}	1.5×10^{-9}
bandgap, eV	1.38	1.22	1.36	1.23	1.21	1.27

Other examples include the work reported by Kim *et al.* in which four solvent responsive dithioether-containing 1D-coordination polymers were synthesized ({[Cu_4I_4**L9**$(MeCN)_2$]•solvent}$_n$; solvent = CH_2Cl_2 (1), $CHCl_3$ (2), xylene (3), nothing (4); **L9** = *N*,*N*'-bis[2-(cyclohexylthio)ethyl]pyromellitic diimide) when exposed to various solvent vapours.[23] In these cases, the somewhat porous luminescent 1-D coordination networks are secured by bidentate ligands **L** (**L9**), which adopt either the *syn*- (**1**, **2**, **3**) or *anti*-conformation (**4**). The SBUs are the emissive Cu_4I_4 cubanes and are bonded to bidentate **L9** *via* two Cu-S bonds and two monodentate MeCN ligands. Solvent exchange is easily performed upon exposure to solvents (**1** ↔ **2** ↔ **3**). This process is accompanied by modest shifts of the emission band (vaporchromism between ~585 and ~610 nm) and small structural changes. Upon heating **1**-**3** and in the presence of MeCN vapour, the solvent molecules leak out and **L9** undergoes a *syn* → *anti*-transformation thus forming **4**, which exhibits an emission maximum at ~580 nm. Compound **4** reversibly returns to **1**-**3** in the *syn*-conformation of upon exposing to their initial solvent vapours (**Figure 14**).

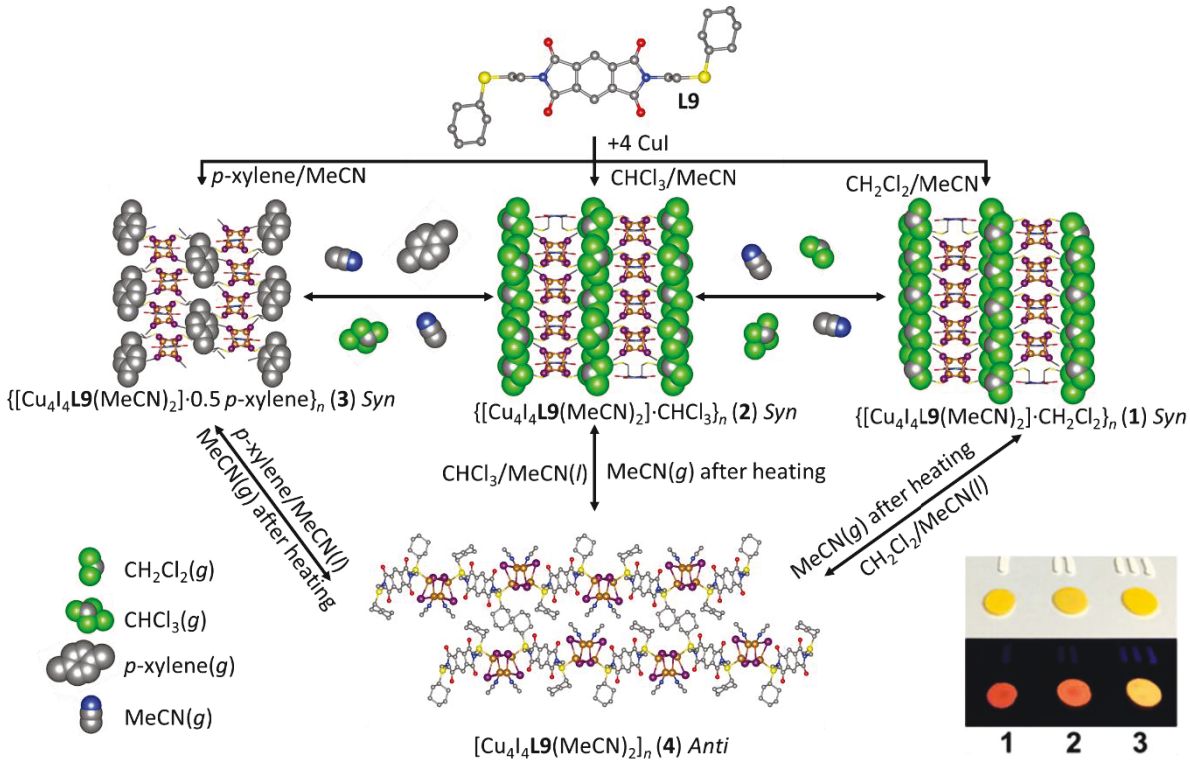

Figure 14. Structures of the {[Cu_4I_4**L9**$(MeCN)_2$]•solvent}$_n$ **1**, **2**, **3** and **4**. Cu, orange; I, purple; S, yellow; N, blue; O, red; Cl, green; C, grey. The images were reproduced using the cif files from the Cambridge Crystallographic Data Centre ; CCDC numbers: 1417587-1417591. Inset: Photoluminescence of the coordination polymers **1-3**. Top, ambient light, bottom, λ_{exc} = 365 nm. Adapted with permission from *Cryst. Growth Des.*, 2015, **15**, 5183–5187. Copyright (2015) American Chemical Society.

A modern application to sensors was recently put forwards by Liu *et al.* for the detection of antibiotics in the environment.[24] The reaction of CuI with 3-ethyl-1,3-benzothiazole-2-thione (EBT (**L10**)) under solvothermal conditions generates light green single crystals, which turned out to be a 3D coordination polymer of formula [Cu_4I_4(**L10**)$_5$]$_n$ as identified by X-ray diffraction methods (**Figure 15**a,b). [Cu_4I_4(**L10**)$_5$] in the solid state exhibits an absorption maximum in the vicinity of 400 nm and a photoluminescence in the yellow-green region (λ_{emi} = ~550 nm) exhibiting an emission lifetime of 9.13 μs. The presence of an ethyl group suggests enhancement of its hydrophobicity, making it insoluble and consequently promoting its stability in water. Indeed, this material exhibits an excellent stability when soaked in water and a good emission intensity appearing as suitable material for outdoor applications. The preparation of pellets proved

easy and the cycling tests, by soaking in water then drying in air, demonstrated its stability upon monitoring the PXRD patterns. Eight common antibiotics were examined in aqueous solutions, which included tetracycline hydrochloride (TCH), tetracycline (TC), chloramphenicol (CMP), amoxicillin (AMX), ampicillin (AMP), ciprofloxacin (CIP), ronidazole (RDZ), and sulfamethazine (SMA), and some common organics. In all cases, emission quenching occurred in mM concentrations of antibiotics, even observable with naked eyes. Upon monitoring the emission intensity *vs.* the concentration of the antibiotics, Stern-Volmer analyses permitted to compare their quenching efficiencies. For the antibiotics, the trend is TCH > TC > CMP > AMX > AMP > CIP > RDZ > SMA. TCH turned out to exhibit the highest quenching efficiency, which is about 6 times larger than the efficiencies of other antibiotics. The detection limit was evaluated to be ~ 4.8 ppm (10 mM). The mechanism was addressed (*i.e.* static quenching *vs* dynamic quenching) and the perfect match between the emission decays of solutions containing $[Cu_4I_4(\mathbf{L10})_5]_n$ alone and $[Cu_4I_4(\mathbf{L10})_5]_n$ with THC provided evidence for a static quenching. The presence of the unsaturated site for anchoring antibiotic molecules, most presumably at the surface of the particles, must play a key role prior to quenching. The nature of the emission quenching is still yet to be formally elucidated (*i.e.* electron transfer *vs.* energy transfer), but the authors favored the former.

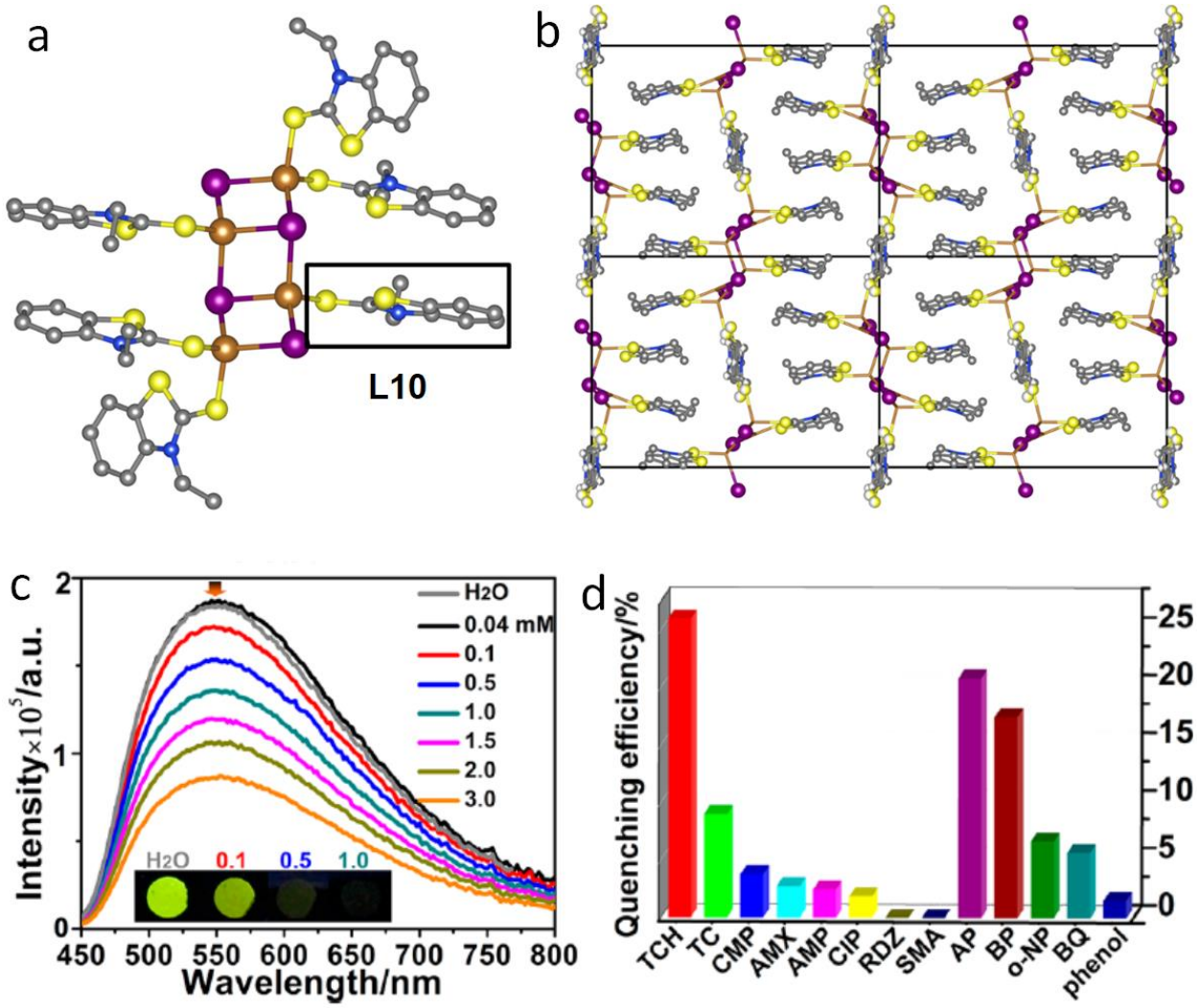

Figure 15. (a) Structure of the $[Cu_4I_4(\mathbf{L10})_5]_n$ motif. (b) 3D structure of the $[Cu_4I_4(\mathbf{L10})_5]_n$ coordination polymer. Cu, orange; I, purple; S, yellow; N, blue; C, grey. The images were reproduced using the cif files from the Cambridge Crystallographic Data Centre; CCDC number: 1827572. (c) Emission spectra of $[Cu_4I_4(\mathbf{L10})_5]_n$ dispersed in aqueous solution of TCH with various concentration. Inset: photographs of pellets in water, 0.1, 0.5, and 1.0 mM of TCH aqueous solutions, under to UV-light. (d) Luminescence quenching of $[Cu_4I_4(\mathbf{L10})_5]_n$ by different analytes. Adapted with permission from *Cryst. Growth Des.*, 2018, **18**, 5441–5448. Copyright (2018) American Chemical Society.

2.4. Metal-Organic Frameworks (MOFs)

One of the key strategies in designing MOFs is the use rigid of organic ligands. Indeed, 2,11-dithia[3.3]paracyclophane (dtpcp (**L11**)) falls into this category. Munakata *et al.* prepared two isostructural porous 3D frameworks of general formula $\{[CuX(\mathbf{L11})]\cdot MeCN\}_n$ (X = Br, I) identified by X-ray crystallography (**Figure 16**).[25] The SBU motif consists of a zigzag $(Cu\text{-}X\text{-}Cu\text{-}X)_n$ chains (X = Br, I). The frameworks exhibit elliptical channels along the a-axis, in which MeCN guest molecules are found. Although these materials clearly fall into the category of MOFs, no BET (Brunauer–Emmett–Teller) analysis measurement was performed. However, adsorption and desorption experiments monitoring the reversible incorporation of guest MeCN occurred without the collapse of the 3D framework as confirmed by PXRD and ^{1}H NMR (Nuclear magnetic resonance) spectroscopy. Moreover, the porous $\{[CuI(\mathbf{L11})]\cdot guest\}_n$ coordination polymer exhibits selectivity in polarity and size for small molecule inclusions. The favorable guests for inclusions are methanol, dichloromethane, acetone, dimethylether, trichloromethane, ethanol and 1-propanol. The absence of an analytical signal such as luminescence (which is common for SBU motifs of the type $(Cu\text{-}X\text{-}Cu\text{-}X)_n$) or conductivity, predictably precluded the design of small molecule sensors in this case.

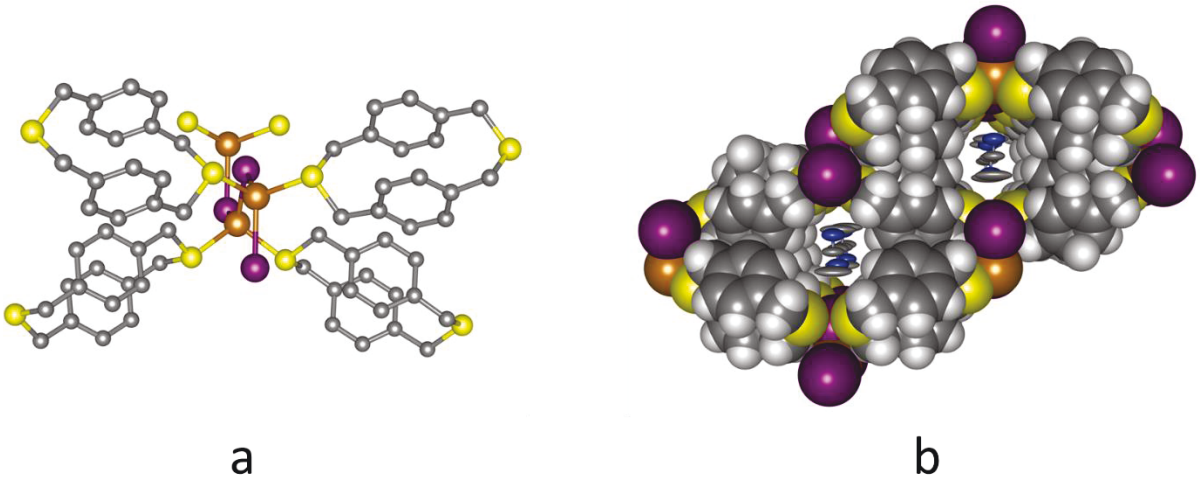

Figure 16. Structure of the isostructural 3D frameworks $\{[CuX(\mathbf{L11})]\cdot MeCN\}_n$ (X = Br, I). (a) Fragment of the 3D coordination polymer stressing on the $(Cu\text{-}X)_n$ chain motif. (b) 3D structure of the $\{[CuX(\mathbf{L11})]\cdot MeCN\}_n$ frameworks stressing on the presence of long channels and MeCN guest molecules. Cu, orange; I, purple; S, yellow; N, blue; C, grey; H, white. The images were

reproduced using the cif files from the Cambridge Crystallographic Data Centre; CCDC number: 232772.

Concurrently Xu *et al.* used a clever approach to construct porous and yet robust frameworks in which a common linear tribenzene dicarboxylate organic ligand (**L12** = $^{-}O_2C$-C_6H_4-$C_6H_2R_2$-C_6H_4-CO_2^{-}) containing side thioether scaffolding functions (R = SMe) as pre-programmable anchors to attach metallic centers (*i.e*. template).[26] In this case, a soft metal component (here CuI), that they call soft imprinting, was incorporated. Indeed, the synthesis involves reacting HO_2C-C_6H_4-$C_6H_2(SMe)_2$-C_6H_4-CO_2H (H_2**L12**) with $EuCl_3$ and CuI in a 1:1 water/MeCN mixture at 140°C (*i.e*. solvothermal conditions) to produce a colorless MOF of formula $\{[Eu(\mathbf{L12})_{1.5}(CuI)]\cdot H_2O\}_n$ (elucidated by X-ray crystallography, **Figure 17**a,b,c). Predictably, this MOF exhibits the distinct luminescence associated with the Eu^{3+} center. The structure consists in Eu^{3+}-carboxylate columns interlinked by the ligand. Running parallel to these inorganic rods, 1D-zigzag chains of $[(SMe)C_6H_2(SMe)_2$-Cu_2I_2-$(SMe)C_6H_2(SMe)]_n$ are formed bearing important consequences. First, this MOF can impressively sustain boiling water for 24 h. Moreover, upon heating the solid to 200°C for 4 h under vacuum, the structure remained intact based on the PXRD patterns. In addition, the TGA (thermogravimetric analysis) measurements indicated minimal weight loss from the host structure up to 240°C. This double structural solidification from the Eu^{3+}-carboxylate rods and the 1D coordination Cu_2I_2-containing chain contributes to this MOF strengthening. The hydrophobicity of the long organic ligand may help repelling water molecules. BET analysis indicates that the surface area is 560 m^2g^{-1}, with a pore volume 0.034 cm^3g^{-1}, corresponding to a pore diameter of 7.5 Å, which is fully consistent with the single crystal structure. The sensing properties were demonstrated upon exposing the MOF suspended in water to dissolve H_2S. For example, exposing the MOF to 20 ppm (parts per million) of H_2S for 30 min leads to the quenching of the red emission associated with the presence of Eu^{3+} ions. At 80°C, even 1 ppm of H_2S could quench the luminescence within 2 h. Although this was not formally demonstrated using, for instance the comparison of the PXRD patterns, H_2S could be suspected to dislodge Cu(I) ions to form Cu_2S nanoparticles (and HI), leaving behind another MOF $\{[Eu(\mathbf{L12})_{1.5}]\}_n$, which was also synthesized in parallel in this investigation. The latter MOF was found to be non-luminescent. No reversibility testing was either performed or mentioned, likely diminishing the possibility to use this material for sensing H_2S and small thiols and thioether molecules. Conversely, the

{[Eu(**L12**)$_{1.5}$(CuI)]·H_2O}$_n$ MOF can be used to design white light LED (light emitting diode) using other concomitant lanthanide ions.

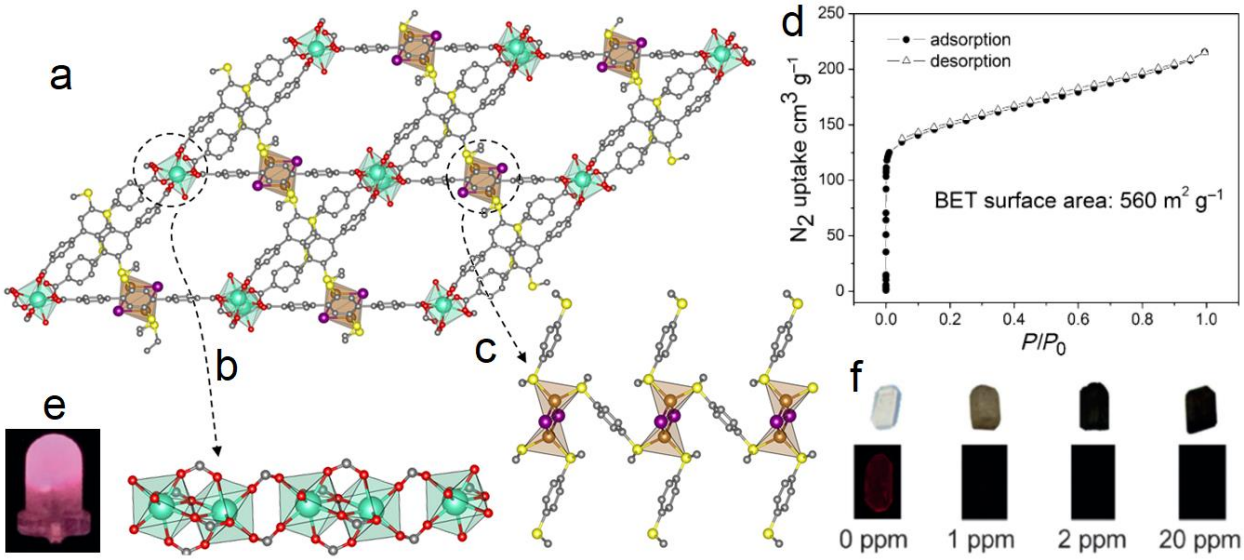

Figure 17. (a) Structure of the {[Eu(**L12**)$_{1.5}$(CuI)]·H_2O}$_n$ MOF (the water molecules are not shown for clarity). (b) View of the Eu-containing coordination chain. (c) View of the secondary 1D zigzag coordination chain involving the centrosymmetric rhomboid $Cu_2I_2S_4$ SBU (note that **L12** is not drawn completely for clarity (the Cu•••Cu separation is 2.807Å). Cu, orange; I, purple; S, yellow; O, red; C, grey; Eu, light green. The images were reproduced using the cif files from the Cambridge Crystallographic Data Centre; CCDC number: 1422000. (d) The N_2 sorption isotherm of {[Eu(**L12**)$_{1.5}$(CuI)]·H_2O}$_n$ MOF. (e) Photograph of a LED coted with the {[Eu(**L12**)$_{1.5}$(CuI)] ·H_2O}$_n$ MOF. (f) Photographs of a single crystal of the {[Eu(**L12**)$_{1.5}$(CuI)]·H_2O}$_n$ MOF soaked in solutions containing H_2S at various concentrations (in ppm) under natural light (bottom) and exciting at 365 nm (top). Adapted with permission from *Chem. - A Eur. J.*, 2016, **22**, 1597–1601. Copyright (2016) Wiley-VCH.

Concurrently, the ditopic ligand 5-(pyridin-3-yl)-1H-1,2,4-triazole-3-thiol **(3-Hptt** (**L13**)) reacts with CuI in diethylformamide to form the luminescent {[$(Cu_4I_4)_3(Cu_6)_2$(**L13**)$_{12}$]•24DEF•12H_2O}$_n$ MOF (DEF = *N*,*N*-diethylformamide), which was identified by single crystal X-ray diffraction.[25] The X-ray data reveal a 3D network in which two different SBUs are depicted: the common cubane $Cu_4I_4N_4$ and a hexagonal Cu_6S_6 cluster placed in an alternate arrangement (**Figure 18**). In the hexagonal Cu_6S_6 cluster, the ligand is under the form of thiolate, which is quite common with thiol

derivatives places under solvothermal conditions. The difference in coordination environments between the clusters create helical arrays, each alternating right-handed and left-handed. Between these arrays are helical channels in which solvent molecules can penetrate. The total volume rendered accessible to solvent molecules calculated using PLATON[27] is around 71.9 % of the total volume and the solvent accessible surface area was determined to be about 2255 m^2g^{-1} based on Poreblazer software.[28] Unfortunately, these cavities could not be activated upon heating under vacuum or through solvent exchange. Upon excessive heating, the structure collapses as soon as the solvent molecules are removed. Clearly, despite this interesting structure, this MOF seems not to be suited for sensing applications at this time. Conversely, this MOF exhibits a double emission; one expectedly associated with the $Cu_4I_4N_4$ cubane (λ_{emi} = ~595 nm; triplet cluster-centered, ^{3}CC*, only visible at low temperature) and one due to the hexagonal Cu_6S_6 cluster (λ_{emi} = ~845 ± 10 nm; *i.e.* in the near-IR (Near-infrared) ; τ_e = 1.72 μs at 298 K). The latter emission was also assigned to a triplet CC* excited state despite the rather long Cu•••Cu separation (3.21 Å). The excitation spectra indicate that these two cluster chromophores behave independently, most likely due to the long distance between the two. At 77 K, the $Cu_4I_4N_4$ cubane emission exhibits a biphasic decay 15.0 and 46.2 μs, whereas the luminescence decay of the hexagonal Cu_6S_6 cluster is monoexponential (τ_e = 21.3 μs). The bi-exponential decay behaviour is not uncommon as mentioned in the previous section, and the time scale for these excited state lifetimes are typical for such type of Cu-containing clusters.

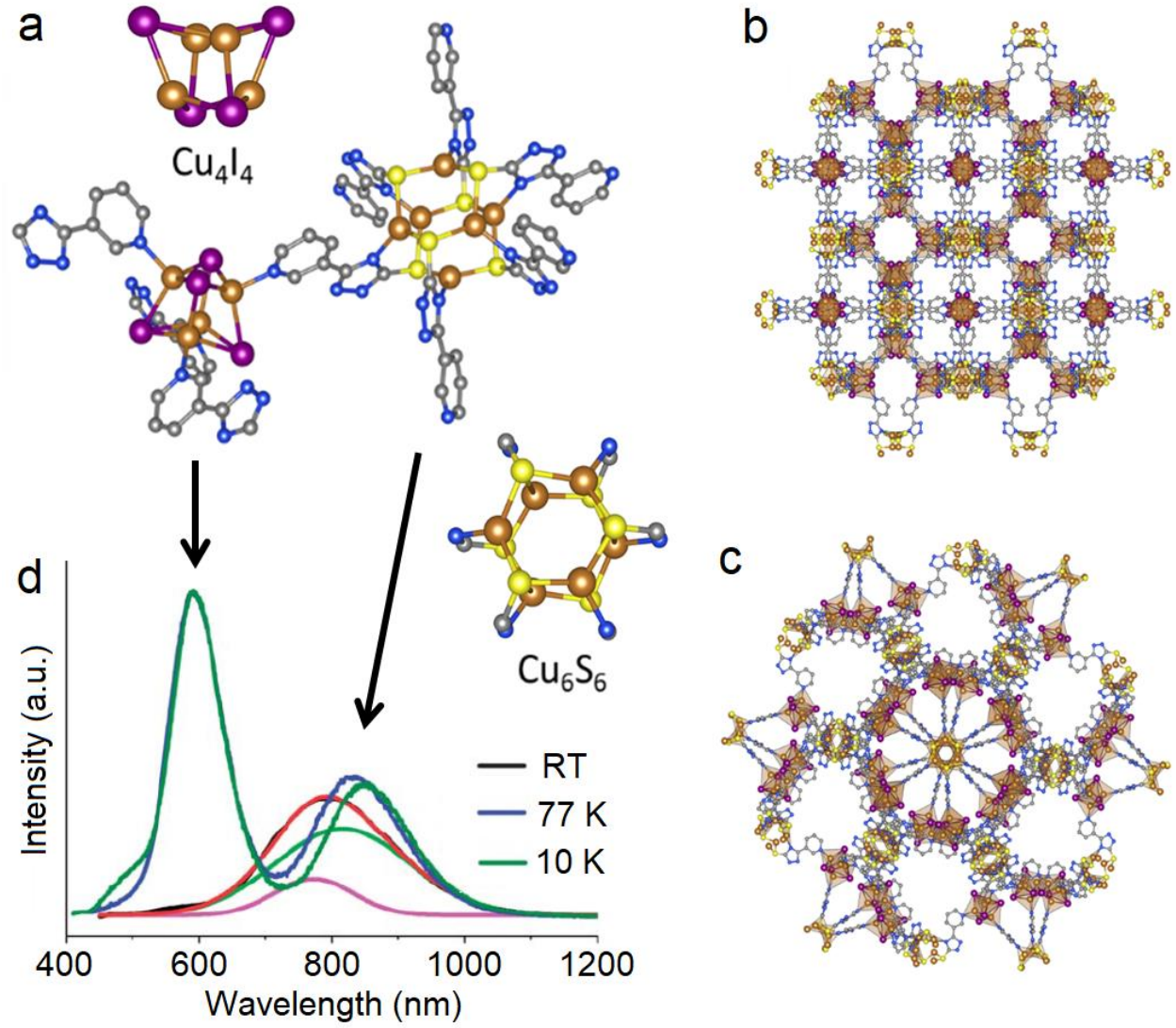

Figure 18. (a) Structures of the two clusters and their ligand environments. (b, c) Structure of the $\{[(Cu_4I_4)_3(Cu_6)_2(\mathbf{L13})_{12}]\bullet 24DEF\bullet 12H_2O\}_n$ MOF (the water and DEF molecules are not shown).The center-to-center distance between the $Cu_4I_4N_4$ cubane and hexagonal Cu_6S_6 cluster is ~50 nm. Cu, orange; I, purple; S, yellow; N, blue; C, grey; H, white. The images were reproduced using the cif files from the Cambridge Crystallographic Data Centre; CCDC number: 867097. (d) Emission spectra of this MOF at different temperatures (λ_{exc} = 365 or 370 nm). The green, pink and red lines are gaussian fitted curves with a coefficient of determination (COD) > 0.994). Adapted with permission from *Chem. Sci.*, 2013, **4**, 1484–1489. Copyright (2013) Royal Chemical Society.

2.5. Homogeneous and heterogeneous catalysis

The use of neutral copper halide-chalcogenoether and -chalcogenone-based materials is not new for catalysis, and many examples of applications have been reported. Indeed, an earlier investigation dealt with the use of CuCl and Me_2S, which together seemingly form a the tetrameric $[CuCl(\mathbf{L1})]_4$ cluster, a formulation based on chemical analysis, and catalyzes the isomerisation of 3,4-dichloro-1-butene to 1,4-dichloro-2-butene in solution, as monitored by UV-vis and electronic paramagnetic resonance (EPR) spectroscopy.[29] Note that the structure of this species has not been demonstrated by X-ray diffraction or any other physical techniques. Evidence for copper(II) species was made, despite that $CuCl_2$-analogue was found to be much poorer as a catalyst. Interestingly, one of the main conclusions was that this species containing **L1** exhibits higher catalytic activity than the $(n\text{-heptyl})_2S$ thioether analogue. Subsequently, a cubane $[CuCl(\mathbf{L2})]_4$ cluster, a structure based on chemical analysis and spectroscopy, was also studied by this same group and showed similar catalytic activities towards this isomerisation and exhibited similar catalytical activity as the Me_2S analogue.[30] Mixed valence species were again suspected to be the active catalyst, making the tetranuclear clusters act as pre-catalysts. Subsequently, further kinetic and spectroscopic studies, notably UV-Vis (ultraviolet-visible), IR (infrared), EPR, and ^1H NMR, suggested the formation of a polynuclear intermediate containing both Cu(I) and Cu(II) ions prior to the electron transfer step in the reaction mechanism.[31] Moreover, the EPR spectra of these mixed-valent pre-catalysts indicated the presence of five-coordinated Cu(II) metals with a trigonal-bipyramidal coordination sphere.

Recently, CuX-based catalysts (X = I, Br, Cl) were investigated.[32] This investigation focussed on the use of a polydentate ligand 1,2-bis(3,5-dimethyloxazol-4-ylmethylthio)ethane (**L14**), which upon complexation with CuX forms a series dinuclear complexes formulated as $Cu_2X_2(\mathbf{L14})$. As all attempts to obtain crystals for X-ray studies stubbornly failed, the structure was proposed on the basis of elemental analysis, IR spectra, and optimized geometry calculations, in which the ligand is bonded through the sulfur atoms (**Figure 19**). However, this does not preclude the possibility of the formation of a coordination polymer in the solid state as the ligand exhibit two free imine sites and a Cu(I) somewhat distorted from the ideal triangular planar geometry in the optimized geometry. Nevertheless, these complexes or coordination polymers ([Cu]) exhibited high catalytic activity in the aminomethylation of phenylacetylene (**Figure 19**), notably with

N,*N*,*N*',*N*'-tetramethylmethane-diamine, bis(oxazolidin-3-yl)methane, and benzaldehyde-piperidine systems (T = 60 °C). These catalysts exhibited similar catalytic activity as the CuCl alone towards *N*,*N*,*N*',*N*'-tetramethylmethanediamine but the Cu_2I_2(**L14**) catalyst turned out sensibly superior in selectivity with a 99.8% composition at the end of the reaction (99% conversion). Conversely, Cu_2Cl_2(**L14**) catalyst was the best for the conversion of bis(oxazolidin-3-yl)methane (100% composition). The proposed mechanism included the coordination of the acetenyl function onto the tricoordinated Cu(I) centers, which activate the C-H bond. This step is followed by a nucleophilic attack onto the α-carbon of the amine, which contains a labile proton.

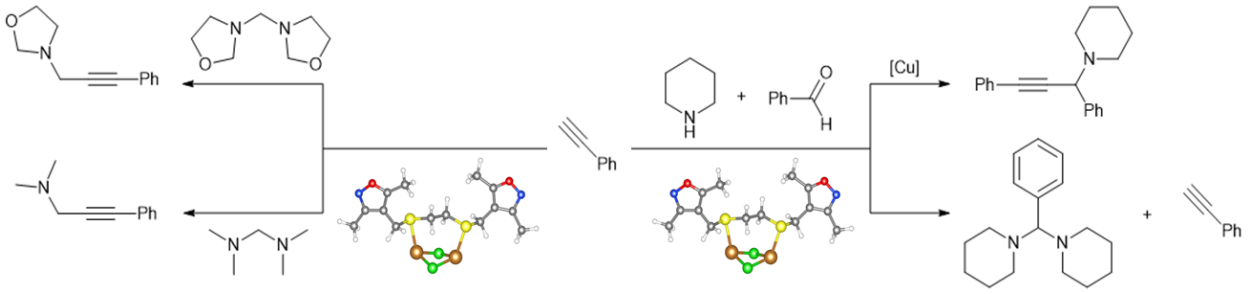

Figure 19. Scheme showing the various catalyzed reactions and the proposed structure of the optimized geometry of the Cu_2Cl_2(**L14**) catalyst. Cu, orange; Cl, green; S, yellow; N, blue; O, red; C, grey; H, white.

Another ditopic ligand, bis(2-(benzylthio)ethyl)amine ((benzyl-S-$CH_2CH_2)_2NH$), was reacted with $Cu(ClO_4)_2$ in the presence of KI resulting in the formation of a Cu(I)-containing coordination polymer formulated as $[Cu_2I_2$(**L15**)$]_n$ and revealed by X-ray crystallography (**Figure 20**).[33] This 1D polymeric species includes a 1D-$(Cu_2I_2$-$Cu_2I_2)_n$ central motif supported by the tridentate ligand through both Cu-S and Cu-N bonds, in which one S- and the N-atoms chelate one Cu(I) metal, whereas the other S-donor bridges the next unit. All Cu(I) metals are tetracoordinated. This $[Cu_2I_2$(**L15**)$]_n$ coordination polymer catalytically actives a copper-catalyzed azide-alkyne cycloaddition in a three-component click reaction (also known as atom-efficient 1,3-dipolar Huisgen cycloaddition reaction) of benzyl chloride, sodium azide, and phenylacetylene in a H_2O/MeCN mixture yielding to 1-benzyl-4-phenyl-1H-1,2,3-triazole. The resulting yields were good (72-87%, isolated) at 298 K, for periods varying from 1 to 24 h and using 0.5 to 5 mol % loading, even in the absence of a base or a reducing agent.

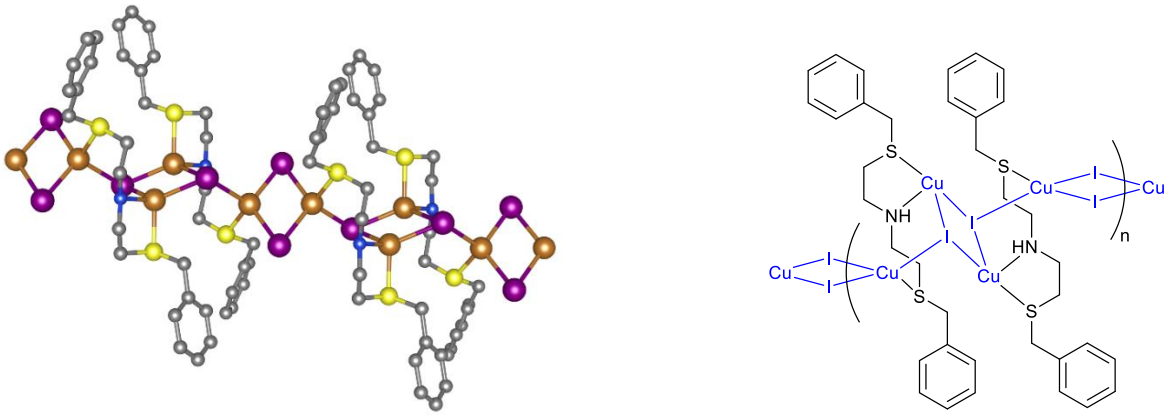

Figure 20. Right, X-ray structure of the coordination polymer $[Cu_2I_2(\mathbf{L15})]_n$. Left, chemdraw representation of the CuI chain link. Cu, orange; I, purple; S, yellow; N, blue; C, grey. The image was reproduced using the cif files from the Cambridge Crystallographic Data Centre; CCDC number: 692263.

Another investigation focussing on one pot three-component click reactions was reported about the same time and involved the use of the 1D coordination polymer $[Cu_2I_2(\mathbf{L16})_2]_n$.[34] This coordination polymer is obtained from the direct reaction of CuI with the ligand in a 1:2 metal to ligand ratio and was characterized by ^1H and ^{13}C NMR and X-ray methods (**Figure 21**). The structure consists of a wide ladder-shaped coordination polymer where the bridging ligands coordinate Cu_2I_2 rhomboids as the steps. The 1,3-dipolar Huisgen cycloaddition reactions involved benzyl bromide, sodium azide, and phenylacetylene, and proceeded in various solvents (neat, MeOH, MeCN, H_2O, H_2O/MeCN (1:1 mixture)) in the presence of 0.1 to 5.0 mol % of catalyst at 50 or 60°C for periods ranging from 0.5 to 8 h. The yield varied from 65 to 97 %, but half of the entries reached more than 90 %. The extension of this procedure with other acetynyl derivatives and organohalides in H_2O/MeCN (1:1 mixture) at 50°C mostly for 3 to 4 h, and 0.1 mol % of catalyst provided similar performances. A mechanism was proposed involving the formation of an anionic 5-coordinate Cu(I) intermediate (*i.e.* a 20-electron complex).

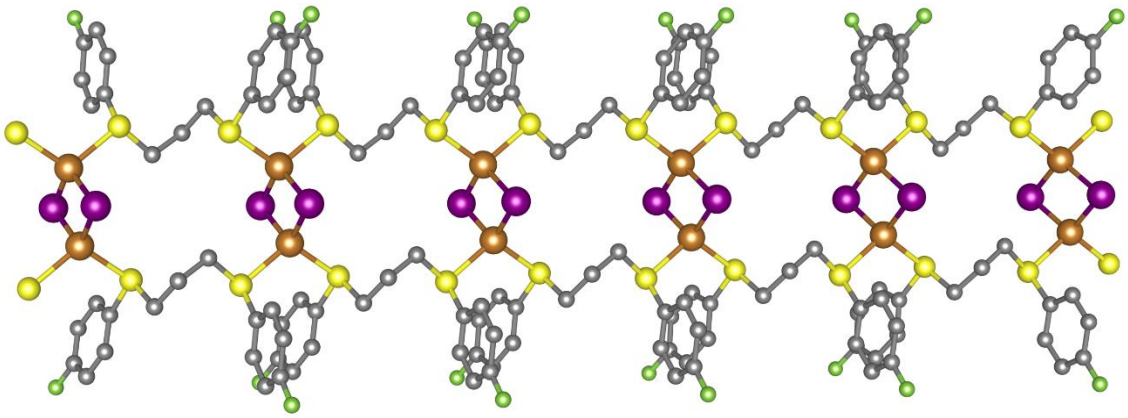

Figure 21. X-ray structure of the 1D arrangement of the $[Cu_2I_2(\mathbf{L16})_2]_n$ coordination polymer. Cu, orange; I, purple; S, yellow; F, green; C, grey. The image was reproduced using the cif files from the Cambridge Crystallographic Data Centre; CCDC number: 1835102.

This same group extended afterward this chemistry to the 1-(1-{4-chlorophenylthio}propan-2-ylthio)-4-chlorobenzene ligand (**L17**).[35] Indeed, after preparing the 2D layered $[Cu_2I_2(\mathbf{L17})_2]_n$ polymer from the direct reaction of CuI with the ligand, the resulting material was identified by X-ray techniques (**Figure 22**). The new material consists in a 2D network polymer somewhat reminiscent of the 1D coordination polymer described above. The difference is that the 2D sheets are likely formed because the C_2-chain may favor the *anti*-conformation, whereas the C_3-chain is likely prone to favor the *syn*-one, thus placing the S-atom in positions for the fabrication of a 2D network. This coordination polymer is also suitable as catalyst for a solvent-free, one-pot, 3-component coupling reaction involving various aromatic and aliphatic aldehydes, terminal alkynes and aliphatic cyclic secondary amines (called an A^3 reaction) in order to synthesize a large series of propargylamine derivatives (**Figure 23**). The authors proposed a mechanism in which the 4-cooridnated intermediate "$(\sim S)(R\text{-}C{\equiv}C^{-})Cu(\mu\text{-}I)_2Cu(S\sim)_2$" releases the $R\text{-}C{\equiv}C^{-}$ nucleophile, which attacks the iminium ion formed by the aldehyde and amine.

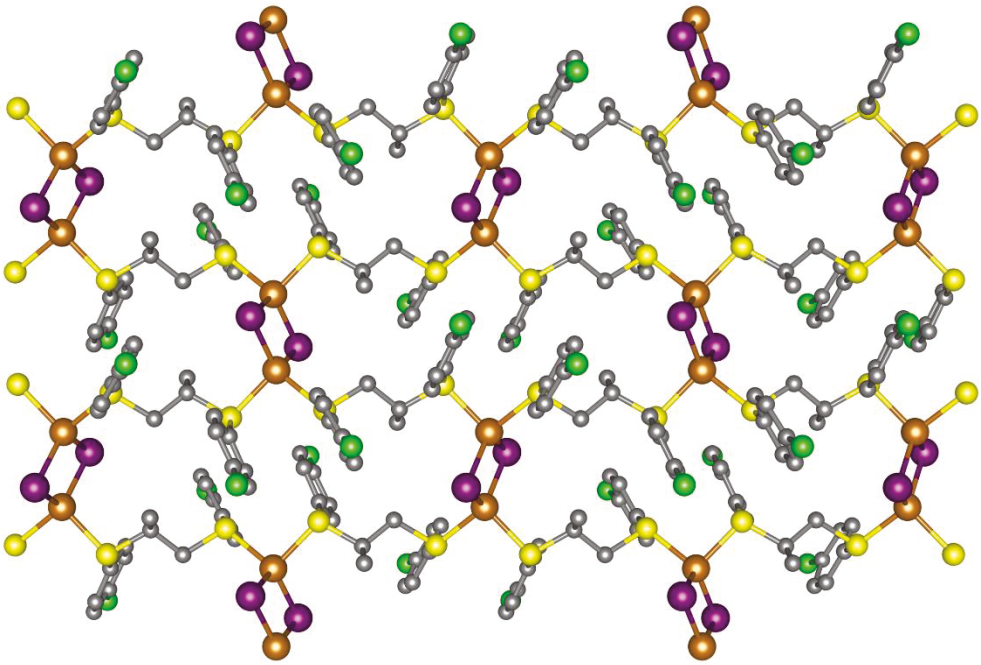

Figure 22. X-ray structure of a fragment of the 2D arrangement of the $[Cu_2I_2(\mathbf{L17})_2]_n$ coordination polymer. Cu, orange; I, purple; S, yellow; Cl, green; C, grey. The image was reproduced using the cif files from the Cambridge Crystallographic Data Centre; CCDC number: 1873371.

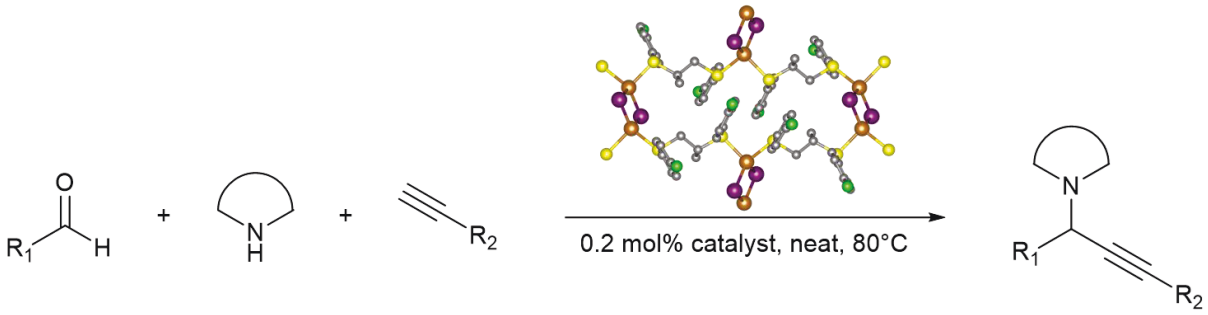

Figure 23. Reaction scheme for the A^3 reaction and the optimum experimental conditions.

The use of selenide- and telluride-containing coordination polymers and a cluster for catalytic purposes was also made.[36] Indeed, Jing *et al*. prepared four ferrocenylchalcogenoether ligands (FcTeTeFc (**L18**), $FcTeCH_2TeFc$ (**L19**), $FcSeCH_2SeFc$ (**L20**) and $FcSeCH_2C_6H_4CH_2SeFc$ (**L21**); Fc = ferrocennyl) and from CuX salts (X = Br, I), and six novel copper(I) halide-based materials, which were successfully characterized by X-ray crystallography (**Figure 24**). The 1D coordination polymers are structurally reminiscent to that of the ladder-type skeleton shown in **Figure 21**. The

catalytic activities of these coordination polymers and a cluster were then investigated in the Ullmann C-N cross-coupling reaction between imidazole and iodobenzene under different conditions (**Figure 25**). The best performances were found for 0D $[Cu_4I_4(\mathbf{L18})_2(MeCN)_2]$ and 1D $[Cu_2I_2(\mathbf{L19})_2]_n$ in DMSO (dimethyl sulfoxide) at 110°C using 10 mol % loading and KOH as a base. The observed conversions based on gas chomatography analysis were 87.3 and 91.3 %. The mechanism was not specifically addressed but the authors stated that a low steric environment around the Cu(I) center in the Cu_2I_2 rhomboid maybe a critical condition during the catalytical cycle, which would allow both imidazole and iodobenzene to coordinate the metal in a stepwise fashion and effectively provide the target product.

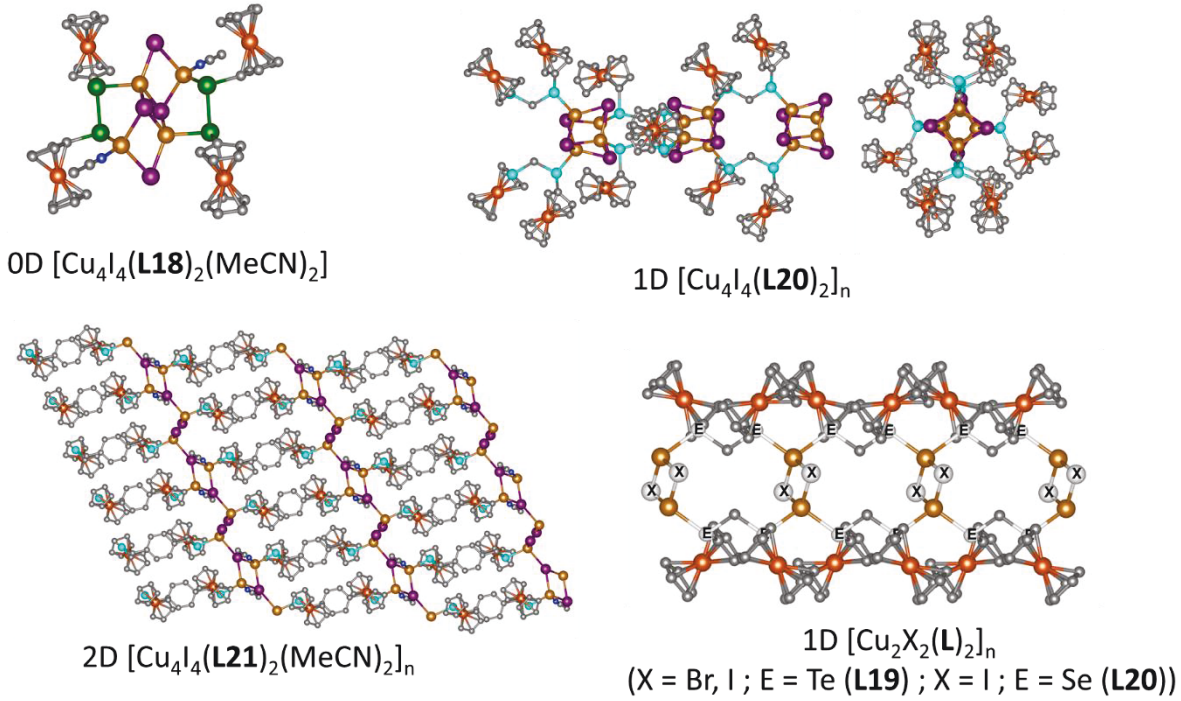

Figure 24. Structures of $[Cu_4I_4(\mathbf{L18})_2(MeCN)_2]$, $[Cu_2I_2(\mathbf{L19})_2]_n$, $[Cu_2Br_2(\mathbf{L19})_2]_n$, $[Cu_2I_2(\mathbf{L20})_2]_n$, $[Cu_4I_4(\mathbf{L20})_2]_n$, and $[Cu_4I_4(\mathbf{L21})_2(MeCN)_2]_n$. Cu, orange; I, purple; Fe, brown; N, nitrogen; Te, green; Se, cyan; C, grey; White, halide (X = Br, I). The images were reproduced using the cif files from the Cambridge Crystallographic Data Centre; CCDC numbers: 1418326, 1418330, 1418331, 1418329 and 1418328.

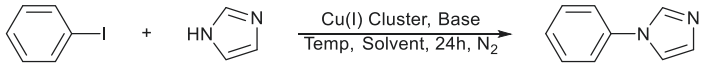

Figure 25. Tested copper(I) species catalyzed C-N coupling reaction.

In continuation with this work, this same group subsequently investigated other telluride-containing coordination polymers.[37] Indeed, in addition to the 0D $[Cu_4I_4(\mathbf{L18})_2(MeCN)_2]$, 1D $[Cu_2I_2(\mathbf{L19})_2]_n$, and 1D $[Cu_2Br_2(\mathbf{L19})_2]_n$ materials, this recent report included three new telluride ligands (**L22**, **L23** and **L24**) and five new 0-2D Cu_2X_2-containing species (X = Br, I). The former ligand generates 0D species $[Cu_2Br_2(\mathbf{L22})_2]$ and $[Cu_2I_2(\mathbf{L22})_2]$, which respectively exhibit bridging and chelating ligand bindings (**Figure 26**), whereas the second one leads to the formation of the 2D coordination polymers $[Cu_2X_2(\mathbf{L23})_2]_n$ (X = Br, I), also reminiscent to that presented in **Figure 26**. Finally, the third ligand led 1D coordination polymer $[Cu_2I_2(\mathbf{L24})_2]$ exhibiting the $\cdots Cu_2I_2(\mu\text{-ligand})_2Cu_2I_2(\mu\text{-ligand})_2\cdots$ organisation. All eight materials in 10 mol % loadings were tested for the same Ullmann C-N cross-coupling reaction shown in **Figure 25**. Interestingly, the comparison of the isolated yields between 110°C, DMSO, 24h, *t*-BuOLi as the base, *vs* 85°C, poly(ethylene glycol) (*i.e.* PEG-400), 12h, and *t*-BuOLi as the base for conditions, were systematically slightly to significantly better for the second series (80 to 99 % isolated yields). The use of poly(ethylene glycol) (in low molecular weight) is viewed as a greener alternative for organic solvent and can easily be recycled. Other imidazole substrates were also investigated, and the isolated yields were also very good (87 to 99 %, here for $[Cu_2I_2(\mathbf{L22})_2]$). The proposed stepwise mechanism, supported by spectroscopic measurements, involves a proton-coupled electron transfer a from Cu(I) and a proton from imidazole resulting in the formation of a labile penta-coordinated Cu(II) and aryl radical, then followed by an effective electron transfer from the ferrocene arm to reduce Cu(II) and forms the Ullman C-N coupled product involves (**Figure 27**). Finally, the ferrocenium unit is subsequently reduced by the I^- anion.

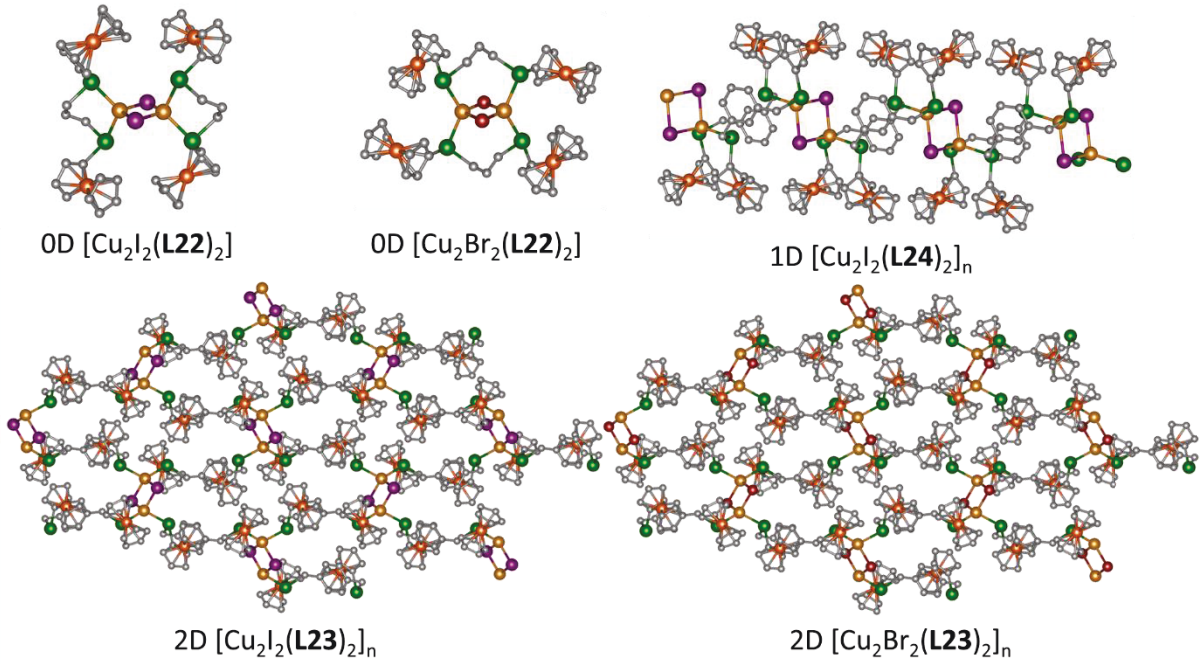

Figure 26. Structures of $[Cu_2Br_2(\mathbf{L22})_2]$, $[Cu_2I_2(\mathbf{L22})_2]$, $[Cu_2Br_2(\mathbf{L23})_2]$, $[Cu_2I_2(\mathbf{L23})_2]$ and $[Cu_2I_2(\mathbf{L24})_2]$. Cu, orange; I, purple; Br, deep red; Fe, brown; N, nitrogen; Te, green; C, grey. The images were reproduced using the cif files from the Cambridge Crystallographic Data Centre; CCDC numbers: 1823304-1823308.

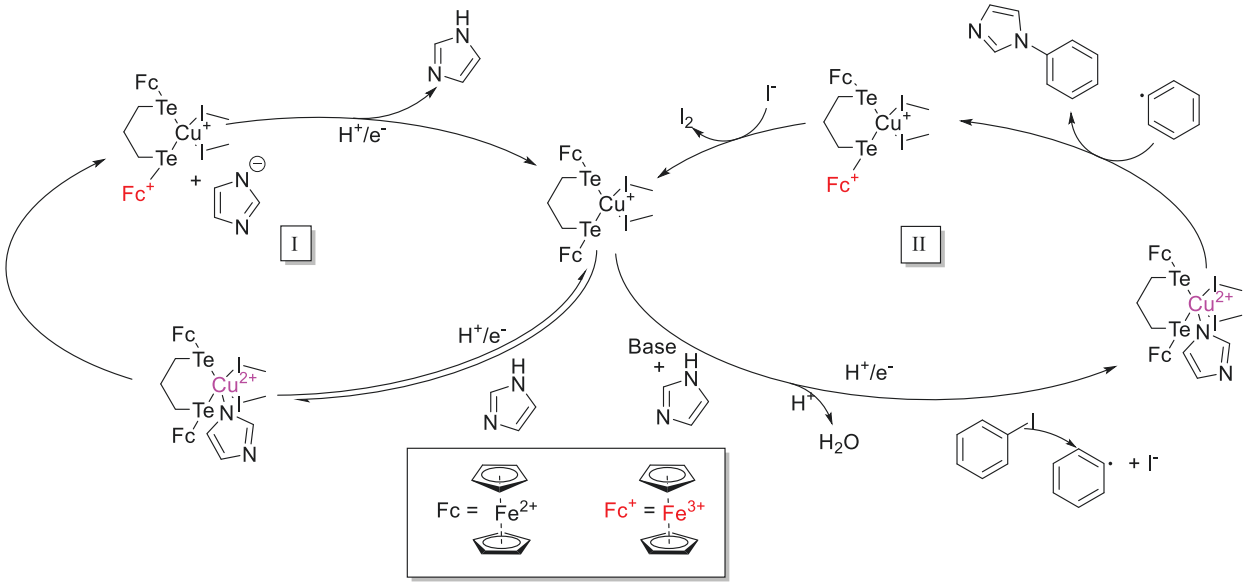

Figure 27. Proposed mechanism for the catalysed C-N coupling reaction.

CuX/thiourea-based catalysis has also been observed. Indeed, Roesky *et al.* reported the synthesis of the thiourea ligand Ar'NHC(S)NHC(O)Ar (Ar' = 2,6-*i*Pr$_2$C$_6$H$_3$; Ar = *p*-*t*-BuC$_6$H$_4$ (**L25**)) and some its 0D complexes of CuX salts (X = Br, I).[38] Together, they formed adamantane-shaped complexes of general formula [Cu$_4$X$_4$(**L25**)$_4$] (X = Cl, Br) or [Cu$_2$I$_2$(**L25**)$_2$] (**Figure 28**). In the presence of hydrogen peroxide, these complexes catalyze the oxidation of alcohols to the carbonyl compounds, including 1-phenylethanol into acetophenone. At 20°C, the conversion is rather modest (17-46 %) but increases to 63-67 % at 70°C.

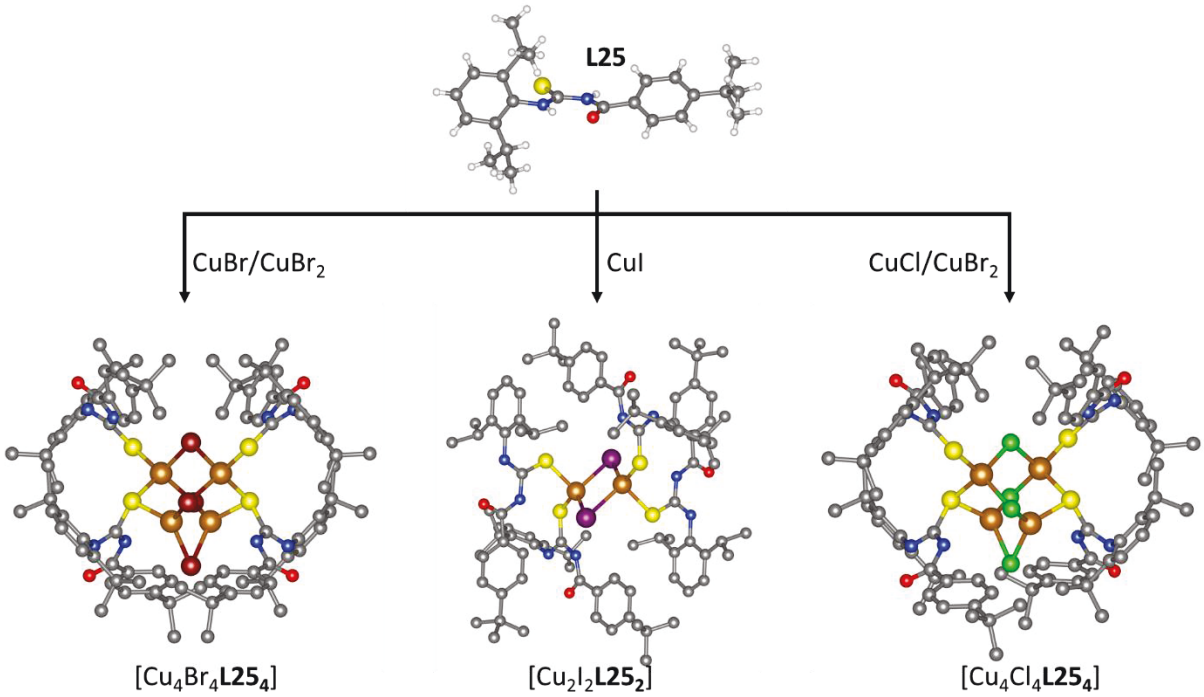

Figure 28. X-ray structures of ligand **L25** and the 0D complexes [Cu$_4$Br$_4$**(L25)**$_4$], [Cu$_4$I$_4$**(L25)**$_4$], and [Cu$_2$I$_2$**(L25)**$_2$]. Cu, orange; I, purple; Br, deep red; S, yellow; O, red; N, blue; Cl, green; C, grey. The images were reproduced using the cif files from the Cambridge Crystallographic Data Centre; CCDC numbers: 1450698 and 1450705-1450707.

2.6. Photocatalysis

The application of the chalcogenoether- and chalcogenone-containing halogenocopper(I) materials as photocatalysts has only recently attracted attention. The 3D [Cu$_4$I$_4$(**L10**)$_5$]$_n$ framework (EBT = 3-ethyl-1,3-benzothiazole-2-thione (**L10**)) used as a sensor for antibiotic (described above[24]), can also be used as a promising semiconductor photocatalyst for the degradation of organics contained

in water.[39] This coordination network is insoluble in ethanol, acetonitrile and acetone, and is stable in water up to 24 h. Moreover, the absorption spectrum of this 3D polymer exhibits a maximum near 420 nm and expand well from 480 to 700 nm, which makes this material potentially useful for applications using visible light. The authors used rhodamine B (RhB) as a model pollutant and compared its photodegradation to that when using nitrogen-doped TiO_2 nanoparticles (N-TiO_2) as photocatalyst under a 300 W Xenon lamp as a simulated solar light source. Kinetic experiments under identical experimental conditions showed absence of catalytic activity in the dark or in the absence of catalyst. Conversely, in the presence of catalyst and under irradiation, the photodegradation of RhB occurs and the 3D-$[Cu_4I_4(\mathbf{L10})_5]_n$ coordination polymer is found significantly more efficient than N-TiO_2 (*i.e.* by a factor of three). Moreover, the process is found repetitive upon cycling several times. Trapping experiments using isopropanol, benzoquinone and ammonium oxalate as scavengers of hydroxide radical •OH, superoxide radical $\bullet O_2^-$, and $hole^+$, respectively, were performed. The latter additive significantly inhibited the photocatalytic activity thus indicating that the process is dominated by the presence of holes. The authors also indicated that this coordination polymer represents the first tetranuclear Cu(I) iodine cluster used for visible-light driven photocatalytic application.

Concurrently, the use of selenoether ligands to design selenoether-containing Cu(I) nanoparticles (labelled in the text as Cu_2-xSe) and composites with TiO_2 was also made.[40] During the synthesis of the nanoparticles, which were performed under mild conditions, intermediate molecular species were isolated and characterised by X-ray diffraction (**Figure 29**). The preparation of the nanocomposites with different Cu/Ti ratios consisted in refluxing $Cu(TFA)_2$ (TFA = trifluoroacetic acid) and *t*-Bu_2Se (**L26**) in toluene in the presence of commercial TiO_2 (type P25 (Rutile/Anatase: 85/15), average diameter = 20 nm). The powder XRD patterns indicated that the composites consisted of the TiO_2 as the major component. BET measurements showed that they could adsorb between 150 (without selenoether-containing Cu(I) materials) and 200 cm^3g^{-1} of gas at STP (standard temperature and pressure) (with selenoether-containing Cu(I) materials) at STP in the Kubelka–Munk plots (type IV isotherms) having a small hysteresis between 0.85 and 1.0 P/P°. These nanoparticles were tested for the photodegradation of formic acid in water. Expectedly, no activity was observed in the dark but upon irradiation (125 W high-pressure mercury vapor lamp and a cut off filter at $\lambda > 350$ nm with a radian flux of ~ 4.1 $mW.cm^{-2}$), the photodegradation of formic acid was observed. The selenoether-containing Cu(I) materials showed very little activity

compared to that of the TiO_2 alone. However, when combined as a composite nanoparticle, the activity increased sensibly for relative compositions of 0.1 and 0.3 % Cu_2-xSe *vs* TiO_2. This improved efficiency was attributed to an enhanced light absorption property and an increased number of charge-separated pairs (e^--h^+). This charge transfer process is defined as thermodynamically favored since both the conduction and valence bands of the Cu_2-xSe component lie above those for TiO_2, thus preventing efficient recombination. The mechanism consists of the formation of superoxide radical $\cdot O_2^-$ and hole$^+$, which in turn generate HCOO• radicals when in contact with the formic acid, decomposing into CO_2. The $\cdot O_2^-$ radical combines with H^+ to form $HO_2\cdot$.

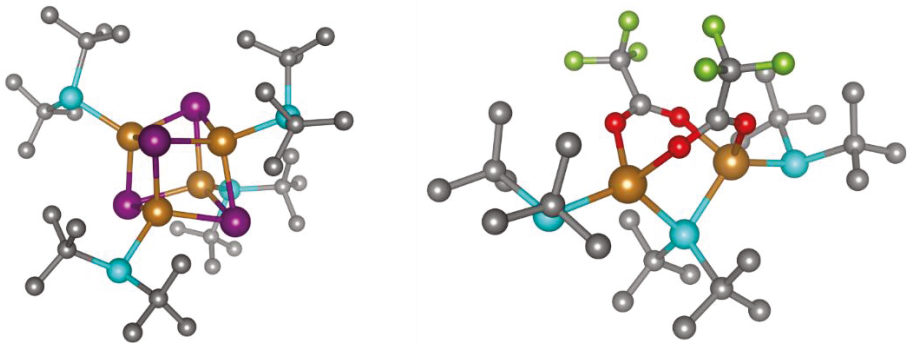

Figure 29. X-ray structures of $[Cu_4I_4(\mathbf{L26})_4]$ (left) and $[Cu_2(TFA)_2(\mathbf{L26})_3]$ (right). Cu, orange; I, purple; Se, cyan; F, light green; O, red; C, grey. The images were reproduced using the cif files from the Cambridge Crystallographic Data Centre; CCDC numbers: 1835505 and 1835506.

In a similar manner, another TiO_2-based nanocomposite was investigated.[41] The authors prepared a 1D coordination polymer of general formula $[Cu_2I_2(\mathbf{L27})_2]_n$ (**L27** = 9-(3-phenylselanyl-2-phenylselanylmethylpropyl)anthracene) where the SBU is a rhomboid. In the solid state, supramolecular face-to-face anthracenyl•••anthracenyl contacts of 3.58 Å are depicted in the crystal. The construction of *in situ* core-shell TiO_2-$[Cu_2I_2(\mathbf{L27})_2]_n$ proceeds in two steps as shown in **Figure 30**. The morphology of the TiO_2-$[Cu_2I_2(\mathbf{L27})_2]_n$ material was assessed by high resolution transmission electron microscopy. The surfaces exhibited well-defined lattice fringes in both the TiO_2 substrate and 1D-$[Cu_2I_2(\mathbf{L27})_2]_n$ coordination polymer, respectively spaced by 0.32 and 0.21 nm. These values are equal to the lattice parameter in the (110) face of the anatase and the (115) face of the 1D coordination polymer. A layer of coordination polymer of ~2.90 Å is coated on the TiO_2 surface of the nanoparticles. This distance corresponds to two 1D chains with cofacial π–π

anthracenyl•••anthracenyl interactions. The photocatalytic activity of this coated hybrid TiO_2 materials involves the reduction of Cr(VI) into Cr(III) in water using colorimetric method (λ = 540 nm), in order to evaluate its photoreduction ability (λ > 400 nm; using a metal halide lamp and filtered with a 1M $NaNO_2$ solution, light intensity 300 mW/cm^2). Uncoated mix of TiO_2 and $[Cu_2I_2(\mathbf{L27})_2]_n$ TiO_2 alone, $[Cu_2I_2(\mathbf{L27})_2]_n$ alone and TiO_2-(**L27**) (**Figure 30**) did not show any significant photocatalytic activity over a period of 2.5 h. Conversely, the coated TiO_2-$[Cu_2I_2(\mathbf{L27})_2]_n$ material completed the photocatalytic reduction of Cr(VI) ions into Cr(III) in 2 h, but some decrease in conversion rate was noted after several cycles. This efficiency is due to the formation of a charge separated state upon irradiation. The excited state oxidation potential, E_{ox}*, of $[Cu_2I_2(\mathbf{L27})_2]_n$ is evaluated to be -2.6 V (*vs* NHE) and the onset of the absorption spectrum, E_g is 2.8 eV. This thermodynamic information led to the proposition of the mechanism in **Figure 31**.

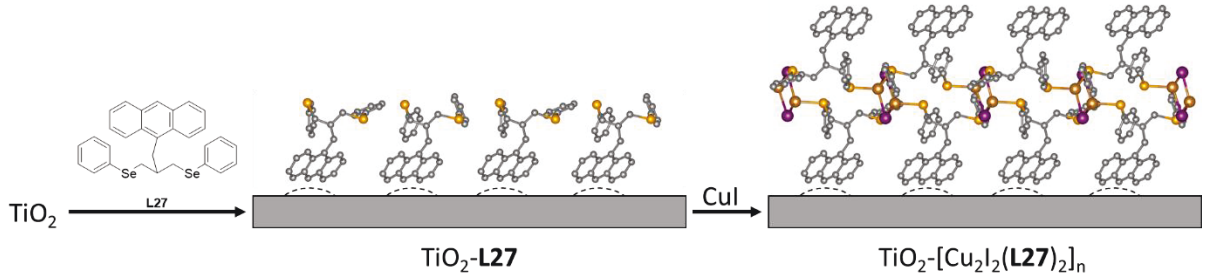

Figure 30. Reaction scheme showing the *in situ* synthesis of TiO_2-(**L27**) and TiO_2-$[Cu_2I_2(\mathbf{L27})_2]_n$. Cu, orange; I, purple; Se, yellow; F, light green; O, red; C, grey. The images were reproduced using the cif files from the Cambridge Crystallographic Data Centre; CCDC numbers: 1469260 and 1469261.

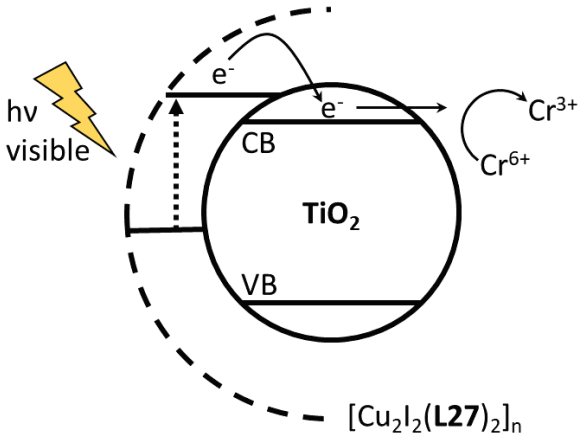

Figure 31. Proposed mechanism.

A series of ferrocenyltelluroether-containing cuprous halide clusters were also investigated as molecular photocatalysts for C-H arylation (**Figure 32**) conducted under white light irradiation in air and at room temperature.[42] These catalysts are shown in **Figure 33**. In DMSO, the isolated yields varied from 40 to 86 %, with the red-looking **cluster 1** being the best. The change of solvent did not improve the yield, but rather decreased it. Using various substituted iodobenzene derivatives and using **cluster 1** as the catalyst in DMSO, similar isolated yields were reported (75 to 86 %). A detailed mechanism investigation suggested that the Cu(I) cluster, upon irradiation with visible light, promotes a proton-coupled electron transfer during which the electron from excited Cu(I) migrates together with the proton from benzothiazole, forming a benzothiazolate-coordinated Cu(II) intermediate species and an aryl radical (**Figure 34**). Subsequently, the electron transfer from the ferrocene pendent group to the metallic Cu(II) unit releases the reactive benzothiazolate to generate the final organic product with an aryl radical.

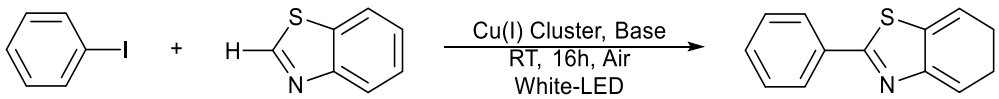

Figure 32. Reaction pathway for the C-H arylation catalyzed by ferrocenyltelluroether-containing cuprous halide clusters (the model reaction condition: iodobenzene (1.25 mmol), benzothiazole (0.25 mmol), copper clusters and coordination polymers (20 mol % Cu), *t*-BuOLi (0.75 mmol), solvent (2.0 mL).

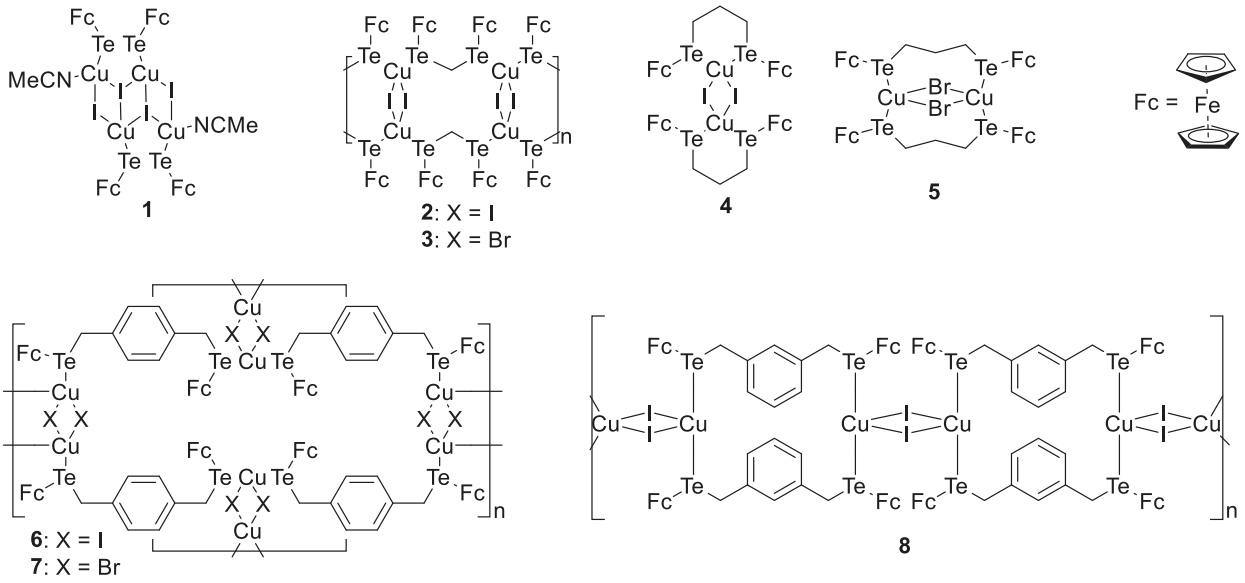

Figure 33. Molecular structures of the catalysts. Modified from ref 42.

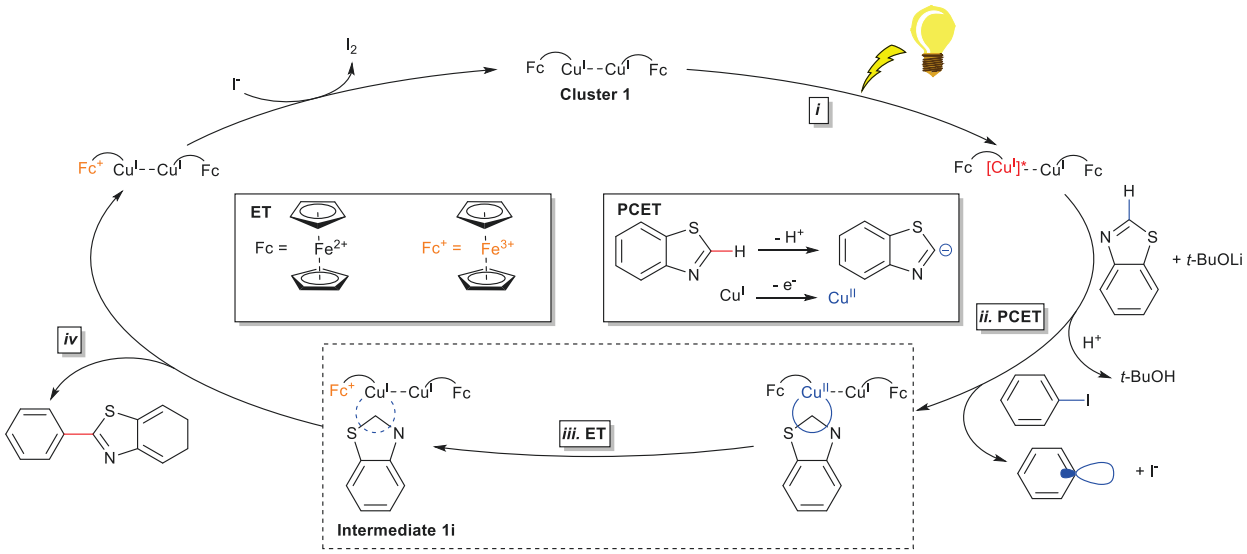

Figure 34. Proposed mechanism. Modified from ref 42.

2.7. Electroactive materials

The presence of Cu(I) centers in the coordination polymers renders these materials potentially electroactive (Cu(I) → Cu(II) + 1e⁻). For example, Amirnasr *et al*, investigated the 1D-coordination polymers $[Cu_2(\mu\text{-}Br)_2(\mu\text{-}(4\text{-}NO_2Ph)_2(\mathbf{L28})]_n$, $[Cu_2(\mu\text{-}I)_2(\mu\text{-}(4\text{-}NO_2Ph)_2(\mathbf{L28})]_n$, and $[Cu_2(\mu\text{-}I)_2(\mu\text{-}(thio)_2(\mathbf{L29})]_n$ (**L28** = *N*,*N*'-bis(4-nitrobenzaldimine)-1,2-bis(o-aminophenylthio)-ethane and **L29** = *N*,*N*'-bis(thiophenedimine)-1,4-bis(o-aminophenylthio)xylene) (**Figure 35**).[43]

The coordination polymers were obtained from the direct reaction of their corresponding ligands and CuX (X = Br, I) in a toluene/mixture. $[Cu_2(\mu\text{-}I)_2(\mu\text{-}(4\text{-}NO_2Ph)_2(\mathbf{L28})]_n$ and $[Cu_2(\mu\text{-}I)_2(\mu\text{-}(thio)_2(\mathbf{L29})]_n$ were characterized by X-ray crystallography, and $[Cu_2(\mu\text{-}Br)_2(\mu\text{-}(4\text{-}NO_2Ph)_2(\mathbf{L26})]_n$ and $[Cu_2(\mu\text{-}I)_2(\mu\text{-}(4\text{-}NO_2Ph)_2(\mathbf{L28})]_n$ are assumed to be isostructural. The cyclic voltammograms (CVs) were obtained using DMSO as solvent and a scan rate of 100 mV s^{-1}. The CVs are characterized by two irreversible waves at +0.38 and +0.79 V ($[Cu_2(\mu\text{-}Br)_2(\mu\text{-}(4\text{-}NO_2Ph)_2(\mathbf{L28})]_n$), +0.26 and +0.62 V ($[Cu_2(\mu\text{-}I)_2(\mu\text{-}(4\text{-}NO_2Ph)_2(\mathbf{L28})]_n$), and +0.27 and +0.42 V vs ($[Cu_2(\mu\text{-}I)_2(\mu\text{-}(thio)_2(\mathbf{L29})]_n$), both being associated with the Cu(I)-Cu(I) ↔ Cu(II)-Cu(II) process. Because the ligands are not prone to electronic communication between the two copper centers, these waves are due to partial solvolysis (**Figure 36**). The integrity of the coordination polymer changes upon dissolving the material splitting in shorter soluble oligomers. This general fact in coordination chemistry causes uncertainties in the interpretation. On the other hand, if the coordination polymer is stabilized onto an electrode surface, the interpretation becomes unambiguous. Indeed, in the previous section (photocatalysis), the $[Cu_2I_2(\mathbf{L27})_2]$ coordination polymer (**L27** = 9-naphthyl-$CH_2CH(CH_2SePh)_2$) was described. This coordination polymer was immobilized onto the electrode surface and the resulting CV exhibited a single quasi-reversible oxidation wave at 1.278 V (in DMF, vs Ag/Ag+ in 0.01 M $AgNO_3$ in MeCN as reference electrode).[41]

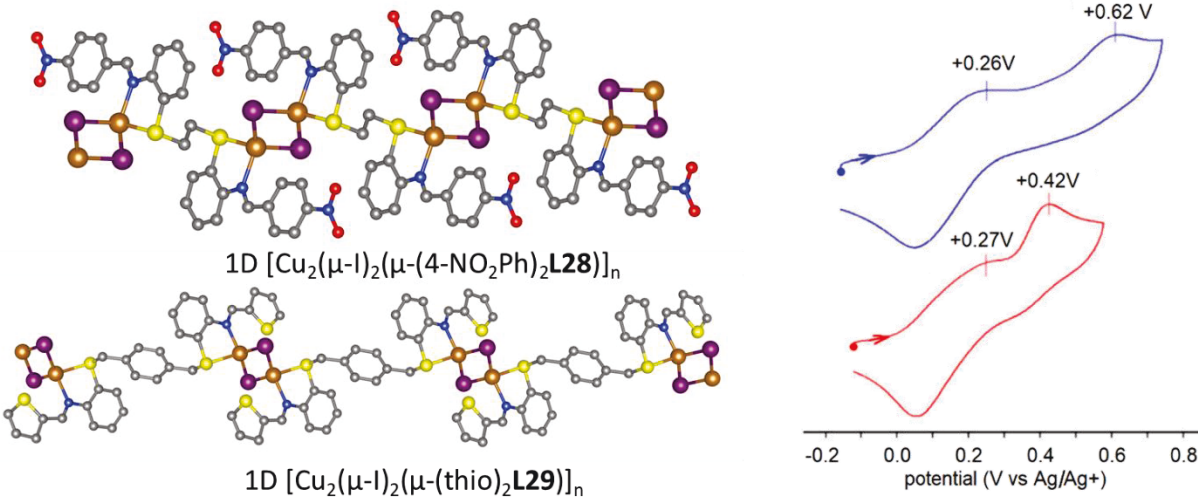

Figure 35. Left: X-ray structures of 1D $[Cu_2(\mu\text{-}I)_2(\mu\text{-}(4\text{-}NO_2Ph)_2\mathbf{L28})]_n$ (top) and 1D $[Cu_2(\mu\text{-}I)_2(\mu\text{-}(thio)_2\mathbf{L29})]_n$ (bottom). Cu, orange; I, purple; S, yellow; N, blue; C, grey. The images were reproduced using the cif files from the Cambridge Crystallographic Data Centre; CCDC numbers:

851506 and 851511. Right: Corresponding CVs in DMSO solutions of these polymers (scan rate = 100 mV s^{-1}; c 4 x 10^{-3} M). Adapted with permission from *J. Coord. Chem.*, 2013, **66**, 1974–1984. Copyright (2013) Taylor & Francis.

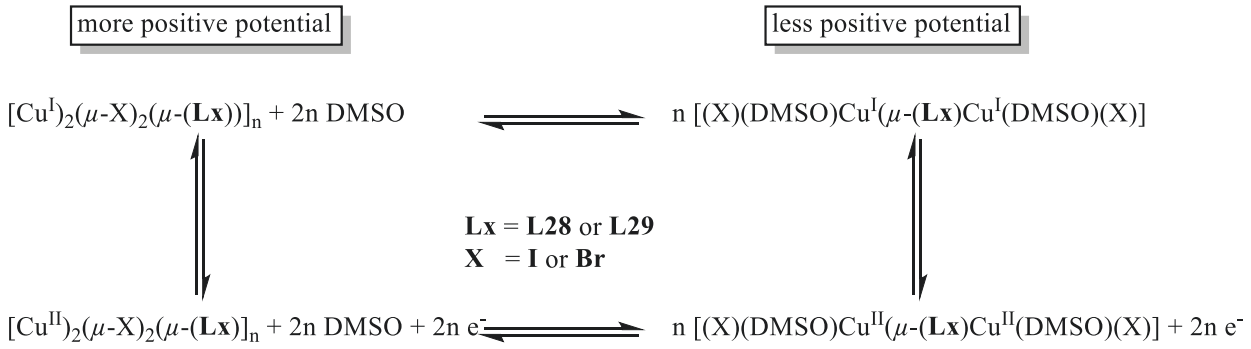

Figure 36. Solvolysis and electrochemical processes in DMSO solutions of 1D polymers $[Cu_2(\mu\text{-}Br)_2(\mu\text{-}(4\text{-}NO_2Ph)_2(\mathbf{L28})]_n$, $[Cu_2(\mu\text{-}I)_2(\mu\text{-}(4\text{-}NO_2Ph)_2(\mathbf{L28})]_n$, and $[Cu_2(\mu\text{-}I)_2(\mu\text{-}(thio)_2(\mathbf{L29})]_n$.

Electrochemical investigations of polythioether ligands in the presence of Cu(I) ions were also reported.[44] Indeed, the tri- and dithioethers tris(2-tert-butyl-4-methylphenylthiomethyl)amine (**L30**), bis(2,4-dimethylphenylthio)methane (**L31**), and bis(2-tert-butyl-4-methylphenylthio) methane (**L32**) were studied (in CH_3CN, 1 mM, V *vs* Fc/Fc^+, scan rate = 0.1 V s^{-1}) in the absence and the presence of Cu(I) ions. The electrochemical data of the ligands alone are provided in **Table 3** (all peaks are irreversible). Upon adding Cu(I) ions under the form $[Cu(CH_3CN)_4]ClO_4$ (*i.e.* without a halide anion), the reduction peak associated with Cu(I) + $1e^- \leftrightarrow$ Cu(0) appeared in the CVs. For **L31**, this peak was found at -1.07 V, which represents a 105 mV shift towards more negative potential (without the ligand this potential is -0.97 V) thus witnessing the presence of coordination with the electron rich thioether. For **L30** and **L32**, these shifts were 202 and 14 mV, respectively, suggesting that the complex formed with **L30** is more stable. Using CuI as additive, the authors stated that the CVs became very complex in the anodic region. This observation may be associated with the formation of several ill-defined oligomers as similarly found for the 1D-coordination polymers $[Cu_2(\mu\text{-}Br)_2(\mu\text{-}(4\text{-}NO_2Ph)_2(\mathbf{L28})]_n$, $[Cu_2(\mu\text{-}I)_2(\mu\text{-}(4\text{-}NO_2Ph)_2(\mathbf{L28})]_n$, and $[Cu_2(\mu\text{-}I)_2(\mu\text{-}(thio)_2(\mathbf{L29})]_n$ discussed above. However, the main conclusion of this contribution is that the thioether ligands are also prone to be redox active.

Table 3. Redox potentials of the ligands **L30**-**L32** (V, *E vs.* Fc^+/Fc; ap = anodic peak).

	I^{ap}	II^{ap}	III^{ap}	IV^{ap}	V^{ap}
L30	0.65	1.04	1.42	1.61	1.96
L31	0.92	1.08	1.63	2.02	-
L32	0.95	1.53	1.92	-	-

Concurrently, soluble discrete complexes are more reliably characterized, and could be used as model for their corresponding coordination polymers. An example for this is provided by the 0D-complex $[Cu_2Br_2(\mathbf{L33})_2]$ where **L33** is 1-oxa-4,7-dithiacyclononane (**Figure 37**).[45] This complex in CH_3CN (1 mM with 0.1 M of NEt_4ClO_4), exhibits a single quasi-reversible wave at +0.594 *vs* Fc/Fc^+ (ΔE_p = 107 mV; scan rates = 40-160 mV s^{-1}). The authors stated that the CV properties of this Cu complex is similar to that of the corresponding 1,4,7-trithiacyclononane complexes of Cu(I). This conclusion supports that soluble discrete models can mimic adequately the electrochemical behavior of insoluble chalcogenoether-containing Cu(I) complexes and coordinaiton polymers.

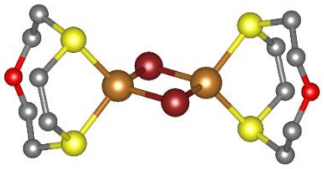

Figure 37. Structure of $[Cu_2Br_2(\mathbf{L33})_2]$. Cu, orange; Br, deep red; S, yellow; O, red; C, grey. The image was reproduced using the cif files from the Cambridge Crystallographic Data Centre; CCDC numbers: 1222362.

In the category of selenone-species (**Figure 38**), the rhomboid $[Cu_2X_2]$-containing complexes $[Cu_2X_2(\mathbf{L34})_4(CuX)_2]$ (X = Br, I) were also investigated.[46] These complexes were investigated in CH_3CN (1 mM, 0.1 M $(NBu_4)_2PO_4$, Ag/AgCl reference electrode reported against NHE electrode, $E_{½} = (E_{ap} + E_{cp})/2$; ap = anodic peak, cp = cathodic peak). The particularity of these complexes is that they also bear two mononuclear CuX units. Thus unsurprisingly, two oxidation processes are depicted and their oxidation waves are found irreversible ($Cu(I) \leftrightarrow Cu(II) + 1e^-$). However, specific assignments for these electrochemical processes were not provided. Conversely, the CV traces of these two complexes showed three distinct reduction waves (*i.e.* return waves). Two of the waves correspond to $Cu^{2+}/^+$ and $Cu^+/0$ redox processes. The third reduction peak is due to I^-/I_2 or Br^-/Br_2 reduction couples as it is suspected that these halides dissociate in solution and the

vacant sites are occupied by solvent molecules. In the differential pulse voltammetry experiments, both complexes exhibit two distinct reduction and oxidation peaks. These processes correspond to $Cu^{2+/+}$ and their respective halogen redox processes. Overall, these complexes exhibit a single $Cu^{2+/+}$ reduction peak at a potential of - 452 and -365 mV, respectively for X = Br and I, despite having two different copper centers with different geometries.

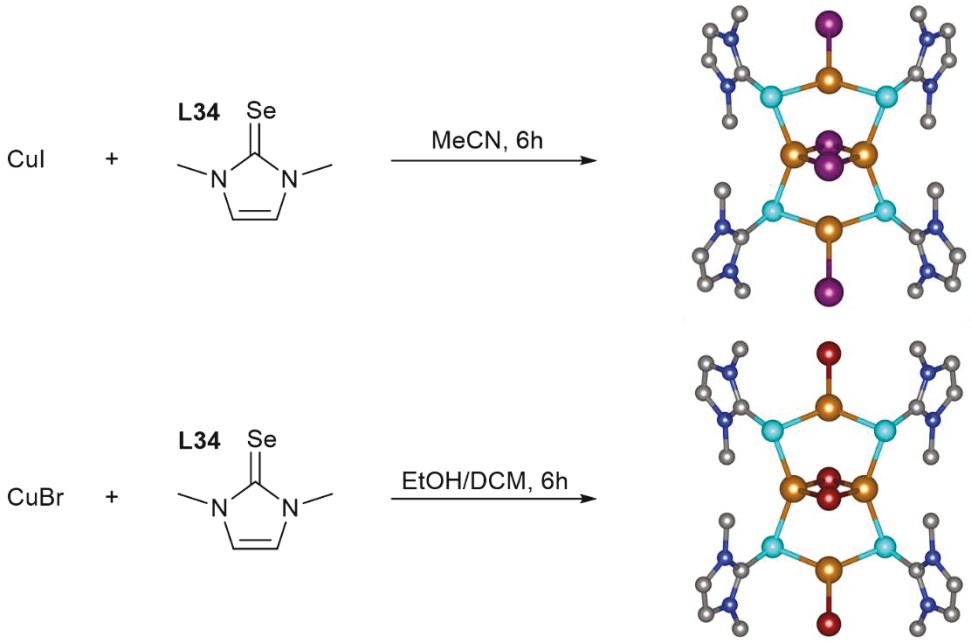

Figure 38. Structures of $[Cu_2X_2(\mathbf{L34})_4(CuX)_2]$ complexes (X = Br, I). Cu, orange; I, purple; Br, deep red; Se, cyan; N, blue; C, grey. The images were reproduced using the cif files from the Cambridge Crystallographic Data Centre; CCDC numbers: 804911 and 804917.

Table 4. Reduction potentials of $Cu^{2+/+}$ and $Cu^{+/0}$ for the $[Cu_2X_2(\mathbf{L34})_4(CuX)_2]$ complexes *vs.* NHE.

	$Cu^{2+/+}$				$Cu^{+/0}$			
X	E_{pa} (mV)	E_{pc} (mV)	ΔE (mV)	$E_{1/2}$ (mV)	E_{pa} (mV)	E_{pc} (mV)	ΔE (mV)	$E_{1/2}$ (mV)
X = I	83, -235	0, -986	1069	-452	-866	-1355	49	-1111
X = I[a]	34, -285	126, -664	92, 379	80, -475				
X = Br	-39, -178	-644	605	-342	-881	-1274	393	-1078
X = Br[a]	-106, -245	-42, -626	64, 381	-74, -436				

[a]Differential pulse voltammetry results.

In conclusion, the presence of redox activity where metal-centered (Cu(I) ↔ Cu(II) + $1e^-$), ligand-centered and even halide-centered processes are all possible and makes the copper halide-chalcogenoether and -chalcogenone coordination polymers and networks prone to electron-driven

devices. A clear evidence for this is the design of a light emitting diode with the MOF containing a Cu_2I_2-rhomboid secondary network presented above (see section presenting several sensors).[26] This MOF contains Ln^{3+} ions which are photo- and electroluminescent.[9] These investigated Ln^{3+} ions are Eu, Tb, and Eu/Tb mixture in a 1:18 Ln^{3+}/ligand ratio during the synthesis. The corresponding Commission Internationale de L'Eclairage (CIE) coordinates are (0.26, 0.42), (0.31, 0.33), and (0.41, 0.22), respectively. The third framework material (*i.e.* Eu/Tb mixture) in this list was used to design a white-light-emitting device. The solid product synthesized with an Eu/Tb molar ratio of 1:10, exhibits a fluorescence quantum efficiency of 5.6 %.

2.8. Conducting solids

The electric conducting properties of neutral copper halide-thioether and thione networks have been known since 1996 and several investigations were reported in the past few years. In 1996, Nakagawa *et al.* reported the synthesis and properties of the coordination polymers $[Cu_2Br_2(\mathbf{L11})(MeCN)_2]_n$ and $[Cu_2I_2(\mathbf{L11})_2]\cdot THF\}_n$ (**L11** = 2,11-dithia[3.3]paracyclophane) including their electric conductivity upon doping with iodine.[47] The structure of the former polymer consists of a 1D-chain whereas the latter coordination network exhibits a layered structure (**Figure 39**). At room temperature, when doped with iodine, these coordination polymers exhibit electric conductivity of respectively $10^{-5.9}$ and $10^{-5.1}$ S cm^{-1}, which is in the range of semi-conducting materials.

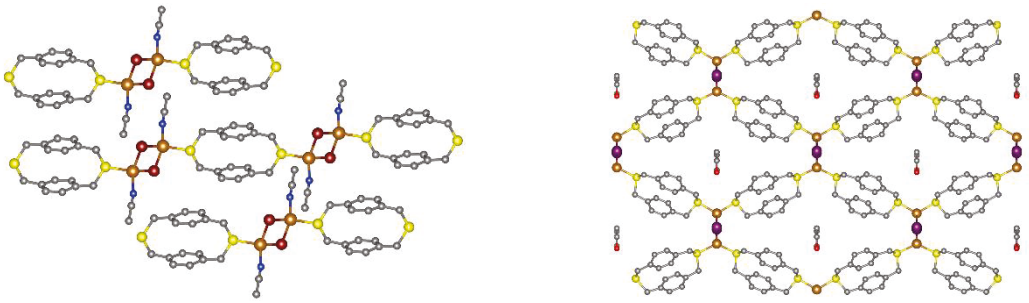

Figure 39. Structures of 1D-$[Cu_2Br_2(\mathbf{L11})(MeCN)_2]_n$ (left) and 2D-$[Cu_2I_2(\mathbf{L11})_2]\cdot THF\}_n$ (right) coordination polymers. Cu, orange; I, purple; Br, deep red; O, red; S, yellow; N, blue; C, grey. The images were reproduced using the cif files from the Cambridge Crystallographic Data Centre; CCDC numbers: 1316860-1316861.

In the category of thione-containing materials, a 1D coordination polymer was also investigated in a similar fashion in these earlier days.[48] The structure of this $[Cu_4I_4(\mathbf{L35})_4]_n$ coordination

polymer is shown in **Figure 40** where the ligand is 4,5-ethylenedithio-1,3-dithiole-2-thione (**L35**). The SBU consists of staircase Cu_4I_4 motif. The authors stressed on the presence of a short S•••S distance of 3.257(2) Å. This polymer is insulating at room temperature (conductivity $\sigma(25°C) < 10^{-12}$ S cm^{-1}), but upon slow exposition of I_2 vapor, a partial oxidation ($Cu(I) \rightarrow Cu(II) + 1e^-$) occurs to form an orange material formulated as $[Cu_4I_4(\mathbf{L35})_4]I_x$. The latter has been characterized by solid state IR ($\nu(C=S) = 1477\ cm^{-1}$) and UV-vis spectroscopy ($\lambda_{max} = 475$ nm, a band extending far in the visible region). This latter band has been assigned to a metal-to-ligand charge transfer (MLCT). Conductivity measurements of this mixed valence species indicated the presence of a semiconducting material ($\sigma(25°C) = 2.2 \times 10^{-4}$ S cm^{-1}). The proximity of the sulfur rich sites is seemingly responsible for this conductivity behavior. In conclusion, these earlier works used iodine to generate a mixed Cu(I)/Cu(II) valence state and if the structure exhibited adequate contacts (*i.e.* close enough), then the formation of a semiconducting material was found possible.

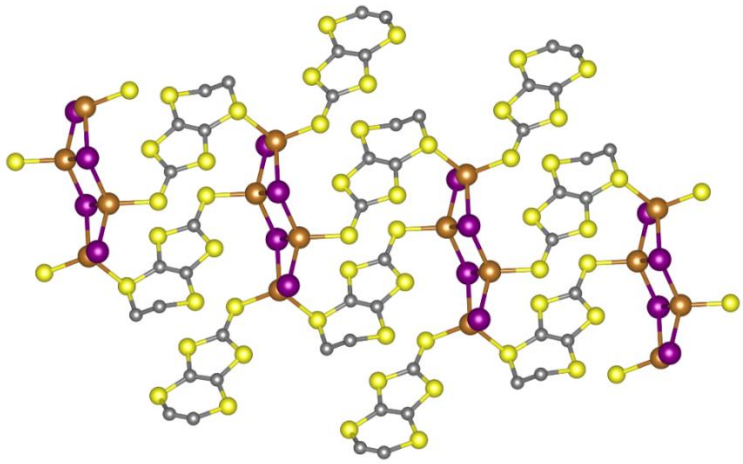

Figure 40. Structures of the 1D-$[Cu_4I_4(\mathbf{L35})_4]_n$ coordination polymer. Cu, orange; I, purple; S, yellow; C, grey. The image was reproduced using the cif files from the Cambridge Crystallographic Data Centre; CCDC numbers: 1217211.

More recently, Degaldo *et al*. reported the preparation of a series of thiobenzamide-containing CuX-coordination polymers (X = Br, I; thiobenzamide = **L8**) along with various properties including conductivity.[22] These luminescent coordination polymers are 1D and exhibit the formula $[CuI(\mathbf{L8})]_n$, $[Cu_3I_3(\mathbf{L8})_2]_n$, and $[CuBr(\mathbf{L8})]_n$ (**Figure 11**a, **Figure 13**a and **Figure 41**). The $[CuI(\mathbf{L8})]_n$ polymer may contain various solvent crystallization molecules in its lattice such as

THF, acetone, and methanol. Beside their sensing properties towards vapors using their changes in luminescence intensity, these materials also exhibit semi-conductivity properties (**Table 5**). Based upon an examination of the literature of related coordination polymers containing the $Cu_2I_2S_2$ repetitive unit and Cu-S-Cu-I chains (where the S-atom is not from a thioether or a thione), the authors concluded that these σ(25°C) values compares favorably with other semiconducting materials.[49–51]

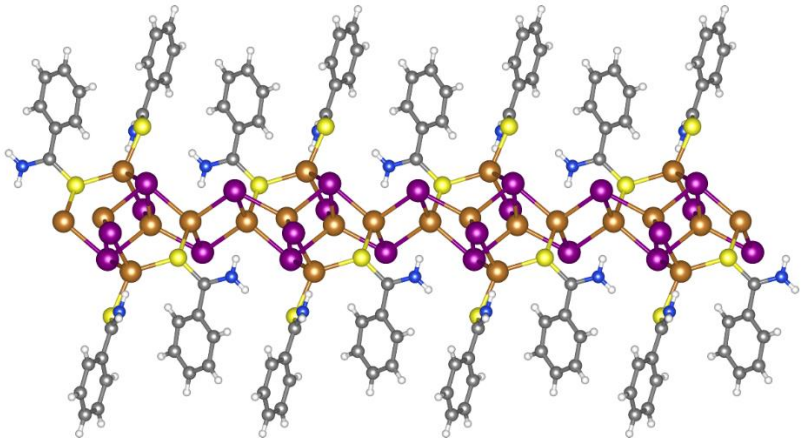

Figure 41. Structure of the 1D coordination polymer $[Cu_3I_3(\mathbf{L8})_2]_n$. Cu, orange; I, purple; Br, deep red; O, red; S, yellow; N, blue; C, grey; H, white. The image was reproduced using the cif files from the Cambridge Crystallographic Data Centre; CCDC numbers: 1835550.

Table 5. Conductivity data (σ(25°C), 2-point probe) and band gap values according to ref. [22].

	form	σ(25°C) (S cm^{-1})	Band gap
$[CuI(\mathbf{L8})]_n$	pellet	3.3 x 10^{-11}	1.38
$[CuI(\mathbf{L8})$•acetone$]_n$	crystal	1.3 x 10^{-8}	1.22
$[CuI(\mathbf{L8})$•MeOH$]_n$	crystal	1.15 x 10^{-9}	1.36
$[Cu_3I_3(\mathbf{L8})_2]_n$	crystal	1.7 x 10^{-10}	1.29
$[CuBr(\mathbf{L8})]_n$	pellet	3.6 x 10^{-8}	1.23
$[CuBr(\mathbf{L8})$•THF$]_n$	crystal	1.9 x 10^{-7}	1.21
$[CuBr(\mathbf{L8})$•acetone$]_n$	crystal	1.5 x 10^{-9}	1.27

This same research group also prepared a translucent film over several mm^2 surfaces of a maximum electric conductivity of 50 S cm^{-1} where the 2D layered polymer of the general formula $[Cu_2I_2(\mathbf{L36})]_n$ (**L36** = thioacetamide).[52] The synthesis was carried out at the water-air interface and the transparent film turned out to be mechanically robust and even stable with a thickness as thin as 4 nm. Using a 2:1 CuI/ligand ratio, the slow diffusion of an acetonitrile solution into diethyl

ether provided crystals a suitable quality for X-ray structure determination. However, the structure was rather disordered where the position of the Cu atoms was distributed over three lattice sites also shared with the iodine atoms (**Figure 42**a). The authors offered three possible structures (**Figure 42**a) and suggested their coexistence in the solid. The Cu-I (2.51-2.68 Å) and Cu-S (2.31-2.41 Å) coordination bond distances were found normal for this type of linkages. Interestingly, the single crystals exhibited a lower conductivity of 10^{-4} S cm^{-1}, but the more amorphous crystals showed conductivity reaching 10 S cm^{-1}. The interesting structural and electric conductivity features triggered a detailed investigation of these transparent films (**Figure 42**b-e). These films showed a memristive behavior at low frequencies, which is rare. The authors stressed that this combination of properties and the large availability of these two synthesis materials provides a great potential for applications in the area of transparent electronics. These two investigations (references [22] and [52]) demonstrate that even without the addition of a doping agent such as iodine, neutral copper halide-thioether and thione networks, as such, can exhibit electric conductivity.

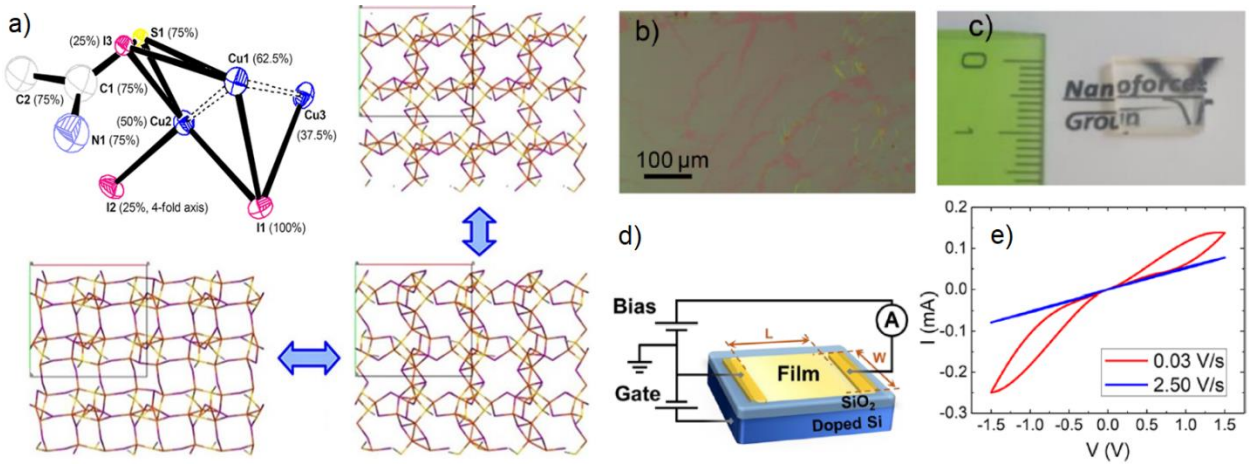

Figure 42. a) Structure of a fragment of the $[Cu_2I_2(\mathbf{L36})]_n$ coordination sheets stressing on the statistical disorder of the occupancy of the atoms, and three proposed 2D structures of this coordination polymer. b) Optical image of a representative sample deposited on a SiO_2 substrate. c) Photograph of a $[Cu_2I_2(\mathbf{L36})]_n$ film collected on a fused quartz with a ruler as a scale bar. d) Scheme of the set up to electrically characterize the films. e) Two representative I-V curves acquired on the same $[Cu_2I_2(\mathbf{L36})]_n$ film. At two bias sweeping speeds, where metallic and memristive behaviors are shown. Adapted with the permissions from *ACS Nano*, 2018, **12**, 10171–10177. [52] Copyright (2014) American Chemical Society.

The formation of conducting films or press pellets can also be achieved upon pyrolysis of coordination polymers, and the resulting electric properties become dependent on the nature of the initial coordination polymer. Recently, two coordination polymers of general formula 3D $[Cu_6I_6(\mathbf{L37})_3]_n$ and 2D $[Cu_4I_4(\mathbf{L38})_2]_n$ (**L37** = 1,4-bis(phenylthio)but-2-yne; **L38** = 1,4-bis(phenylthio)butane) were prepared using a 1:2 molar ratio (ligand/copper) in acetonitrile and then investigated.[53]

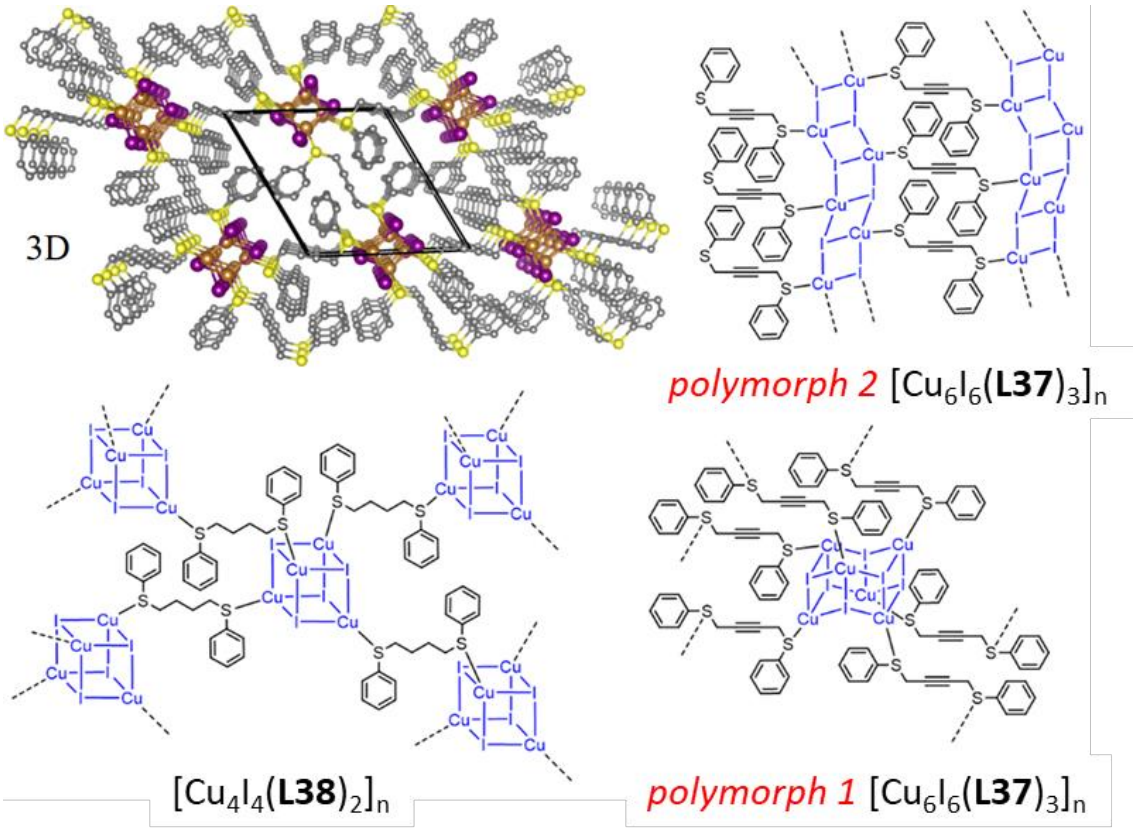

Figure 43. Top: Structure of the 3D coordination polymers of $[Cu_6I_6(\mathbf{L37})_3]_n$ (*polymorph 2*). Bottom: drawings of the structures of the 2D $[Cu_6I_6(\mathbf{L37})_3]_n$ (*polymorph 1*) and $[Cu_4I_4(\mathbf{L38})_2]_n$. Cu, orange; I, purple; S, yellow; C, grey. The image was reproduced using the cif files from the Cambridge Crystallographic Data Centre; CCDC numbers: 1855099.

The powder XRD pattern of the former coordination polymer did not match that of the single crystal obtained from the literature, where the SBU is a hexagonal prism (see the SBU colored in blue), *polymorph 1*.[54] New crystals were grown from slow evaporation of an acetonitrile solution over a week. The resulting structure is shown in **Figure 43** and consists of a polymorph with the

same elemental analysis. This new 3D network consists of a 1D staircase ladder $(CuI)_n$ SBU, which are interconnected by **L37** through the S-atoms with no interaction between the Cu atoms and the triple bonds, *polymorph 2*. These two coordination frameworks do not undergo phase changes with the temperature between 173 K and room temperature. These networks are rather found stable up to about 180°C, after which ligand loss is noticed in the TGA traces under air and nitrogen atmospheres. Upon thermal pyrolysis of *polymorph 2* and $[Cu_4I_4(\mathbf{L38})_2]_n$ at high temperature (*i.e.*, 400°C), composite materials are obtained. The resulting light greyish material originating from the $[Cu_4I_4(\mathbf{L38})_2]_n$ coordination polymer exhibited a 0.05 % in weight of carbon content and turned out rather brittle, so no conductivity measurements was carried out. Conversely, the composite of *polymorph 2* contained 10.2 % in weight of carbon and a significant amount of CuI in its cubic form (density = 3.58 g cm^{-3}). No carbon diffraction was observed indicating that this phase was amorphous. Pressed pellets of this composite (of *polymorph 2*) under 10 bar of pressure permitted the measurements of reflectance UV-vis spectra from which the band gap was evaluated at 2.93 eV. The electrical conductivity was measured along with its Seebeck coefficient. The conductivity was to decrease with the temperature between 75 and 250°C and the recorded conductivity started at 0.07 S cm^{-1} at 75°C and reached 0 S cm^{-1} at 250°C. The Seebeck coefficients range between 543 to 1308 mV K^{-1} in this temperature range.

In a similar fashion, this same research groups (Bai, Hor *et al.*) prepared another 2D polymer of formula $[Cu_4I_4(\mathbf{L39})_2]_n$ (**L39** = bis(2-(cyclohexylthio)ethyl)amine).[55] Its X-ray structure consists of a Z-shaped CuI-Cu_2I_2-CuI SBU binding all three donors of the ligand to form a 2D network and this coordination polymer is stable up to 260°C also under air or nitrogen atmosphere (**Figure 44**). The thermolysis at 400°C led to a robust composite (density = 4.32 g cm^{-3}) where again cubic CuI and amorphous carbon (4.25 %) are detected. The electrical conductivity measurements were carried out between 35 and 210°C and the recorded conductivity was noted to decrease from 0.6 to 0.0 S cm^{-1}. The Seebeck coefficients were reported to be 700-950 μV K^{-1} in the 25-204°C temperature range.

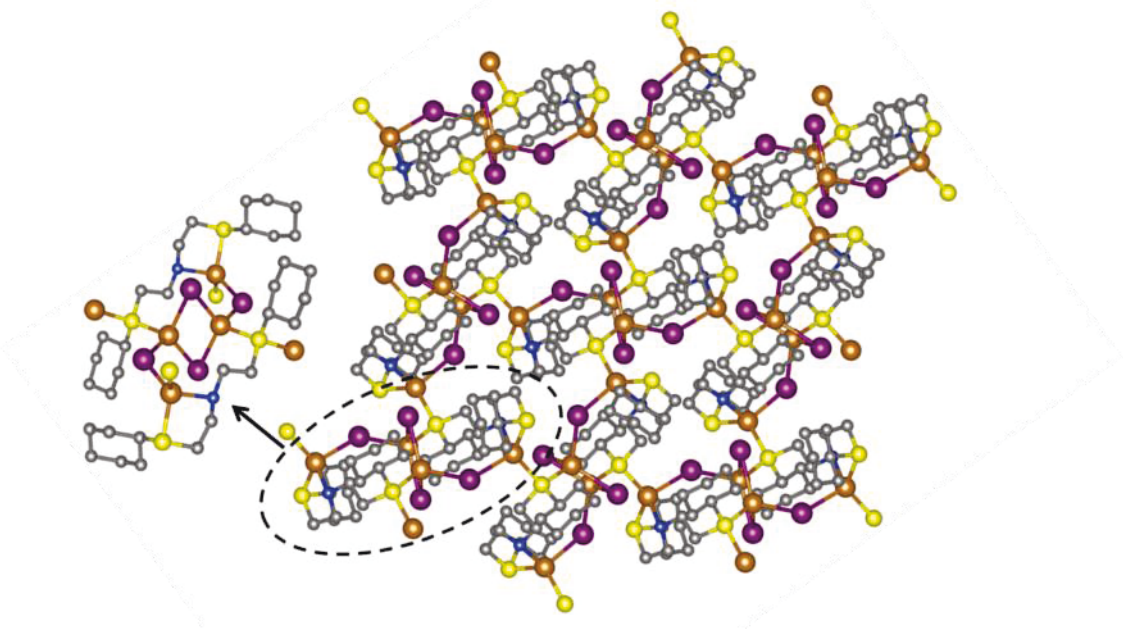

Figure 44. Left: structure of a unit of the coordination polymer $[Cu_4I_4(\mathbf{L39})_2]_n$. Right: 2D structure of the polymer $[Cu_4I_4(\mathbf{L39})_2]_n$. Cu, orange; I, purple; S, yellow; N, blue; C, grey. The images were reproduced using the cif files from the Cambridge Crystallographic Data Centre; CCDC numbers: 1586815.

Metal-containing ligands represent also an interesting variation of the chalcogene-donor ligands. In this category Okubo and collaborators investigated the neutral square planar S-metallo-ligands of the type $[Cu(\mathbf{SCS})_2]$ (**SCS** = piperidine-1-carbodithioate (**L40**) and hexamethylene dithiocarbamate (**L41**).[56] Using $[Cu(\mathbf{L40})_2]$ and $[Cu(\mathbf{L41})_2]$ in $CHCl_3$, they reacted these species with CuI in a solvent mixture proprionitrile/acetone. They obtained needle-shaped crystalline materials with isolated yields of 33.4 and 18.9 %, respectively. X-ray crystallography revealed the presence of a zigzag 1D coordination polymers $\{Cu_5I_5[Cu(\mathbf{SCS})_2](EtCN)\}_n \bullet CHCl_3$ (**Figure 45**). Both include a unique cluster as SBU formulated as $Cu_5I_5(EtCN)$ consisting of five tetracoordinated Cu(I) metals, five bridging I-anions, and a terminal EtCN. Using diffuse-reflection spectroscopy, and MgO soping, the electronic band gap (Eg), was evaluated to be 1.11 and 1.14 eV for **SCS** = **L40** and **L41**, respectively. The two polymers exhibit a semiconducting behavior and using impedance spectroscopy, the estimated conductivity was found to be 2.19 x 10^{-9} Scm^{-1} and 3.98 x 10^{-9} Scm^{-1} for **SCS** = **L40** and **L41**, respectively. The authors pointed out that the zigzag structures reveal a 1D-chain of alternating I-Cu(II)-I-Cu(II)-, with a Cu•••I

separation of 3.420(2) Å for **SCS** = **L40**, for instance. The thermal stability was tested using TGA, and the polymers started showing weight losses at 154 and 138°C for = **L40** and **L41**, respectively.

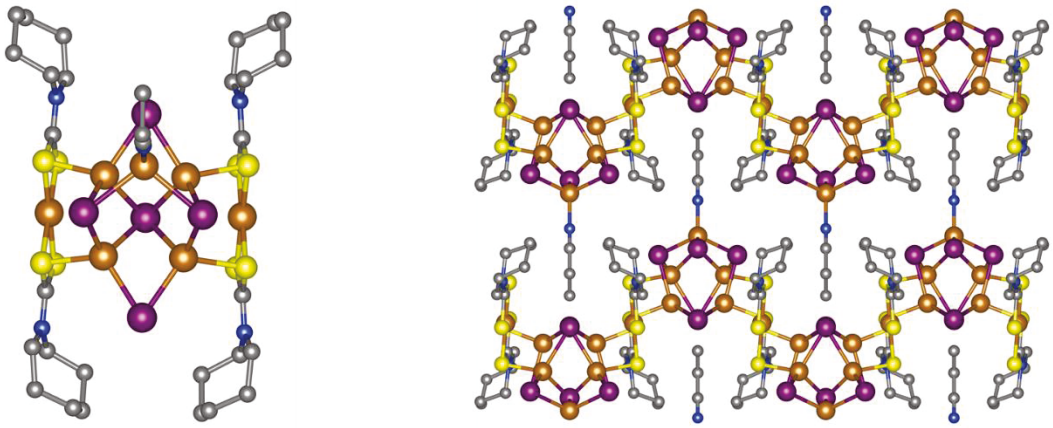

Figure 45. Left: Structure of a cluster $Cu_5I_5(EtCN)$ unit. Right: Structure of a segment of two layers of the 1D $\{Cu_5I_5[Cu(\mathbf{L40})_2](EtCN)\}_n$ polymer (the organic part of **L40** is not shown for clarity. Cu, orange; I, purple; S, yellow; N, blue; C, grey. The images were reproduced using the cif files from the Cambridge Crystallographic Data Centre; CCDC numbers: 931054 and 931053. Adapted with permission from Polyhedron 69 (2014) 103–109. Copyright (2014) Elsevier.

2.9. Dye sensitized solar cells

Dye sensitized solar cells (DSSCs) were also designed using these same neutral S-metallo-ligands.[57,58] These basic motifs (*i.e.* square planar $[M(\mathbf{SCS})_2]$, **SCS** = dithiocarbamate ligand) exhibits three mains features. First, these complexes are redox active when using an appropriate metal such as Ni(II) and Cu(II). Second, the S-atoms are prone to coordinate copper halide salts allowing for the buildup of coordination polymers Third, they are intensively colored due to the presence of a low-energy charge-transfer band (SCS → metal). This feature permits to absorb light far in the visible region extending well in the near-IR (as measured by diffuse-reflection absorption spectroscopy), thus acting like a dye. For examples in these two investigations, six 1D coordination polymers were prepared when copper halides (X = Br, I) were reacted with $[Cu(\mathbf{SCS})_2]$ where **SCS** = piperidine-1-carbodithioate (**L40**) and hexamethylene dithiocarbamate (**L41**),[57] and with $[Ni(\mathbf{SCS})_2]$ where **SCS** = **L41**,[58] in acetonitrile. In all cases, the structure of these polymers exhibits the same general formula $\{M'_2X_2[M(\mathbf{SCS})_2](CH_3CN)_2\}_n$ (M' = Cu or Ni; X = Br, I) and consists of an alternating chain of $[M(\mathbf{SCS})_2]$ and rhomboid Cu_2X_2 in a zigzag fashion (**Figure 46**).

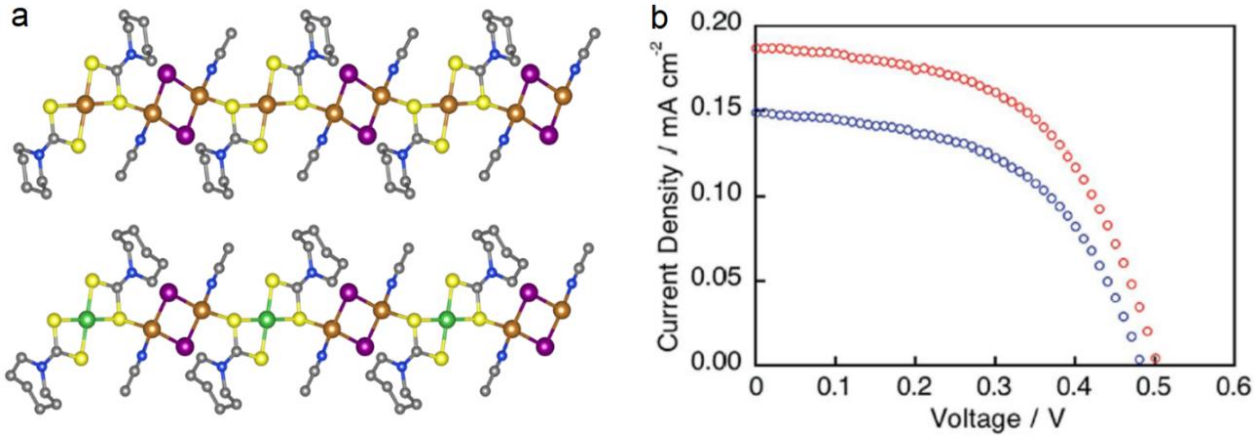

Figure 46. (a) X-ray structures of $\{Cu_2I_2[Cu(\mathbf{L40})_2](CH_3CN)_2\}_n$ and $\{Cu_2I_2[Ni(\mathbf{L40})_2](CH_3CN)_2\}_n$ as representative examples. Cu, orange; Ni, green; I, purple; S, yellow; N, blue; C, grey. Note that the polymers are all isostructural regardless X = Br or I, M(II) = Cu(II) or Ni(II). The images were reproduced using the cif files from the Cambridge Crystallographic Data Centre; CCDC numbers: 923679, 923680, 889235 and 889238. (b) Photocurrent density-voltage (*J/V*) curves of $\{Cu_2X_2[Cu(Pip\text{-}dtc)_2](CH_3CN)_2\}_n$ (X = Br (red), I (bleu). Adapted with permission from *Eur. J. Inorg. Chem.*, 2013, **2013**, 3384–3391. Copyright (2013) Wiley.

Table 6. DSSC's characteristics: short-circuit current densities (J_{SC}), open-circuit voltages (V_{OC}), fill factors (FF), and power conversion efficiencies (PCE).

coordination polymer	J_{SC} (mAcm^{-1})	V_{OC} (V)	FF	PCE (%)
$\{Cu_2Br_2[Cu(\mathbf{L40})_2](CH_3CN)_2\}_n$[57]	0.19	0.50	0.54	0.051
$\{Cu_2I_2[Cu(\mathbf{L40})_2](CH_3CN)_2\}_n$[57]	0.15	0.50	0.52	0.038
$\{Cu_2Br_2[Cu(\mathbf{L41})_2](CH_3CN)_2\}_n$[57]	0.41	0.50	0.53	0.11
$\{Cu_2I_2[Cu(\mathbf{L41})_2](CH_3CN)_2\}_n$[57]	0.39	0.50	0.56	0.11
$\{Cu_2Br_2[Cu(\mathbf{L41})_2](CH_3CN)_2\}_n$[58]	0.663	0.457	0.492	0.149
$\{Cu_2I_2[Cu(\mathbf{L41})_2](CH_3CN)_2\}_n$[58]	0.633	0.460	0.519	0.151
$\{Cu_2Br_2[Ni(\mathbf{L41})_2](CH_3CN)_2\}_n$[58]	0.171	0.519	0.387	0.034
$\{Cu_2I_2[Ni(\mathbf{L41})_2](CH_3CN)_2\}_n$[58]	0.163	0.527	0.489	0.041

The 1D-$\{Cu_2X_2[Cu(\mathbf{L40})_2](CH_3CN)_2\}_n$ polymers display strong antiferromagnetic interactions (J = -20.4 cm^{-1} (X = Br) and J = -18.8 cm^{-1} (X = I)) due to interactions between the unpaired electron of Cu(II) centers through the rhomboid Cu_2X_2 units. Both solids are semiconducting exhibiting activation energies of 0.78 (X = Br) and 0.62 eV (X = I) using impedance spectroscopy. By

comparison, the 1D-$\{Cu_2X_2[Cu(\mathbf{L41})_2](CH_3CN)_2\}_n$ polymers reveal similar properties (σ_{340K} = 1.07×10^{-7} S cm^{-1}, E_a = 0.56 eV, (X = Br); σ_{340K} = 2.46×10^{-7} S cm^{-1}, E_a = 0.48 eV (X = I)).[59] Conversely, the 1D-$\{Cu_2X_2[Ni(\mathbf{L41})_2](CH_3CN)_2\}_n$ polymers turned out insulators (σ_{300K} <10^{-12} S cm^{-1}). This latter comparison suggests that the Cu(II)•••Cu(I) interactions play a key role in the electrical conductivity. The 1D-$\{Cu_2X_2[M(\mathbf{SCS})_2](CH_3CN)_2\}_n$ polymers (M = Cu(II), Ni(II); SCS = **L40**, **L41**) polymers were compared in a DSSCs study. The polymers were mixed with TiO_2 paste by grinding in a mortar and then painted on an indium tin oxide (ITO) substrate. Under standard irradiation conditions of AM 1.5 (100 mW/cm^2), the performances were tested. The power conversion efficiencies (PCE) are as follow: $\{Cu_2X_2[Cu(\mathbf{L40})_2](CH_3CN)_2\}_n$, 0.051 (X = Br), 0.038 % (X = I);[57] $\{Cu_2X_2[Cu(\mathbf{L41})_2](CH_3CN)_2\}_n$, 0.11 (X = Br), 0.11 % (X = I), according to ref [57], and 0.149 (X = Br) and 0.151 % (X = I) according to ref.[58] ; $\{Cu_2X_2[Ni(\mathbf{L41})_2](CH_3CN)_2\}_n$, 0.034 (X = Br), 0.041 % (X = I).[58] The overall characteristics of the DSSCs are placed in **Table 6**. In overall, these PCEs appears rather modest, but the main conclusion is that the presence of Cu(II)-Cu(I) metals within the same network is reminiscent of the mixed valence species of the generally conducting materials, and consequently these materials appear prone for the design of photonic devices.

2.10. Crosslinking of organic polymers for multifunctional and smart materials

The crosslinking of organic polymers promotes the design of multifunctional and stimuli responsive materials, and the use of neutral CuX salts as crosslinking agents has been explored by Zhang and coworkers.[60,61] In a first investigation, a block copolymer poly(methyl methacrylate)-b-poly(methyl thioethyl acrylate-co-butylacrylate) (PMMA-b-P(MTEA-co-BA)), in which thioether pendent groups were introduced, was prepared and reacted with CuBr in acetonitrile leading to a reinforcement of the polymer (**Figure 47**).[60] The nature of the [CuBr] reticulation units inside the resulting material was not identified. However, past reviews provide a strong indication that, in the absence of steric limitation such as in these highly flexible organic polymers, the common $Cu_2Br_2S_4$ rhomboid SBU be the major component of these crosslinking units in these hybrid materials.[6-8] For example, the flexible $EtS(CH_2)_4SEt$ ligand forms an emissive 3D coordination polymer with CuBr where the $Cu_2Br_2S_4$ rhomboid motif is depicted.[62] Moreover, knowing that many coordination polymers containing this particular $Cu_2Br_2S_4$ rhomboid motif are often emissive,[63–66] it would have been useful to examine the luminescence spectra in an attempt

to corroborate this possibility. Nevertheless, the best or optimum material (based on the stress *versus* strain curves) was obtained when the 6.6% (in weight determined by Inductively Coupled Plasma Atomic Emission Spectroscopy (ICP-AES)) of CuBr content was incorporated in the polymer samples. The resulting materials was stable up to 300°C from TGA measurements. The crosslinking behavior was confirmed by DSC upon comparing the traces of the pure dibloc polymer to the hybrid material. Indeed, two phase transitions occurred for the pristine organic copolymer (at -25 and 93°C witnessing a phase separation and a Tg), but only one Tg was observed for the hybrid materials. Increasing the CuBr content, for example 10.5 % rendered the material brittle. The hybrid materials with variable CuBr contents exhibit high tensile strength (up to σ_b = 7.5 MPa) and breaking strain (ε_b = 500 %) but this high crosslinking density is made to the detriment of the ductility. Because these light-colored film materials (about 0.1 mm thick) change colour rapidly from yellow to brown upon exposing them to HCl vapor (10 sec) and rapidly in contact with a 3% hydrogen peroxide solution (1 min), the authors stressed on the possibility of a new type of sensors. These new materials also show self-healing ability, which can occur within 24 h by keeping both ends in contact at room temperature (**Figure 49**). Although the process has not been demonstrated formally, one can anticipated that upon cut, the Cu-S bond breaks leaving behind unsaturated copper(I) atoms and thioether ligands free. When the two pieces are put back together, then recombination occurs. After that, the materials were stretchable again with approximately with the same stress versus strain properties.

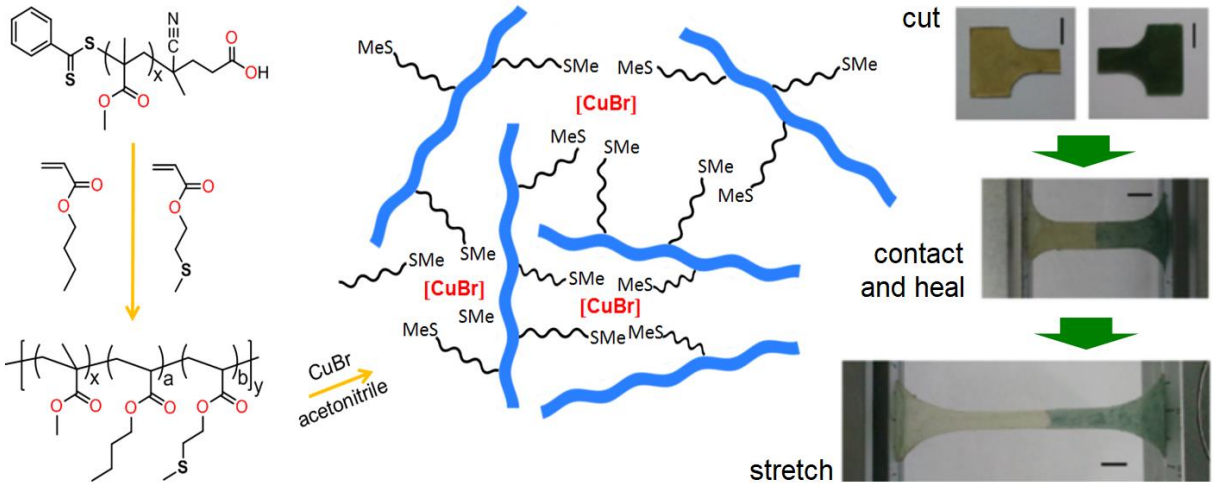

Figure 47. Left: Synthesis of the PMMA-b-P(MTEA-co-BA polymer and its coordination with CuBr. Right: Representative photos of the PMMA-b-P(MTEA-co-BA dog-bone sample

containing 6.6 % CuBr for self-healing test. Scale bar = 5 mm. Adapted with the permission from *Polym. Chem.*, 2017, **8**, 6527–6533. Copyright (2017) Royal Chemical Society.

Subsequently, this approach was also applied to other organic polymers containing the alternating $(A\text{-}B)_n$ structure in which regularly spaced thioether functions were introduced in the main chain.[61] Upon reaction with CuI (**Figure 48**), two emissive hybrid materials are generated labelled as PETD-CuI (λ_{emi} = 580 nm) and PAND-CuI (λ_{emi} = 570 nm). The authors correctly pointed out that the SBU motifs formed upon coordination of CuI with thioethers are diverse with excellent size and shape variability thus capable of adapting to various bite distances and angles. Consequently, the authors prudently did not speculate on the emissive motifs inside the hybrid materials. However, past investigations demonstrate clearly that the globular CuI-SBU motifs are far more emissive than the flat ones,[6-8] and that without any geometric constraint the most probable motifs are the common closed cubane $Cu_4I_4S_4$ and rhomboid $Cu_2I_2S_4$ motifs, depending on the Cu-to-S ratio.[6-8] Indeed, the reported spectra exhibit precisely the usual λ range and FWHM (Full width at half maximum) that the emission bands for $Cu_4I_4S_4$ cubane normally have. However, the closed cubane $Cu_4I_4S_4$ motif is generated when the M/L ratio is 1:1 which is more concentrated than 1:2 which often result in the $Cu_2I_2S_4$-rhomboid. Because the $Cu_2I_2S_4$-rhomboids are generally weak emitters (but not exclusively) and that the synthesis was performed under small M/L ratio, the presence of rhomboid bridges cannot be ruled out in this case. These hybrid materials are found more stable based on TGA measurements with a temperature of degradation reaching 220°C. This temperature is higher than that reported for the 0D-molecular Cu(I)-thioether clusters in the literature (100-160°C). The PETD polymer exhibits a Tg at -67.8°C and at 22.5°C after coordination. Concurrently, the PAND polymer exhibited Tg's at 73.4°C and 114°C before and after complexation with CuI. The powder XRD patterns of the hybrid materials are ill-defined indicating that these polymeric species are amorphous. The shape processing of these materials is easily achievable at high temperature. They also exhibit excellent stress-strain properties. For instance, the PAND-CuI with 10% CuI content exhibits strain at break (ε_b) at 80% and a fracture stress (σ_b) at 175 kPa. These two hybrid materials exhibited self-healing after cutting the materials and then left in contact for a period of 72 h.

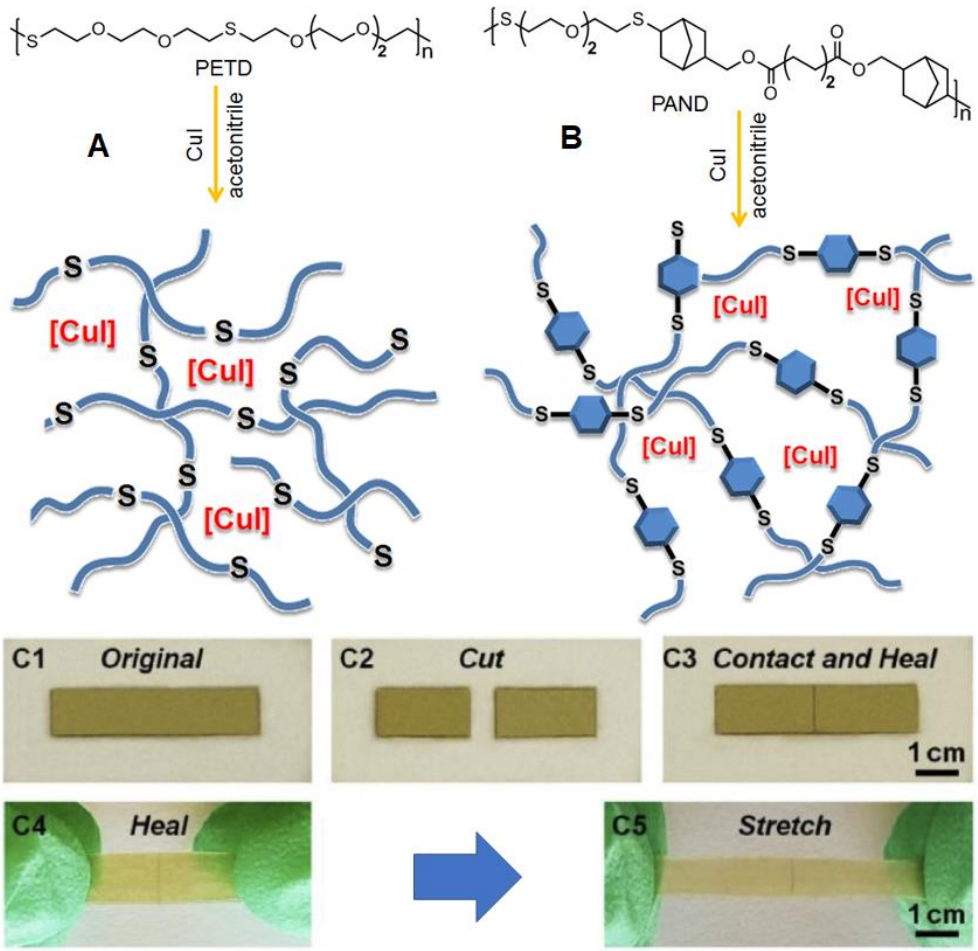

Figure 48. Reaction pathway used to prepare the emissive CuI-containing hybrid materials. The PETD-CuI (A) and PAND-CuI (B) mass ratio varied from 50% to 5%. (C) Representative photos of a PETD-CuI sample for a self-healing test. The self-healing occurred over a period of 72 hrs. Adapted with the permission from *Polymer.*, 2019, **179**, 121616/1-121616/7. Copyright (2019) Elsevier.

A supramolecular assembling strategy has also been proposed for the more structurally rigid poly(3-hexylthiophene), P3HT, with the $CuCl_2$ salt in ethylene glycol (**Figure 49**).[67] In this assembly, π–π stacking is promoted in a hydrophilic environment aided by the ionic nature of the $CuCl_2$, which was probably bonded to the S-atom of the thiophene residue. The powder XRD patterns indicated that the resulting materials were amorphous, despite the presence of crystal under the optical microscope (**Figure 49**a,b). Although the oxidation state of Cu(II) does not match the scope of this review, the provided experimental data in this investigation strongly suggest that the dication has been reduced to Cu(I). The drastic evidence comes from the fluorescence

quenching measurements where upon increasing the amount of $CuCl_2$, the resulting fluorescence gradually shifts to the blue side of the spectrum indicating that the π-conjugation of the polythiophene chain was cut off. This chemical process witnesses the presence of an oxidation of the P3HT. It is well known that $CuCl_2$ quenches fluorescence of organic molecules by photoinduced electron transfer,[68,69] and conjugated polymers by both energy and electron transfers.[70] For P3HT, it was demonstrated in the literature that the presence of Cu^{2+} does indeed break the π-conjugation length of the polymer chain and consequently results in a blue-shift in the absorption band, a process assigned as an oxidative doping.[71] In the presence of thioether residues, this redox process, Cu(II) + 1 e^- → Cu(I), has been observed several times where the thioether is also used as a sacrificial ligand.[17,72–75] In the most two recent works, the resulting coordination polymers exhibited a full conversion of the Cu(II) into Cu(I). Moreover, the supramolecular assembly proposed by the authors was not investigated by EPR spectroscopy with the aim to confirm whether a mixed valence state exists. Moreover, a library search on polythiophenes coordinated to copper(II) ion (other than this work) turned out futile. Concurrently, several investigations showed that the soft Lewis acid copper(I) is capable of forming coordination polymers upon the coordination to thiophene derivatives.[76] All in all, this supramolecular concept is interesting, but research deserves to be revisited to secure the nature of the Cu atoms.

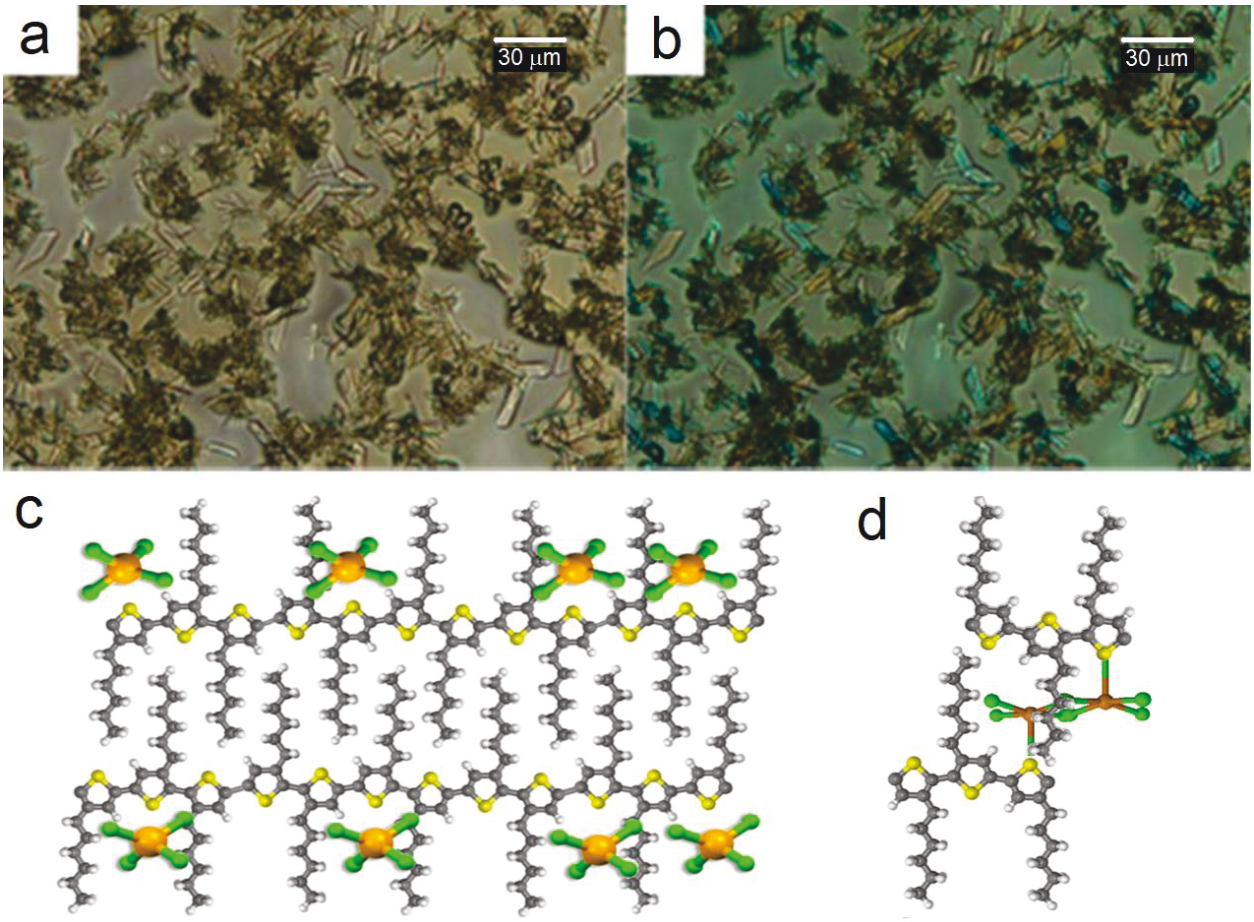

Figure 49. (a) Optical microscope image of a mixture of P3HT (1% wt%) and $CuCl_2$ (4000 ppm) in ethylene glycol (EG). (b) Texture polarized light of this same sample. Note that X-ray powder XRD confirms the absence of $CuCl_2$ crystals (c) Proposed primary supramolecular structure of P3HT in solution in the presence of $CuCl_2$ and EG. The complexes are $CuCl_4^{2-}$ anions (suggesting that the counter cations must be $[Cu(H_2O)_6]^{2+}$ or $[Cu(EG)_3]^{2+}$. (d) Fragment of the proposed coordination assembly between P3HT and $CuCl_2$, which form a 1D-poly($CuCl_2$) adopting a square pyramidal geometry about the Cu(II) atom. However, there is an obvious mismatch in the Cu•••Cu and S•••S distances, and obvious steric hindrance with the hexyl chain. Adapted with the permission *RSC Adv.*, 2015, **5**, 87723–87729. Copyright (2019) Royal Chemical Society.

2.11. Cytotoxicity and antibacterial properties

Thione complexes of the CuX salts exhibit cytotoxic and antibacterial properties as well and several recent reports on the subject have recently appeared. For example, the bidentate 1,1'-(1,2-ethanediyl)bis(3-methylimidazole-2-thione) ligand **(L42)** reacts, through a layer diffusion process,

with two equivalents of CuBr to form an air stable 2D coordination polymer formulated as $[Cu_2Br_2(\mathbf{L42})]_n$ (**Figure 50**).[77] This synthesis is accompanied by a parallel redox reaction forming a byproduct salt identified by X-ray structure determination as $[(C_{10}H_{14}N_4S)CuBr_3]$. Evidence for thione-Cu coordination was obtained by IR, fluorescence spectroscopy, and X-ray diffraction data. Indeed, the ν(C=S) value shifts from 516 to 508 cm^{-1} upon the ligand coordination. Similarly, the fluorescence maximum (λ_{max}) also shift from 320 to 367 nm (λ_{exc} = 280 nm). This fluorescence band was assigned to arise from an intraligand ππ* excited state. The structure of the coordination polymer consists of honeycomb layers built upon 12-membered macrometallocycle and centro-symmetric $Cu_2Br_2S_4$ rhomboids as SBUs interconnected by the bridging 1,1'-(1,2-ethanediyl) bis(3-methyl-imidazole-2-thione) ligand **L42** in a zigzag fashion through Cu-S coordination bonds.

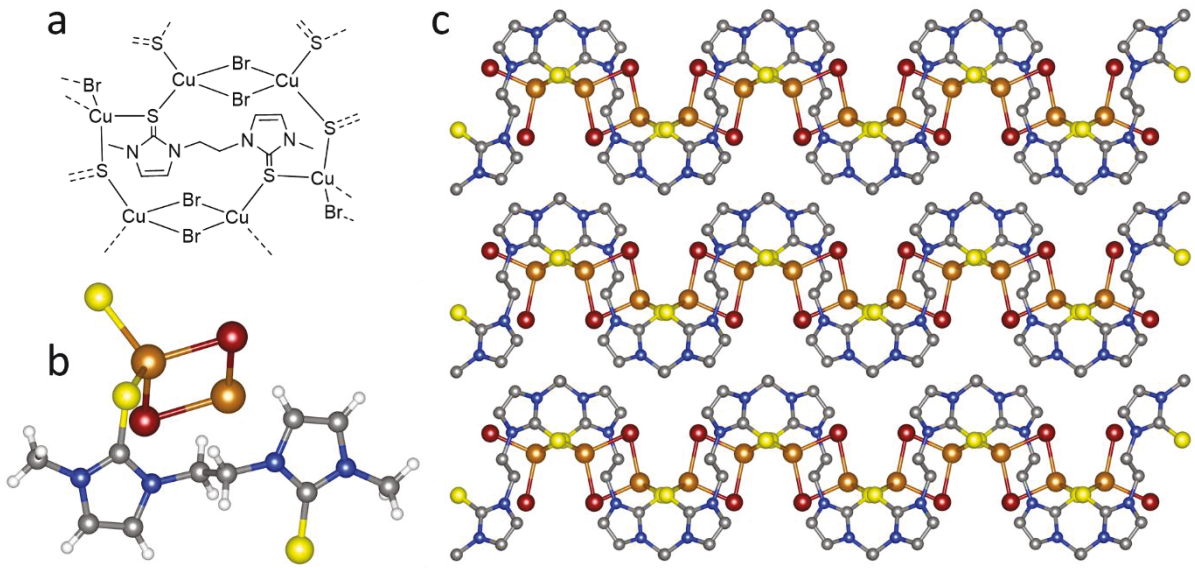

Figure 50. (a) Drawing of the molecular structure of 1,1'-(1,2-ethanediyl)bis(3-methyl-imidazole-2-thione) (**L42**) and its surrounding within the 2D coordination polymer $[Cu_2Br_2(\mathbf{L42})]_n$. (b) Representation of a fragment of the coordination polymer. (c) View of a slice of 3 layers of the 2D structure. Cu, orange; Br, deep red; S, yellow; N, blue; C, grey; H, white. The images were reproduced using the cif files from the Cambridge Crystallographic Data Centre; CCDC numbers: 1909121.

In this work, model pollutants were investigated (Congo Red, Aniline Blue, Malachite Green and Victoria Blue) for their adsorption onto or inside the 2D $[Cu_2Br_2(\mathbf{L42})]_n$ coordination layers.

Detailed analyses of their corresponding isotherms (*i.e.* Freundlich, Langmuir and Temkin) were performed and proposed adsorption mechanisms were provided. Taking advantage of the well-defined 2D structure of this coordination polymer, well organized CuO nanospheres could be prepared using the ultrasonic and calcination method. This coordination polymer is stable up to 120°C based on TGA analysis. Between 120 and 250°C, the weight loss is attributed to the ligand elimination. In the 410-700°C temperature range, bromide atoms escape, and subsequently the formation of CuO nanospheres occurs (at T > 700°C). The resulting agglomerated nanospheres were of 2.05 to 10.30 nm in diameters (based TEM (Transmission Electron Microscop) and SEM (Scanning Electron Microscopy) measurements). The identity of these nanospheres was confirmed by powder XRD and EDX (Energy-dispersive X-ray spectroscopy) spectra. This CuO material was tested for the photocatalytic degradation of the organic dye Rhodamine B adsorbed inside the nanosphere in the presence of a very small amount of H_2O_2 (30 % weight). The photoreaction ($400 < \lambda_{exc} < 700$ nm), monitored by UV-vis spectroscopy. The photoinduced antibacterial activity was also assessed by monitoring the half minimal inhibitory concentration and inhibitory concentration based on MTT (3-(4,5-dimethylthiazol-2-yl)-2,5-diphenyltetrazolium bromide) colorimetric assay on two Gram-negative bacteria of *Escherichia coli* and *Pseudomonas aeruginosa* and two *Gram-positive* bacteria of *Staphylococcus aureus* and *Bacillus subtilis*. The resulting antimicrobial activity turned out good and medical applications may be possible. It is worth noting that the coordination polymer precursor $[Cu_2Br_2(\mathbf{L42})]_n$ has no activity towards the investigated bacteria essentially meaning that their 2D structures and efficient absorptivity properties are predisposition for the preparation of good CuO materials for photocatalytic applications.

New CuX complexes (X = Cl, Br, I) of *N*-substituted imidazolidine-2-thiones were recently prepared and investigated for their antimicrobial activity.[78] Among these species, bi-, tetra-, and hexanuclear complexes and 1D coordination polymers ($[Cu_6Cl_6(\mu\text{-S-}\mathbf{L44})_6]$, $[Cu_2Br_2(\mu\text{-S-}\mathbf{L43})_2(\kappa^1\text{-S-}\mathbf{L43})_2]$, $[Cu_4I_2(\mu\text{-I})_2(\mu\text{-S-}\mathbf{L43})_4(\kappa^1\text{-S-}\mathbf{L43})_2]$ and $[Cu(\mu\text{-I})_2Cu(\mu\text{-S-}\mathbf{L43})_2]_n$) were prepared and characterized by X-ray diffraction studies (**Figure 51**). These materials were probed for their antimicrobial properties against the Gram positive bacteria *Staphylococcus aureus,* MTCC740, and methicillin resistant *Staphylococcus aureus*, MRSA, and Gram negative bacteria, *Klebsiella pneumoniae*, MTCC109), *Salmonella typhimurium*, MTCC741) and *Candida albicans*, MTCC227). The $[Cu_6Cl_6(\mu\text{-S-}\mathbf{L44})_6]$, $[Cu_2Br_2(\mu\text{-S-}\mathbf{L43})_2(\kappa^1\text{-S-}\mathbf{L43})_2]$, $[Cu_4I_2(\mu\text{-I})_2(\mu\text{-S-}\mathbf{L43})_4(\kappa^1\text{-}$

S-**L43**)$_2$] complexes exhibit zones of inhibition and the minimum inhibitory concentration (**Table 7**).

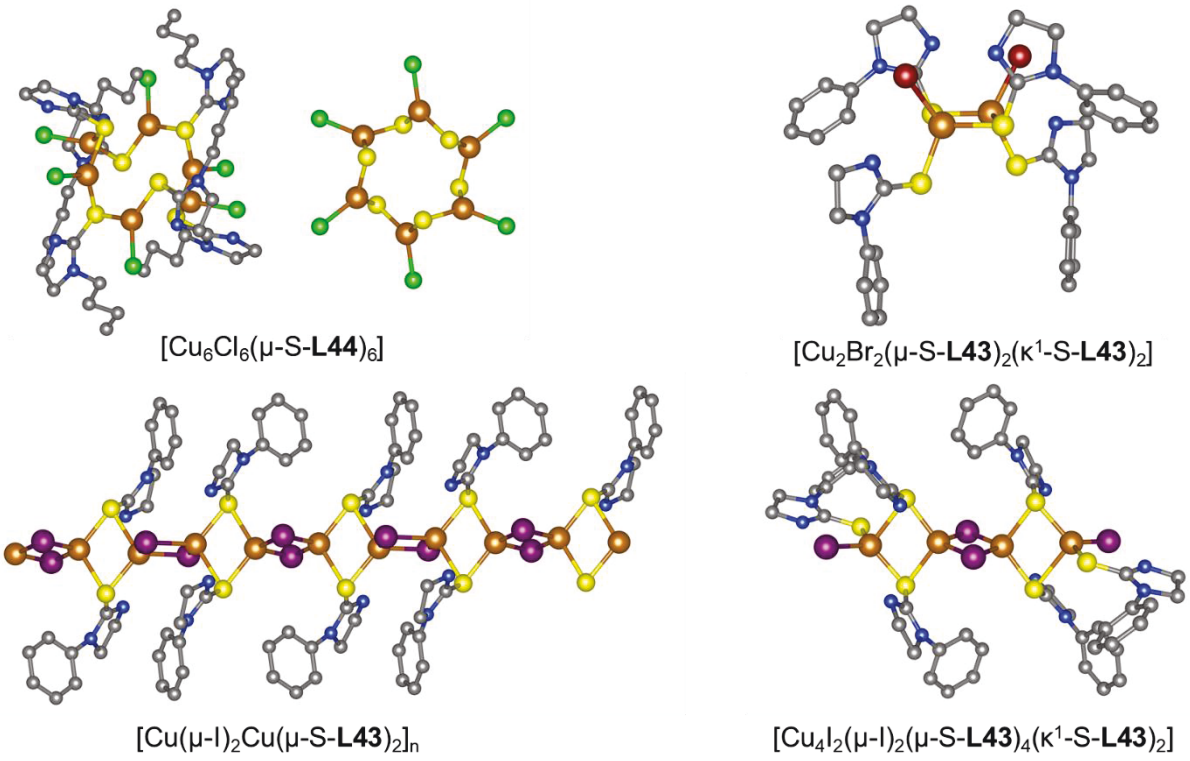

Figure 51. Structures of [Cu_6Cl_6(μ-S-**L44**)$_6$] with emphasis on the 12-member S-Cu core ring, [Cu_2Br_2(μ-S-**L43**)$_2$(κ^1-S-**L43**)$_2$], [Cu_4I_2(μ-I)$_2$(μ-S-**L43**)$_4$(κ^1-S-**L43**)$_2$] and [Cu(μ-I)$_2$Cu(μ-S-**L43**)$_2$]$_n$. Cu, orange; I, purple; Cl, green; Br, deep red; S, yellow; N, blue; C, grey. The images were reproduced using the cif files from the Cambridge Crystallographic Data Centre; CCDC numbers: 1507434, 1506832, 1507427 and 1506830.

Table 7. Zones of inhibition and minimum inhibitory concentration (in mg L^{-1}) for [Cu_6Cl_6(**L44**)$_6$], [Cu_2Br_2(**L43**)$_2$(**L43**)$_2$], and [Cu_4I_2(μ-I)$_2$(**L43**)$_4$(**L43**)$_2$] in DMSO.

complex	Methicillin Resistant *Staphylococcus aureus*	*Staphylococcus aureus*	*Klebsiella pneumoniae*	*Candida albicans*
[Cu_4I_2(μ-I)$_2$(μ-S-**L43**)$_4$(κ^1-S-**L43**)$_2$]	—	14 (1250)	20 (50)	15 (1000)
[Cu_2Br_2(μ-S-**L43**)$_2$(κ^1-S-**L43**)$_2$]	—	16 (50)	23 (50)	16 (750)
[Cu_6Cl_6(μ-S-**L44**)$_6$]	13 (1250)	19 (50)	26 (7)	18 (750)

Similarly, regardless of the ligand-metal ratio, the ligand *N*-methylbenzothiazole-2-thione (**L45**) reacts with the CuX salts (X = Cl, Br, I) to form the corresponding emissive [CuX(**L45**)$_2$]$_2$ complexes.[79] The structure of complex [CuCl(**L45**)$_2$]$_2$ was determined by X-ray structure (**Figure 52**). The antibacterial activity of these complexes as well as their ability to interact with native calf thymus DNA (CT-DNA) *in vitro* were also investigated (**Table 8**). For *E. Coli* and *B. subtilis,* the half-minimal inhibitory concentration (IC_{50}) follows the trend X = I > Br > Cl, and the IC_{50} value ranges from 22 to 29 mg/mL and from 23 to 27 mg/mL, respectively. For *S. aureus*, the trend changed to X = Br > Cl > I and IC_{50} ranged from 32 to 53 mg/mL. For *X. campestris*, the trend was X = Cl > l > Br and the IC_{50} data varied 31 to 39 mg/mL. Concurrently, the trend was X = Cl > Br > I and the IC_{50} values going from 57 to 62 mg/mL for *B. cereus*. In conclusion, considering the uncertainties, the binuclear species exhibit similar, and yet, significant activities against all bacteria examined, which also compare favorably to that of standard antibiotic ampicillin. Finally, all three complexes exhibit IC_{100}'s, minimum inhibitory concentrations, of 50 to 100 $\mu g \cdot mL^{-1}$. The integrity of the CT-ds DNA was investigated using gel electrophoresis (stained with ethidium bromide). Indeed, the DNA electrophoretic mobilities showed that the [CuX(**L45**)$_2$]$_2$ complexes bind to CT-ds DNA and result in the formation of high molecular weight species which ultimately leads to the degradation of DNA.

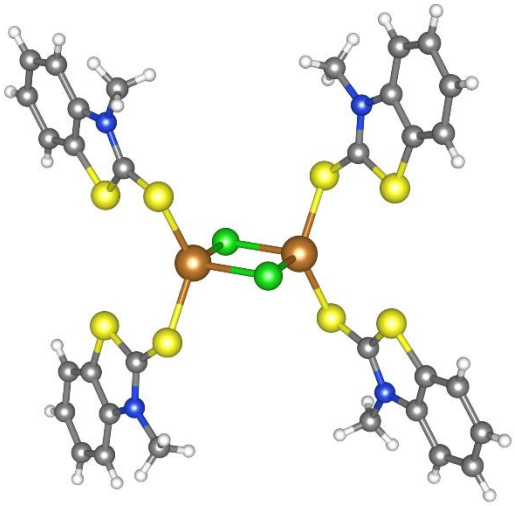

Figure 52. X-ray structure of 0D-[CuCl(**L45**)$_2$]$_2$. Cu, orange; Cl, green, S, yellow; N, blue; C, grey; H, white. The image was reproduced using the cif files from the Cambridge Crystallographic Data Centre; CCDC number: 906821.

Table 8. Antimicrobial activities of $[CuX(\mathbf{L45})_2]_2$ complexes evaluated by the half-minimal inhibitory concentration (IC_{50}) and the inhibitory concentration (IC_{100}) ($\mu g \cdot mL^{-1}$; values in parentheses are in μM).

Complex	*E. coli*		*X.campestri*		*S.aureus*		*B.cereus*		*B.subtilis*	
	IC_{50} (μg/mL)	IC_{100} (μg/mL)	IC_{50} (μg/mL)	IC_{100} (μg/mL)	IC_{50} (μg/mL)	IC_{100} (μg/mL)	IC_{50} (μg/mL)	IC_{100} (μg/mL)	IC_{50} (μg/mL)	IC_{100} (μg/mL)
$Cu_2Cl_2\mathbf{L45}_4$	29 (31.4)	100 (108.3)	31 (33.6)	50 (54.2)	32 (34.7)	100 (108.3)	57 (61.7)	100 (108.3)	27 (29.2)	50 (54.2)
$Cu_2Br_2\mathbf{L45}_4$	28 (27.7)	100 (98.8)	50 (49.4)	100 (98.8)	27 (26.7)	100 (98.8)	60 (59.3)	100 (98.8)	26 (25.7)	50 (49.4)
$Cu_2I_2\mathbf{L45}_4$	22 (19.9)	100 (90.4)	39 (35.3)	100 (90.4)	53 (47.9)	100 (90.4)	62 (56.1)	100 (90.4)	23 (20.8)	50 (29.8)

For comparison purposes with the thione-containing complexes discussed above, mercaptant-containing species have also been investigated.[80] One of the synthesized complexes was $[Cu(\mathbf{L46})I]_2$ (**L46** = 2-mercaptonicotinic acid), which was characterized by IR, ^1H and ^{13}C NMR spectroscopy, and elemental analysis. Its structure was addressed by DFT computations ($COSMO_{DMSO}$/B3LYP-D3/def2-TZVP) and consisted of a rhomboid Cu_2I_2 central core flanked by two 2-mercaptonicotinic acid ligand, through direct Cu(I)-S(thiolate) bonds. Its antimicrobial activity based on the IC_{50} measurements are as follow: 1) against gram-negative bacteria, *Escherichia coli*, 410 $\mu g \cdot mL^{-1}$, and *Pseudomonas aeruginosa*, 500 $\mu g \cdot mL^{-1}$, 2) against molds, *Aspergillus niger*, 510 $\mu g \cdot mL^{-1}$, *Penicillium citrinum*, >1000 $\mu g \cdot mL^{-1}$, and 3) against yeasts, *Candida albicans*, >1000 $\mu g \cdot mL^{-1}$, and *Saccharomyces cerevisiae*, >1000 $\mu g \cdot mL^{-1}$. The comparison of the *Escherichia coli* data (410 $\mu g \cdot mL^{-1}$) with that from the $[CuI(\mathbf{L46})_2]_2$ complex (22 mg/mL; X = Cl, Br, I) strongly suggest that the thione-containing materials exhibit superior performance (both exhibit a Cu_2I_2 rhomboid structure).

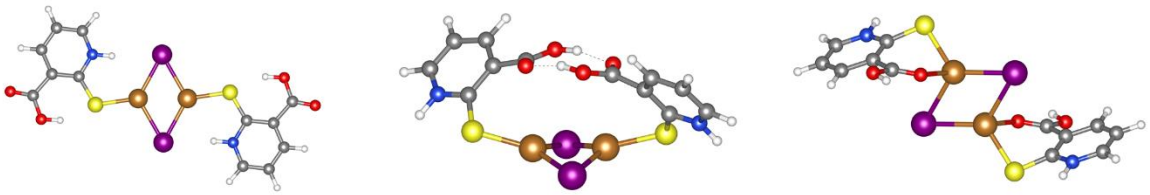

Figure 53. Proposed structures for $[Cu(\mathbf{L46})I]_2$ based on DFT computations ($COSMO_{DMSO}$/B3LYP-D3/def2-TZVP). Cu, orange; I, purple, S, yellow; N, blue; C, grey; H, white. The images were reproduced using the cartesian coordinates provided in supplementary data of ref 80.

3. The CuCN- and CuSCN-containing thioether and thione materials

The cyanide and thiocyanide are considered pseudo-halides and are incorporated into this review for comparison purposes. The first observation is that there are only several examples of studies that fall into the category of $Cu_xX_xE_y$ species (E = S, Se, Te) as defined in the Introduction, where X is a pseudo-halide. Excluding the presence of emission, the second observation is that functional materials have also been reported (see below), but the number of examples is proportionally scarce.

Hunter and collaborators reported what seems the only example where a coordination polymer is held together by Cu-S bonds without the contribution of the (μ2-C≡C)-Cu bond.[81] Indeed, an anthracenyl bearing four thioether groups, 9,10-bis{[3,4-bis(methylthio)phenyl]ethynyl}anthracene **L47**, forms a 2D coordination polymer of formula $[(CuCN)_2\mathbf{L47}]_n$ with CuCN where the CuCN unit forms the typical zigzag chain (**Figure 54**). The zigzag chains are interlinked by **L47** through Cu-S bonds. This polymer is emissive with a maximum near 614 nm.

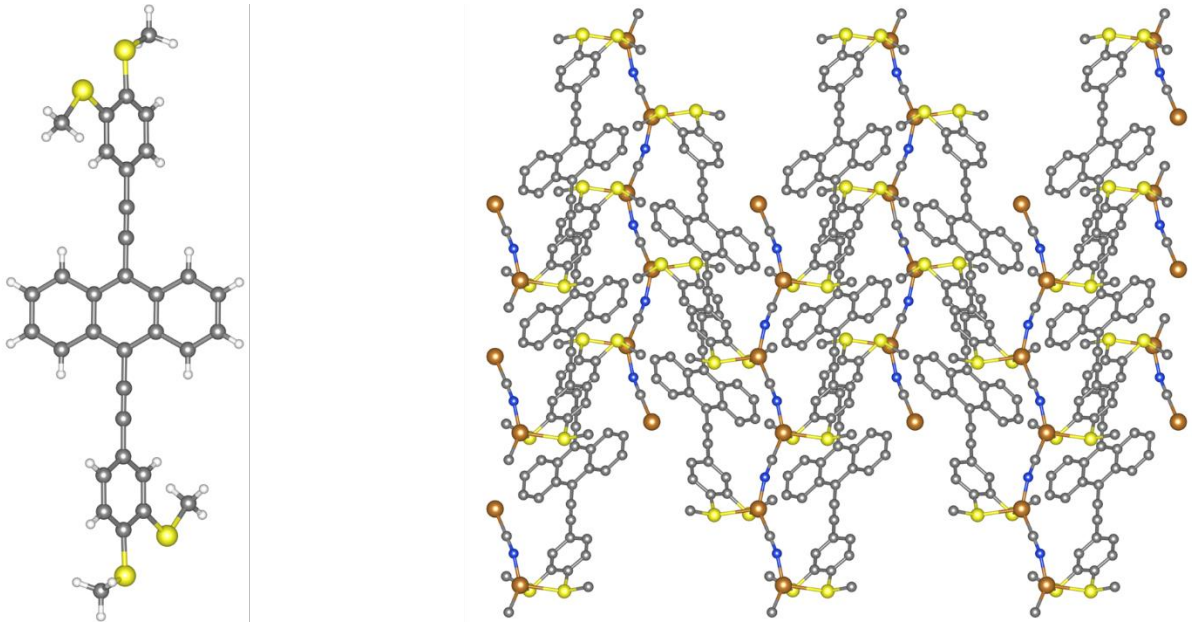

Figure 54. Left: Structure of ligand **L47**. Right: X-ray structure of the $[(CuCN)_2\mathbf{L47}]_n$ coordination polymers. Cu, orange; S, yellow; N, blue; C, grey; H, white. The images were reproduced using the cif files from the Cambridge Crystallographic Data Centre; CCDC numbers: 696009-696010.

Concerning the electron rich thione as ligands, an earlier work reported the preparation of a 2D coordination polymer built upon 1-methylimidazoline-2-thione (**L48**) and CuCN of formula $[CuCN(\mathbf{L48})]_n$.[82] The CuCN unit also builds the commonly encountered $(CuCN)_n$ zigzag chain flanked by two **L48** ligands coordinated through Cu-S bonds forming a cyclic Cu_2S_2 core, and hence completing a large honeycomb-like framework (**Figure 55**). This study turned out to be mainly crystallographic.

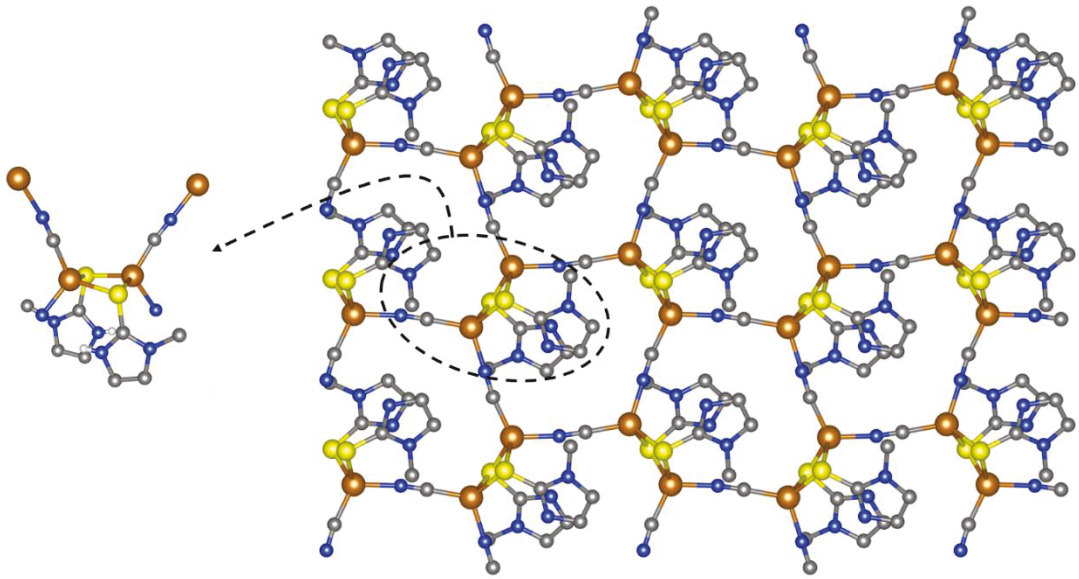

Figure 55. Left: X-ray structure of a fragment of the $[CuCN(\mathbf{L48})]_n$ coordination polymer. Right: 2D representation of this polymer. Cu, orange; S, yellow; N, blue; C, grey; H, white. The images were reproduced using the cif files from the Cambridge Crystallographic Data Centre; CCDC number: 1181993.

Several mixed Cu(I)/Au(I) coordination polymers built the pseudohalide CN^- and dimethylsulfide (**L1**) and diethylsulfide (**L2**) also recently described and characterized.[83] These materials were formulated as $[Cu_xAu_{(1-x)}CN(\mathbf{L})]_n$ (x = 0.67, 0.50; **L** = **L1**, **L2**). The 3D $[Cu_{0.5}Au_{0.5}CN(\mathbf{L1})]_n$ coordination polymers consists of parallel $(CuCN)_n$ zigzag chains placed in parallel layers. Then, the metals are bridged by dimethylsulfides forming a 3D network resembling at a honeycomb network (**Figure 56**). The $[Cu_{0.67}Au_{0.33}CN(\mathbf{L})]_n$ versions ($\mathbf{L_i}$ = **L1**, **L2**) are found isostructural. Both are emissive (λ_{emi} = 420 nm for **L2**, and λ_{emi} = 460 nm for **L1**) at room temperature. When the sulfide ligands are absent from the 3D structure, the resulting $[Cu_xAu_{(1-x)}CN]_n$ coordination

polymer is found non-emissive but is found vapoluminescent upon exposing the materials to dimethylsulfide and diethylsulfide vapours.

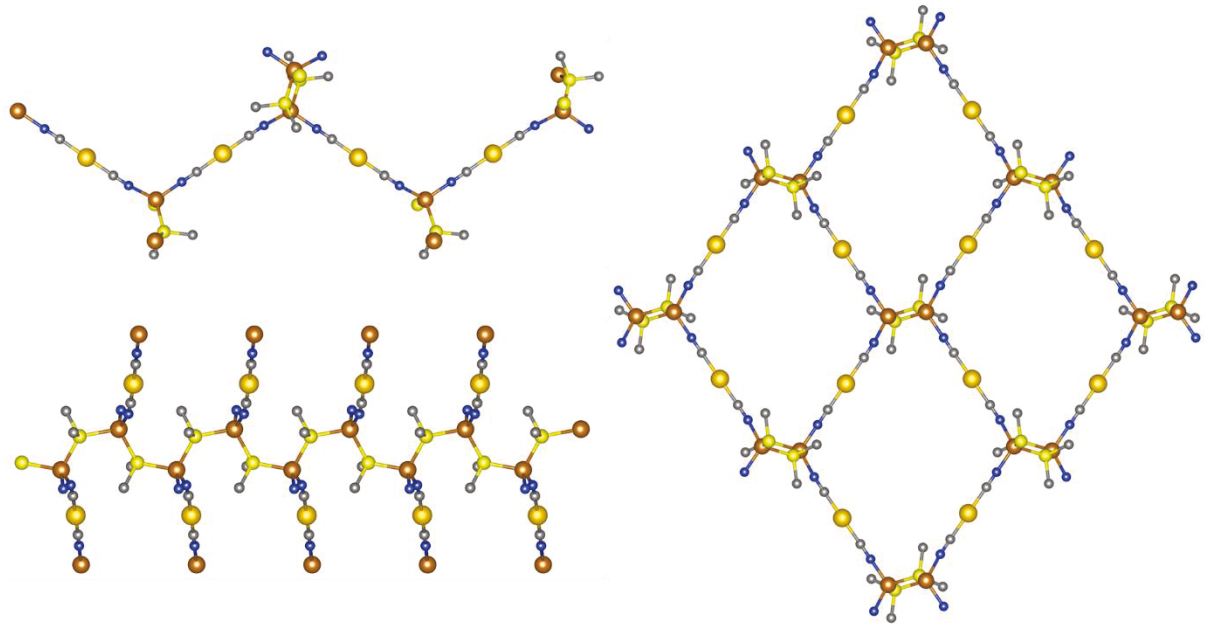

Figure 56. Left (top): X-ray structure of fragments of a $(CuCN)_n$ zigzag chain of $[Cu_{0.5}Au_{0.5}CN(\mathbf{L1})]_n$. Left (bottom): representation of the $(Cu\text{-}S)_n$ chain formed by the **L1** ligand. Right: 3D representation of this coordination polymer. Cu, orange; Au, gold, S, yellow; N, blue; C, grey. The images were reproduced using the cif files from the Cambridge Crystallographic Data Centre; CCDC number: 1537965.

Knorr, Viau and collaborators also reported a coordination polymer obtained upon reacting 2-methyl-1,3-dithiane (**L49**) with CuCN.[17] They obtained a 2D folded layered materials formulated as $[(Cu(\mu_2\text{-}CN)(\mu_2\text{-}\mathbf{L49})]_n$ (**Figure 57**). The folded sheets consist of parallel head-to-tail $[CuCNCuCN]_n$ bridged by parallel **L49** ligands. All Cu(I) centers are tetracoordinated, but the crystal is built upon two crystallographically different copper centers. This coordination polymer is seemingly non-luminescent.

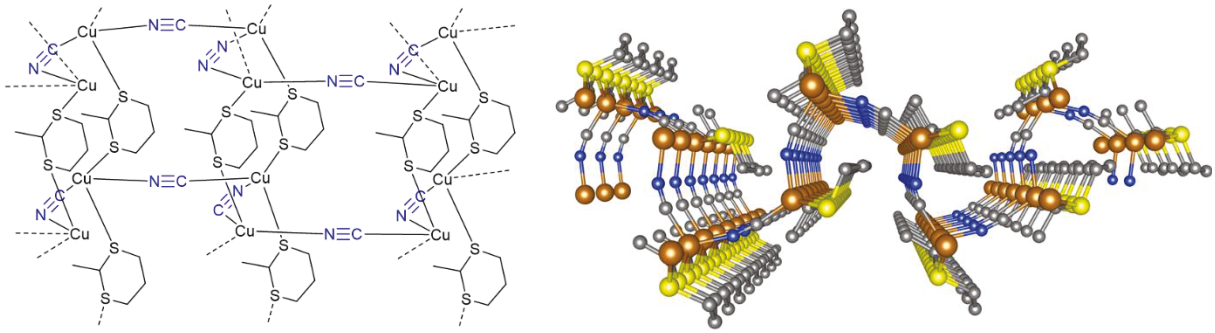

Figure 57. Left: Representation of the folded 2D sheets of [(Cu(μ_2-CN)(μ_2-**L49**)]n. Right: X-ray structure of this polymer. Cu, orange; S, yellow; N, blue; C, grey. The image was reproduced using the cif files from the Cambridge Crystallographic Data Centre; CCDC number: 1888478.

The thiocyanide salt CuSCN has also been used with some thioether ligands, notably Me_2S, Et_2S, *i*Pr_2S and THT (**L1**, **L2**, **L50** and **L3** respectively) to form several coordination polymers, forming 1D zigzag chain, 1D ladder, 1D ladder and 1D zigzag, respectively (**Figure 58**).[84,85] Functional materials built with CuSCN, such as films, are often used as a hole-transporting semiconductor. In a recent study, the treatment of CuSCN films with tetrahydrofuran or acetone leads to films containing crystallites, presumably 1D coordination polymers of large dimensions passivated by the Et_2S at the surface leading to an increase in the hole mobility from 0.01 to 0.05 cm^2/Vs.[86]

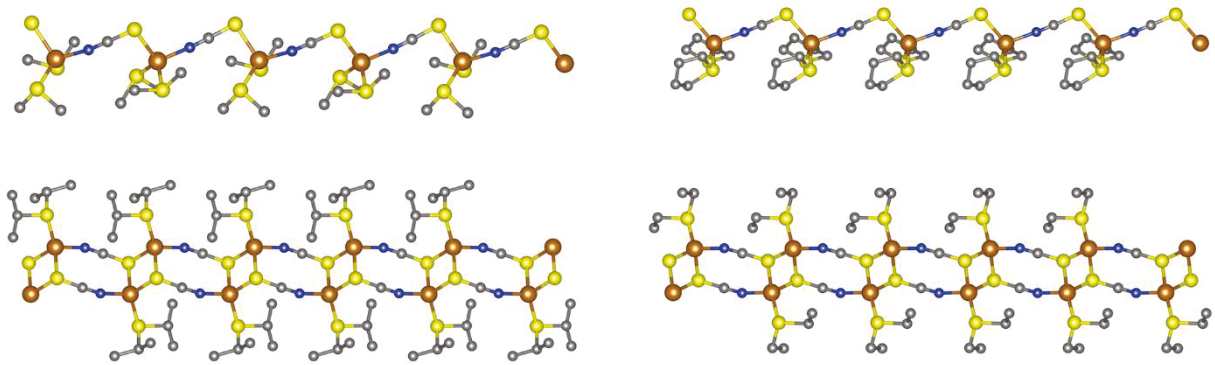

Figure 58. Representative X-ray structure of the 1D zigzag [CuSCN(**L1**)$_2$]$_n$ chain (top left), 1D zigzag [CuSCN(**L3**)$_2$]$_n$ chain (top right), 1D [CuSCN(**L50**)]$_n$ ladder (bottom left) and 1D [CuSCN(**L2**)$_2$]$_n$ ladder (bottom right) coordination polymers. Cu, orange; S, yellow; N, blue; C,

grey. The images were reproduced using the cif files from the Cambridge Crystallographic Data Centre; CCDC numbers: 1460762, 1460763, 1460764, 1460765.

In conclusion, in the light of these past investigations, the construction of globular SBUs commonly encountered with the CuX salts (X = Cl, Br, I) is clearly difficult, not to say illusive, and rather the common $(CuCN)_n$ zigzag chain as the central scaffoldings of the coordination polymers has to be systematically expected. This feature represents the major difference with the halide counterparts.

4. Metal-containing thioether organometallic ligands.

The design of metal-containing ligands is interesting as it provides a supplementary functionality of the resulting material (see sections on conducting materials and DSSCs for examples). However, in the area of chalcogenoether ligands, such endeavor is still in its infancy. In this category, one finds the organometallic ligands (ferrocenyl is an obvious example). For thioether-containing ligands, the earlier works came from Juvenal *et al*. where he designed a series of intensively emissive (*i.e*. the emission quantum yields, Φ_e, vary from 15 to 20%) *trans*-platinum(II)-containing ligands bearing -C_6H_4-SMe end groups (**Figure 59**).[87,88] When reacting with CuX salts (X = Cl, Br, I), these ditopic organometallic ligands (-C≡C-, -SMe) bind the copper atom through the ethynyl donor preferentially. Indeed, the Cu-(η^2-C≡C) coordination linkage is present in all coordination polymers but occasionally, both ethynyl and thioether moieties bind the copper(I) of the SBU resulting into 2D coordination polymers with **L51** and 1D polymer with **L52** (**Figure 60**). This preference maybe due to the presence of a negative charge placed on the ethynyl group.

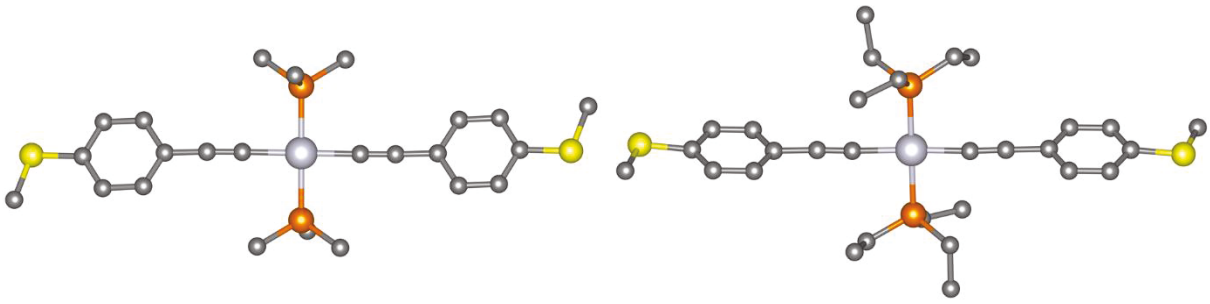

Figure 59. Representative X-ray structure of the Pt-containing dithioether ligands, **L51** (left) and **L52** (right). Pt, silver; S, yellow; P, orange; C, grey. The images were reproduced using the cif files from the Cambridge Crystallographic Data Centre; CCDC numbers: 1521640, 1558597.

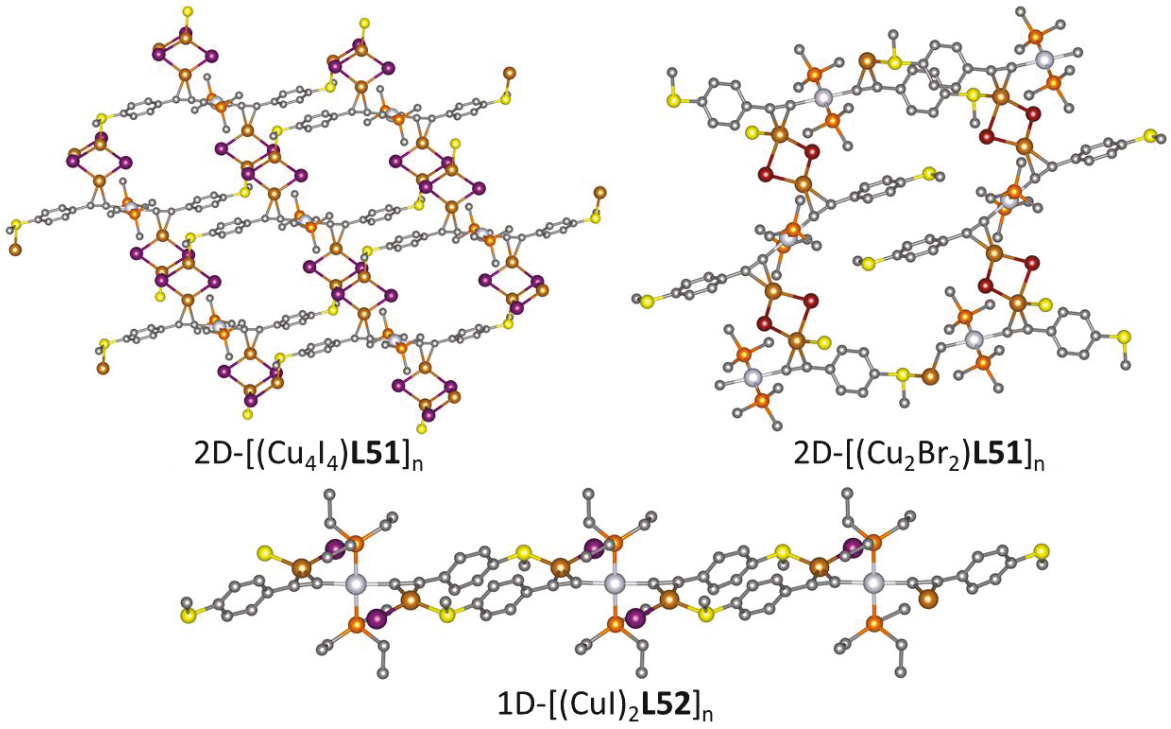

Figure 60. Drawings of the 2D-[(Cu_4I_4)**L51**]$_n$, 2D-[(Cu_2Br_2)**L51**]$_n$ and the 1D-[$(CuI)_2$**L52**]$_n$ polymers. Cu, orange; Pt, silver; I, purple; S, yellow; Br, deep red; P, orange; C, grey. The images were reproduced using the cif files from the Cambridge Crystallographic Data Centre; CCDC numbers: 1521634, 1521639 and 1558592.

The 2D-[(Cu_4I_4)**L51**·solvent]$_n$ coordination polymer, which contains a SBU exhibiting a step staircase geometry, is weakly porous (solvent = MeCN and PrCN, see **Figure 61** for an example of a X-ray structure), which can absorb up to 12.2 cm^3/g (STP) of CO_2 with a surface area of 57.2 m^2/g and a pore volume of 0.019 cm^3/g when solvent = PrCN. The 2D-[(Cu_4I_4)**L51**·MeCN]$_n$ coordination polymers expectedly gives similar data: CO_2 absorption, 16.8 cm^3/g (STP); surface area, 79.5 m^2/g; pore volume 0.027 cm^3/g. Conversely, the rhomboid-containing 2D-[(Cu_2Br_2)**L51**]$_n$ coordination polymers is not porous as its pores are filled with uncoordinated pendent C≡CC_6H_4SMe groups (CO_2 absorption, 1.6 cm^3/g (STP); surface area, 1.7 m^2/g; pore volume < 0.01 cm^3/g). The main feature of these coordination polymers is that they are emissive. For examples at 298 K, λ_{emi} = 568 nm, Φ_e = 15% and τ_e = 2.08 μs for 2D-[(Cu_4I_4)**L51**·PrCN]$_n$, and λ_{emi} = 586 nm, Φ_e = 16% and τ_e = 0.06 μs for 2D-[(Cu_2Br_2)**L51**]$_n$, whereas the data for **L51** are λ_{emi} = 476 nm, Φ_e = 20% and τ_e = 1.11 μs, in the solid state. Moreover, the photophysical

properties of the 2D-[(Cu_4I_4)**L51**·solvent]$_n$ coordination polymers are solvent dependent inside the cavity. For instance, the chromaticity data are (0.43270, 0.44875) and after removing MeCN, they change to (0.42015, 0.38006) and then after reintroducing it from vapor they become (0.44754, 0.42595). The position of λ_{emi} also varies between 15 and 20 nm depending on the solvent vapor. For instance, the 2D-[(Cu_4I_4)**L51**·PrCN]$_n$ coordination polymer exhibits λ_{emi} = 568 nm, but upon removing the solvent under vacuum, the 2D-[(Cu_4I_4)**L51**]$_n$ coordination polymer exhibits λ_{emi} = 583 nm. This behaviour suggests some modest vapo- or solvatochromism. Based on DFT and TDDFT calculations, the nature of the singlet and emissive triplet excited states was addressed. The computational results indicate that it is mainly ππ* with some minor contributions of a MLCT (Cu_4I_4 → **L51**).

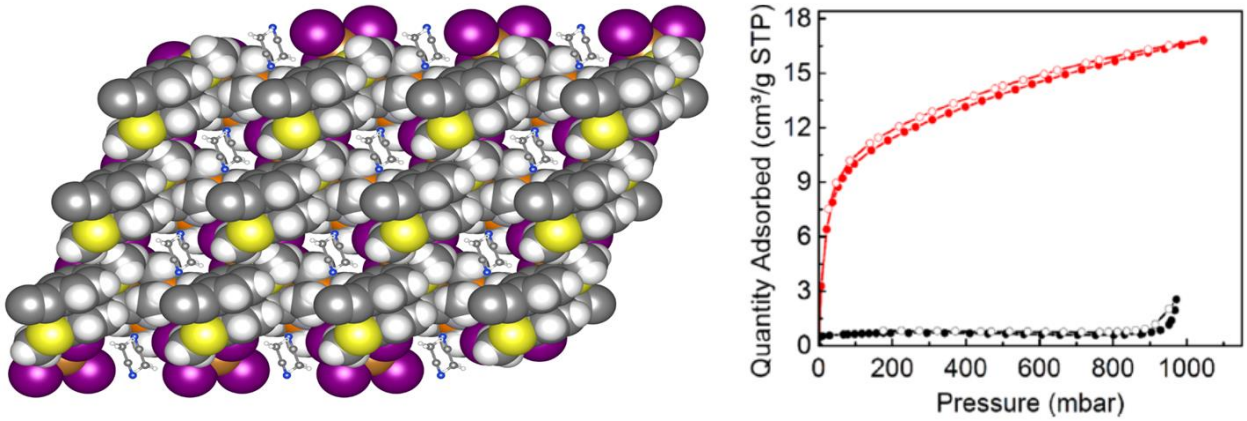

Figure 61. Left: Space-filling view along *b* axis for 2D-[(Cu_4I_4)**L51**•MeCN]$_n$ showing the cavities containing MeCN molecules. Cu, orange; Pt, silver; I, purple; S, yellow; N, blue; P, orange; C, grey; H, white. The image was reproduced using the cif files from the Cambridge Crystallographic Data Centre; CCDC numbers: 1558591. Right: CO_2 (red; at 273 K) and N_2 (black; at 77 K) sorption isotherms for 2D-[(Cu_4I_4)**L51**•EtCN]$_n$ as a representative example. Closed circles = adsorption; open circles = desorption. Adapted with permission from *ACS Omega*, 2017, **2**, 7433–7443. Copyrigth (2017) American Chemical Society.

Although this was not directly addressed in these earlier works, the preference for Cu-(η^2-C≡C) binding over the Cu-S coordination is explained by comparing the results obtained with **L51** and **L52** and the CuI with those collected for the reactivity of this same salt with the related ligand $MeSC_6H_4C{\equiv}CC{\equiv}CC_6H_4SMe$ (**L53**).[89] The resulting non-porous emissive 2D coordination

polymer is of formula $[Cu_4I_4(\mathbf{L53})_3]_n$ (λ_{emi} = 481 nm, Φ_e = 17 % and τ_e = 1.52 (B = 0.0038) and 0.43 μs (B = 0.0034; B being a pre-exponential factor; nature of the excited state is triplet M/XLCT) exhibiting Cu-S coordination bonds only (**Figure 62**). The difference resides in the negative charge bear by the ethynyl segment, thus rendering it a stronger Lewis base.

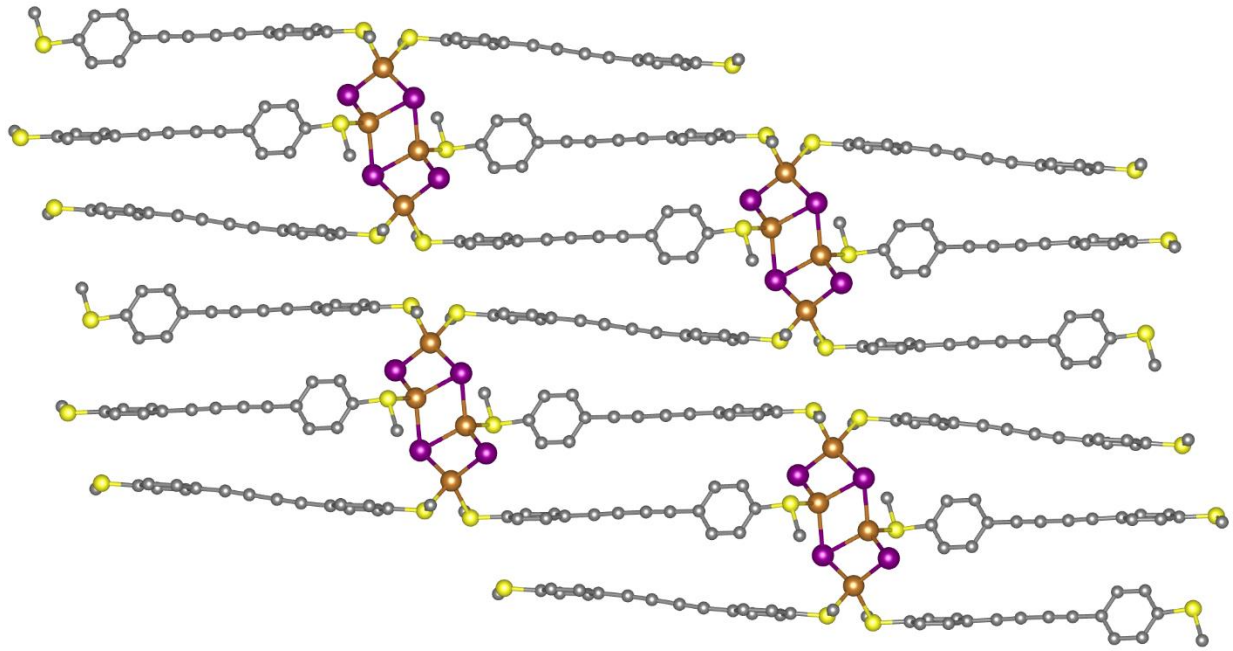

Figure 62. X-ray structure of a layer of the 2D-$[Cu_4I_4(\mathbf{L53})_3]_n$ coordination polymer. Cu, orange; I, purple; S, yellow; C, grey. The X-ray image was reproduced using the cif file provided in supplementary data of ref 89.

Ligand **L51** turned out to be subject to substitution, despite the generally recognized strength of the Pt-CC bond. Indeed, treatment of **L51** with CuCN provokes a CN^- attack onto the Pt(II)-center thus dissociating one $MeSC_6H_4C{\equiv}C^-$, which in turn binds the free copper(I) forming an organometallic coordination polymer formulated as $[Cu(C{\equiv}CC_6H_4SMe)]_n$ (see the 1D-staircase ribbon in **Figure 63**).[90] Concurrently, the newly formed Pt-containing ligand, *trans*-$MeSC_6H_4C{\equiv}CPt(PMe_3)_2C{\equiv}N$ (**L54**), binds the Cu(I) in the zigzag CuCN chain. Notably, no Cu-S bonding was observed in these coordination polymers, stressing the favorable selectivity for the N-containing donor.

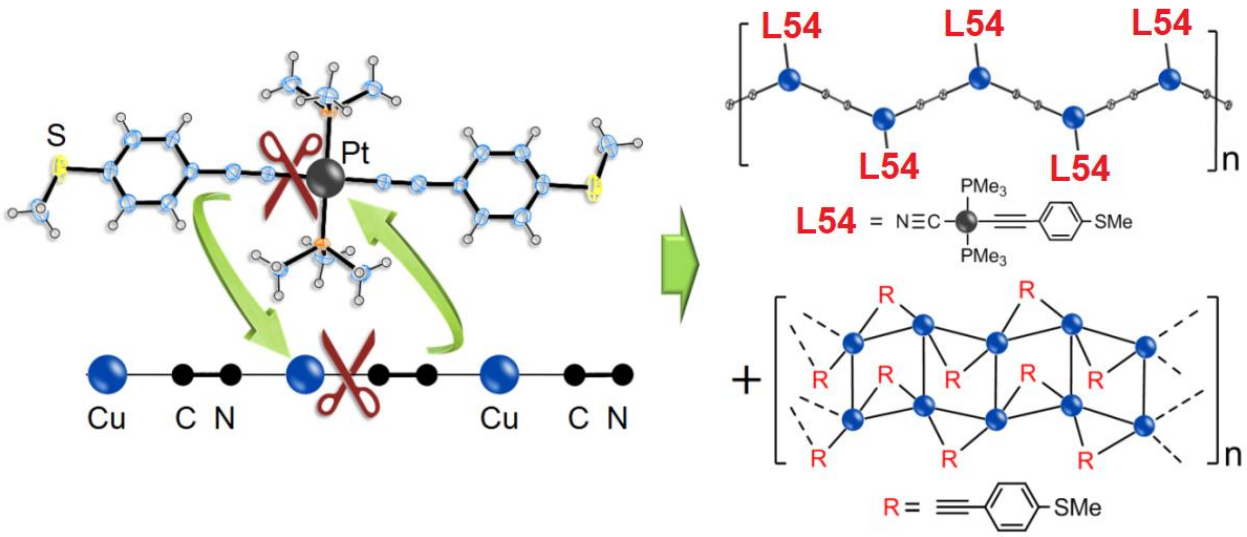

Figure 63. Schematic representation of the reactivity of **L51** with CuCN.

The direct reaction of **L51** with the NaCN salt led to the known complex *trans*-$Pt(PMe_3)_2(CN)_2$ and the salt $[Na^+ {}^-C{\equiv}CC_6H_4SMe]$. Conversely, the reaction of NaCN with the *trans*-$Pt(PMe_3)_2(C{\equiv}CC_6H_4SMe)Cl$ complex led to the formation of tritopic *trans*-$MeSC_6H_4C{\equiv}CPt(PMe_3)_2C{\equiv}N$ ligand **L54**.[91] This latter species reacts with various CuX salts (X = I, CN, SCN) and again the Cu-S bonding is not systematically observed in all three isolated coordination polymers. In the case of the CuSCN salt, an emissive layered coordination polymer formulated as $[(\mathbf{L52})(CuSCN)]_n$ was isolated and characterized. These two latter investigations stressed on the unexpected fragility but convenient variability of the **L51** and **L54** motifs hence providing facile opportunities to design and modulate new metal-containing thioether ligands.

CONCLUSION

Herein a brief outlook of the properties and applications was surveyed. Numerous physical and chemical properties have been studied and exploited, and the most notorious reported property is unambiguously the luminescence. The coordination polymers exhibiting SBUs with *globular* geometry are generally emissive with good intensities (*i.e.* quantum yields from a triplet excited state often characterized as cluster-centered, CC*) and exhibiting an emission band in the vicinity of 600 nm. Conversely, the rhomboid motif and quasi-planar motifs are less emissive as evidenced by the clear paucity of reported emission spectra and related applications.

The second interesting property is the fact that many soluble 0D-complexes and some coordination polymers as pristine thin films are electro-active. This property makes the corresponding coordination polymers suitable for the design of conducting materials and electrocatalysis. Indeed, this survey indicated that this redox activity may stem from either the metal center (Cu(I) ↔ Cu(II) + 1 e^-) or the ligand, and sometimes the halide, which opened the door to the formation of mixed-valent states, and upon suitable stacking in the solid state, to the design of conducting materials upon various doping methods, including subjecting the solid to iodine and bromine vapors for examples. Applications in photonic devices, such as the design of solar cells (*i.e*. DSSCs) and light emitting diodes, were also reported. Concurrently, homogeneous electro-catalytic transformations of some organics were also observed using 0D-complexes.

In parallel, homo- and heterogeneous thermo- and photocatalytic activities have been observed for several coordination polymers and surface-modified nanoparticles. Applications in organic synthesis, notably for the C-N bond coupling reaction, were stressed several times. Interestingly, the photocatalytic degradation of organic pollutants in laboratory conditions was also reported, thus suggesting potential environmental applications.

Several coordination polymers exhibit solid-to-solid phase transitions induced by thermal, mechanical, and vapor treatments. These stimuli-responsive properties were readily detected by the change in their X-ray powder diffraction patterns, but occasionally these phase changes were accompanied by the modification the photophysical properties. These optical processes are respectively referred as thermo-, mechano- and vapochromism. In the latter case, sensing properties were also reported.

The use of copper bromide and iodide salts as reticulation linkers in thioether-containing organic polymers led to the design of self-healing materials where the mechanical properties recovered almost completely after several hours or days upon a complete scission into two parts. This result stresses the basic property of the Cu-X and Cu-S coordination bonds, which are relatively weak and prone to break and reform easily, thus permitting the design of such functional materials. This approach of linking polymer chains through a copper salt, here $CuCl_2$, with ethylene glycol as co-solvent, were also used to auto-assemble the conjugated polymer P3HT in order to improve the charge migration in solar cell through better chain organisation in 3D. However, the data and experimental conditions, based on the literature, suggests the reduction of the Cu(II) ions into

Cu(I), thus favoring the coordination of the soft Lewis base (thiophene) with the softer Lewis acid Cu(I). Concurrently, the use of copper iodide was made to drastically change the properties of a MOF constructed with a rigid dicarboxylate organic ligand, bearing SMe side arms, and Eu^{3+} ions. Upon the coordination of the thioethers to the rhomboid Cu_2I_2 units, a second column is formed, thus rendering the MOF particularly robust, even in boiling water. In addition, this MOF turns out to be electroluminescent (because of the Eu^{3+} ions) which can be tuned to white light emission when using a mixture of Eu^{3+} and Tb^{3+} ions. Furthermore, many studies targeting the cytotoxicity and antibacterial activities of many selone-containing complexes and coordination polymers were undertaken. The highlight is that these properties are comparable to other well-known efficient cytotoxic materials, and applications in cancer therapy are clearly possible. Moreover, there was a clear evidence for surface functionalization of copper salt films or nanocrystals by thioether ligands. However, there was no investigation of similar study concerning selenoethers and telluroethers, thus giving an opportunity to promote surface passivation and stabilisation, and design of novel hole-transporting semiconducting materials. Finally, the design of thioether organometallic ligands has recently been made and 2D coordination polymers with copper salts were prepared and investigated. The key feature is most certainly the high intensity of the resulting emission, and the presence of some porosity of the materials. The area is still in its infancy, and the design of their corresponding functional and smart materials is foreseen.

All in all, the number of reported functional materials based on $Cu_xX_xL_y$ species (L = S-, Se-, Te-containing ligands; X = Cl, Br, I, CN, SCN) is rather large and present a wide scope of applications. The review also implies that there is plenty of room for further developments. Among the modern studies, one finds several designs of robust and functional thin films and one can easily predict that electrochromic films can be fabricated. Moreover, the concept of pre-programming the ligands (*i.e*. rigid ligands that contain both a *hard* and *soft* Lewis bases) to solidify MOFs is quiet appealing when bearing in mind that the synthesis of MOFs can often prove challenging. Similarly, the preparation in a controlled manner of materials containing two different SBUs exhibiting different properties, is yet to be achieved. This could likely be performed by taking advantage of the difference in Cu-S, Cu-Se and Cu-Te bond strengths. Luminescent self-healing materials also offer interesting avenues but would certainly benefit from the incorporation of prefabricated motifs (for example cubane $Cu_4I_4(SR_2)_4$) inside the thioether-containing linear or branched organic polymers, instead of CuI. The use of siloxane as nodes to prepare luminescent or semiconducting sol-gel-

type materials, could also be made.[92] Finally, the high cytotoxicity of many of these materials is also clearly commendable and deserves more developments.

LIST OF ABBREVIATION, ACRONYM AND SYMBOL

°C	degree celsius
0D, 1D, 2D, 3D	Zero Dimensional, One Dimensional, Two Dimensional, Three Dimensional
^{3}CC*	triplet cluster-centered excited state
3-Hptt	5-(pyridin-3-yl)-1H-1,2,4-triazole-3-thiol
Å	Angstrom
AMP	ampicillin
AMX	amoxicillin
ap	anodic peak
Ar	aryl
B	pre-exponential factor
B3LYP	Becke, 3-parameter, Lee–Yang–Parr
BET	Brunauer–Emmett–Teller
Bu	Butyl
CCDC	Cambridge Crystallographic Data Centre
CIE	Commission Internationale de L'Eclairage
CIP	ciprofloxacin
cm	centimeter
CMP	chloramphenicol
COD	coefficient of determination
COSMO	COnductor-like Screening MOde
cp	cathodic peak
CV	cyclic voltammograms
DCM	dichloromethane
DEF	*N*,*N*-diethylformamide
def2-TZVP	Valence triple-zeta polarization
DEp	difference between two peak potentials
DFT	Density-functional theory
DMF	*N*,*N*-Dimethylformamide
DMSO	Dimethyl sulfoxide
DNA	Deoxyribonucleic acid
DSC	differential scanning calorimetry
DSSC	Dye sensitized solar cells
dtpcp	2,11-dithia[3.3]paracyclophane
e^-	electron
$E_{½}$	average potential
*E*a	Anodic potential
e_b	strain at break
EBT	3-ethyl-1,3-benzothiazole-2-thione
EDX	Energy-dispersive X-ray spectroscopy
E_g	Electronic band gap
EG	ethylene glycol
emi	Emission
E_{ox}*	excited state oxidation potential
EPR	electron spin resonance
Et	Ethyl
ET	electron transfer
eV	Electronvolt
exc	Excitation
Fc	Ferrocene
F_e	emission quantum yields
FF	fill factors
FWHM	Full width at half maximum
g	gamma
h	hours

h	Planck constant
IC_{100}	minimum inhibitory concentrations
IC_{50}	half-minimal inhibitory concentration
ICP-AES	Inductively Coupled Plasma Atomic Emission Spectroscopy
*i*Pr	isopropyl
IR	Infrared
J_{SC}	short-circuit current densities
K	Kelvin
L	Ligand
l	wavelength
LED	light emitting diod
M/L	Metal/Ligand
M/XLCT	Metal/halide to ligand charge transfer
Me	Methyl
min	minute
MLCT	metal-to-ligand charge transfer
mM	milimolar
MOF	Metal–organic framework
MPa	Mega Pascal
ms	Micro second
MTT	3-(4,5-dimethylthiazol-2-yl)-2,5-diphenyltetrazolium bromide
n	nu
near-IR	Near-infrared
NHE	Normal Hydrogen Electrode
nm	nanometer
NMR	Nuclear magnetic resonance
OLED	Organic Light-Emitting Diodes
P	Pressure
p	pi
p-	para
P25	Rutile/Anatase: 85/15
P3HT	poly(3-hexylthiophene)
PAND	poly (adipic acid-5-norbornene-2-methyl ester)-(3,6-dioxa1,8-octanedithiol)
PCE	power conversion efficiencies
PCET	proton-coupled electron transfer
PEG	polyethylene glycol
PETD	poly (diethylene glycol divinyl ether)-(3,6-dioxa-1,8-octanedithiol)
PMMA-b-P(MTEA-co-BA)	poly(methyl methacrylate)-b-poly(methyl thioethyl acrylate-co-butylacrylate)
ppm	parts per million
Pr	Propyl
PXRD	powder X-ray diffraction
RDZ	ronidazole
RhB	rhodamine B
RT	Room temperature
S	Siemens
s	conductivity
s_b	fracture stress
SBU	secondary building unit
SCS	piperidine-1-carbodithioate
SEM	Scanning Electron Microscopy
SMA	sulfamethazine
STP	standard temperature and pressure
T	Temperature
TBA	thiobenzamide
t-Bu	*tert*-butyl
TC	tetracycline
TCH	tetracycline hydrochloride
TDDFT	Time dependent density-functional theory
t_e	Emission lifetime
TEM	Transmission Electron Microscop
Temp	Temperature
TFA	trifluoroacetic acid

Tg	glass transition temperatures
TGA	thermogravimetric analysis
THF	tetrahydrofuran
THT	Tetrahydrothiophene
UV-Vis	Ultraviolet-visible
V	volume
V	Volt
V_{OC}	open-circuit voltages
W	Watt
X	Halide (Cl, Br, I)
µm	micrometer

AUTHOR INFORMATION

Corresponding Author

*E-mail: Pierre.Harvey@USherbrooke.ca (P.D.H.)

Orcid

Pierre D. Harvey: 0000-0002-6809-1629

Adrien Schlachter: 0000-0001-5215-8908

Author Contributions

The manuscript was written through contributions of all authors. All authors have given approval to the final version of the manuscript.

Notes

The authors declare no competing financial interest.

Biographies

Adrien Schlachter completed a bachelor's degree in chemistry in 2014 and a master's degree in physical chemistry of interfaces in 2016 at the Université de Bourgogne Franche-Comté, France. He is currently completing a PhD degree in the field of functional polymeric coordination compounds based on copper(I) in Prof. Harvey's group at the U. de Sherbrooke. He won twice best oral presentation at SACIQ (Symposium Annuel de Chimie Inorganique du Québec).

Prof. P.D. Harvey obtained his MSc at the U. de Montréal (1982) and his PhD at McGill U. (1986). He was a NSERC postdoctoral fellow at CalTech (1986-88) and MIT (1988) under the supervisions of Profs H.B. Gray and M.S. Wrighton, respectively. He was appointed assistant professor (1989) and promoted to full professor (1998) at the U. de Sherbrooke (Canada). He awarded a Chaire d'Excellence de Recherche from the ANR (France) held at the U. de Bourgogne, Dijon (2008-10). He serves on the Editorial Boards of the *Journal of Cluster Science* and *Journal of Inorganic and Organometallic Polymers*. He published over 320 research papers and 8 book chapters, and he was awarded the Rio Tinto Alcan Award from the Canadian Society for Chemistry (2013), among many other prizes.

ACKNOWLEDGMENTS

This work was supported by the Natural Sciences and Engineering Research Council of Canada, the Fonds de Recherche du Québec-Nature et Technologies, Compute Canada and Calcul Québec, the Centre Quebecois sur les Matériaux Fonctionnels.

REFERENCES

1 P. C. Ford, E. Cariati and J. Bourassa, *Chem. Rev.*, 1999, **99**, 3625–3648.

2 G. A. Ardizzoia and S. Brenna, *Coord. Chem. Rev.*, 2016, 311, 53–74.

3 J. Conesa-Egea, F. Zamora and P. Amo-Ochoa, *Coord. Chem. Rev.*, 2019, **381**, 65–78.

4 W. Liu, Y. Fang and J. Li, *Adv. Funct. Mater.*, 2018, **28**, 1705593.

5 A. Kobayashi and M. Kato, *Chem. Lett.*, 2017, **46**, 154–162.

6 P. D. Harvey and M. Knorr, *Macromol. Rapid Commun.*, 2010, **31**, 808–826.

7 P. D. Harvey and M. Knorr, *J. Clust. Sci.*, 2015, **26**, 411–459.

8 P. D. Harvey and M. Knorr, *J. Inorg. Organomet. Polym. Mater.*, 2016, **26**, 1174–1197.

9 J. P. Killarney, M. McKinnon, C. Murphy, K. M. Henline, C. Wang, R. D. Pike and H. H. Patterson, *Inorg. Chem. Commun.*, 2014, **40**, 18–21.

10 A. D. Nicholas, F. H. Barnes, D. R. Adams, M. S. Webber, M. A. Sturner, M. D. Kessler, D. A. Welch, R. D. Pike and H. H. Patterson, *Phys. Chem. Chem. Phys.*, 2020, **22**, 11296–11306.

11 M. Johnsson and I. Persson, *Inorganica Chim. Acta*, 1987, **130**, 215–220.

12 B. Norén, Å. Oskarsson, A. Pajunen, M. Tammenmaa and H. V. Volden, *Acta Chem. Scand.*, 1985, **39a**, 701–709.

13 A. Corradi Bonamartini, G. Fava Gasparri, M. Ferrari Belicchi and M. Nardelli, *Acta Crystallogr. Sect. C Cryst. Struct. Commun.*, 1987, **43**, 407–413.

14 A. Serpe, F. Artizzu, L. Marchiò, M. L. Mercuri, L. Pilia and P. Deplano, *Cryst. Growth Des.*, 2011, **11**, 1278–1286.

15 A. Beheshti, W. Clegg, R. Khorramdin, V. Nobakht and L. Russo, *Dalt. Trans.*, 2011, **40**, 2815–2821.

16 S. Mishra, E. Jeanneau, G. Ledoux and S. Daniele, *Inorg. Chem.*, 2014, **53**, 11721–11731.

17 A. Raghuvanshi, M. Knorr, L. Knauer, C. Strohmann, S. Boullanger, V. Moutarlier and L. Viau, *Inorg. Chem.*, 2019, **58**, 5753–5775.

18 M. Knorr, A. Khatyr, A. Dini Aleo, A. El Yaagoubi, C. Strohmann, M. M. Kubicki, Y. Rousselin, S. M. Aly, D. Fortin, A. Lapprand and P. D. Harvey, *Cryst. Growth Des.*, 2014, **14**, 5373–5387.

19 K. M. Henline, C. Wang, R. D. Pike, J. C. Ahern, B. Sousa, H. H. Patterson, A. T. Kerr and C. L. Cahill, *Cryst. Growth Des.*, 2014, **14**, 1449–1458.

20 T. H. Kim, Y. W. Shin, J. H. Jung, J. S. Kim and J. Kim, *Angew. Chemie - Int. Ed.*, 2008, **47**, 685–688.

21 Y. L. Jai, Y. L. So, W. Sim, K. M. Park, J. Kim and S. L. Shim, *J. Am. Chem. Soc.*, 2008, **130**, 6902–6903.

22 J. Troyano, E. Zapata, J. Perles, P. Amo-Ochoa, V. Fernández-Moreira, J. I. Martínez, F. Zamora and S. Delgado, *Inorg. Chem.*, 2019, **58**, 3290–3301.

23 G. Kang, Y. Jeon, K. Y. Lee, J. Kim and T. H. Kim, *Cryst. Growth Des.*, 2015, **15**, 5183–5187.

24 G. N. Liu, R. Y. Zhao, R. D. Xu, X. Zhang, X. N. Tang, Q. J. Dan, Y. W. Wei, Y. Y. Tu, Q. B. Bo and C. Li, *Cryst. Growth Des.*, 2018, **18**, 5441–5448.

25 X. C. Shan, F. L. Jiang, D. Q. Yuan, H. Bin Zhang, M. Y. Wu, L. Chen, J. Wei, S. Q. Zhang, J. Pan and M. C. Hong, *Chem. Sci.*, 2013, **4**, 1484–1489.

26 J. He, J. Huang, Y. He, P. Cao, M. Zeller, A. D. Hunter and Z. Xu, *Chem. - A Eur. J.*, 2016, **22**, 1597–1601.

27 P. van der Sluis and A. L. Spek, *Acta Crystallogr. Sect. A Found. Crystallogr.*, 1990, **46**, 194–201.

28 L. Sarkisov and A. Harrison, *Mol. Simul.*, 2011, **37**, 1248–1257.

29 D. N. Kharitonov, *Russ. J. Coord. Chem. Khimiya*, 1996, **22**, 668–670.

30 T. N. Rostovshchikova, V. V. Smirnov, D. N. Kharitonov and V. B. Rybakov, *Russ. Chem. Bull.*, 1997, **46**, 1736–1740.

31 T. N. Rostovshchikova, V. V. Smirnov and A. I. Kokorin, *J. Mol. Catal. A Chem.*, 1998, **129**, 141–151.

32 V. R. Akhmetova, N. S. Akhmadiev, G. M. Nurtdinova, V. M. Yanybin, A. B. Glazyrin and A. G.

Ibragimov, *Russ. J. Gen. Chem.*, 2018, **88**, 1418–1424.

33 S. Q. Bai, L. L. Koh and T. S. A. Hor, *Inorg. Chem.*, 2009, **48**, 1207–1213.

34 S. Saha, K. Biswas and B. Basu, *Tetrahedron Lett.*, 2018, **59**, 2541–2545.

35 S. Saha, K. Biswas, P. Ghosh and B. Basu, *J. Coord. Chem.*, 2019, **72**, 1810–1819.

36 W. Ji, J. Qu, S. Jing, D. Zhu and W. Huang, *Dalt. Trans.*, 2016, **45**, 1016–1024.

37 C. A. Li, W. Ji, J. Qu, S. Jing, F. Gao and D. R. Zhu, *Dalt. Trans.*, 2018, **47**, 7463–7470.

38 D. Wang, S.-Y. Wu, H.-P. Li, Y. Yang and H. W. Roesky, *Eur. J. Inorg. Chem.*, 2017, **2017**, 1406–1413.

39 R. Y. Zhao, R. D. Xu, G. N. Liu, Y. Sun and C. Li, *Inorg. Chem. Commun.*, 2019, **105**, 135–139.

40 S. Gahlot, E. Jeanneau, F. Dappozze, C. Guillard and S. Mishra, *Dalt. Trans.*, 2018, **47**, 8897–8905.

41 W. Ji, J. Qu, C.-A. Li, J.-W. Wu, S. Jing, F. Gao, Y.-N. Lv, C. Liu, D.-R. Zhu, X.-M. Ren and W. Huang, *Appl. Catal. B Environ.*, 2017, **205**, 368–375.

42 W. Ji, H. Wang, C.-A. Li, F. Gao, Z.-F. An, L. Huang, H. Wang, Y. Pan, D.-R. Zhu, J.-Q. Wang, C. Guo, J. A. Mayoral and S. Jing, *J. Catal.*, 2019, **378**, 270–276.

43 M. Rasouli, M. Morshedi, M. Amirnasr, A. M. Z. Slawin and R. Randall, *J. Coord. Chem.*, 2013, **66**, 1974–1984.

44 P. R. Martínez-Alanis, V. M. Ugalde-Saldívar and I. Castillo, *Eur. J. Inorg. Chem.*, 2011, **2011**, 212–220.

45 C. R. Lucas, W. Liang, D. O. Miller and J. N. Bridson, *Inorg. Chem.*, 1997, **36**, 4508–4513.

46 M. M. Kimani, C. A. Bayse and J. L. Brumaghim, *Dalt. Trans.*, 2011, **40**, 3711–3723.

47 M. Munakata, L. P. Wu, T. Kuroda-Sowa, M. Maekawa, Y. Suenaga and S. Nakagawa, *J. Chem. Soc. Dalt. Trans.*, 1996, 1525.

48 J. Dai, M. Munakata, L. P. Wu, T. Kuroda-Sowa and Y. Suenaga, *Inorganica Chim. Acta*, 1997, **258**, 65–69.

49 J. Troyano, J. Perles, P. Amo-Ochoa, J. I. Martínez, M. Concepción Gimeno, V. Fernández-Moreira, F. Zamora and S. Delgado, *Chem. - A Eur. J.*, 2016, **22**, 18027–18035.

50 J. Troyano, J. Perles, P. Amo-Ochoa, J. I. Martínez, F. Zamora and S. Delgado, *CrystEngComm*, 2014, **16**, 8224–8231.

51 G. Givaja, P. Amo-Ochoa, C. J. Gómez-García and F. Zamora, *Chem. Soc. Rev.*, 2012, **41**, 115–147.

52 M. Moreno-Moreno, J. Troyano, P. Ares, O. Castillo, C. A. Nijhuis, L. Yuan, P. Amo-Ochoa, S. Delgado, J. Gómez-Herrero, F. Zamora and C. Gómez-Navarro, *ACS Nano*, 2018, **12**, 10171–10177.

53 S.-Q. Q. Bai, I. H. K. Wong, N. Zhang, K. Lin Ke, M. Lin, D. J. Young and T. S. A. A. Hor, *Dalt. Trans.*, 2018, **47**, 16292–16298.

54 M. Knorr, F. Guyon, A. Khatyr, C. Däschlein, C. Strohmann, S. M. Aly, A. S. Abd-El-Aziz, D.

Fortin and P. D. Harvey, *J. Chem. Soc. Dalt. Trans.*, 2009, **0**, 948–955.

55 S. Q. Bai, I. H. K. Wong, M. Lin, D. J. Young and T. S. A. Hor, *Dalt. Trans.*, 2018, **47**, 5564–5569.

56 T. Okubo, H. Anma, Y. Nakahashi, M. Maekawa and T. Kuroda-Sowa, *Polyhedron*, 2014, **69**, 103–109.

57 N. Tanaka, T. Okubo, H. Anma, K. H. Kim, Y. Inuzuka, M. Maekawa and T. Kuroda-Sowa, *Eur. J. Inorg. Chem.*, 2013, **2013**, 3384–3391.

58 T. Okubo, N. Tanaka, H. Anma, K. H. Kim, M. Maekawa and T. Kuroda-Sowa, *Polymers (Basel).*, 2012, **4**, 1613–1626.

59 T. Okubo, N. Tanaka, K. H. Kim, H. Yone, M. Maekawa and T. Kuroda-Sowa, *Inorg. Chem.*, 2010, **49**, 3700–3702.

60 J. Zhang, M. Li, L. Cheng and T. Li, *Polym. Chem.*, 2017, **8**, 6527–6533.

61 Y. Liu, H. Peng, P. Wu, H. Liu and J. Zhang, *Polymer (Guildf).*, 2019, **179**, 121616.

62 A. Bonnot, P. L. Karsenti, F. Juvenal, C. Golz, C. Strohmann, D. Fortin, M. Knorr and P. D. Harvey, *Phys. Chem. Chem. Phys.*, 2016, **18**, 24845–24849.

63 A. Bonnot, M. Knorr, F. Guyon, M. M. Kubicki, Y. Rousselin, C. Strohmann, D. Fortin and P. D. Harvey, *Cryst. Growth Des.*, 2016, **16**, 774–788.

64 M. Knorr, A. Khatyr, A. Dini Aleo, A. El Yaagoubi, C. Strohmann, M. M. Kubicki, Y. Rousselin, S. M. Aly, D. Fortin, A. Lapprand and P. D. Harvey, *Cryst. Growth Des.*, 2014, **14**, 5373–5387.

65 M. Knorr, F. Guyon, A. Khatyr, C. Strohmann, M. Allain, S. M. Aly, A. Lapprand, D. Fortin and P. D. Harvey, *Inorg. Chem.*, 2012, **51**, 9917–9934.

66 A. Bonnot, C. Strohmann, M. Knorr and P. D. Harvey, *J. Clust. Sci.*, 2014, **25**, 261–275.

67 F.-H. Lu, M. G. Mohamed, T.-F. Liu, C.-G. Chao and S.-W. Kuo, *RSC Adv.*, 2015, **5**, 87723–87729.

68 M. Mellado, R. Sariego-Kluge, C. González, K. Díaz, L. F. Aguilar and M. A. Bravo, *J. Mol. Struct.*, 2020, **1217**, 128430.

69 M. Panda, T. I. Chandel, M. Kamil and R. H. Khan, *J. Mol. Liq.*, 2020, **306**, 112763.

70 L. J. Fan, J. J. Martin and W. E. Jones, *J. Fluoresc.*, 2009, **19**, 555–559.

71 J. Zhu, R. X. Peng and M. T. Wang, *Gaodeng Xuexiao Huaxue Xuebao/Chemical J. Chinese Univ.*, 2009, **30**, 792–795.

72 A. Schlachter, A. Lapprand, D. Fortin, C. Strohmann, P. D. Harvey and M. Knorr, *Inorg. Chem.*, 2020, **59**, 3686–3708.

73 S. F. Tan and K. P. Ang, *J. Singapore Natl. Acad. Sci.*, 1987, **16**, 111–114.

74 J. T. Guy, J. C. Cooper, R. D. Gilardi, J. L. Flippen-Anderson and C. F. George, *Inorg. Chem.*, 1988, **27**, 635–638.

75 E. W. Ainscough, A. M. Brodie, J. M. Husbands, G. J. Gainsford, E. J. Gabe and N. F. Curtis, *J.*

Chem. Soc., Dalt. Trans., 1985, 151–158.

76 L. R. Hanton, C. Richardson, W. T. Robinson and J. M. Turnbull, *Chem. Commun.*, 2000, 2465–2466.

77 A. Beheshti, E. S. Mousavifard, B. Zargar, P. Mayer and S. E. Rezatofighi, *New J. Chem.*, 2020, **44**, 8520–8537.

78 J. K. Aulakh, T. S. Lobana, H. Sood, D. S. Arora, I. Garcia-Santos, G. Hundal, M. Kaur, V. A. Smolenski and J. P. Jasinski, *Dalt. Trans.*, 2017, **46**, 1324–1339.

79 M. A. Tsiaggali, E. G. Andreadou, A. G. Hatzidimitriou, A. A. Pantazaki and P. Aslanidis, *J. Inorg. Biochem.*, 2013, **121**, 121–128.

80 S. Ahmad, A. Espinosa, T. Ahmad, M. Sohail, A. A. Isab, M. Saleem, A. Hameed, M. Monim-ul-Mehboob and É. D. Las Heras, *Polyhedron*, 2015, **85**, 239–245.

81 Y. Q. Sun, C. K. Tsang, Z. Xu, G. Huang, J. He, X. P. Zhou, M. Zeller and A. D. Hunter, *Cryst. Growth Des.*, 2008, **8**, 1468–1470.

82 E. S. Raper, J. R. Creighton, J. D. Wilson, W. Clegg and A. Milne, *Inorganica Chim. Acta*, 1989, **155**, 77–83.

83 B. R. Varju, J. S. Ovens and D. B. Leznoff, *Chem. Commun.*, 2017, **53**, 6500–6503.

84 P. Pattanasattayavong, D. M. Packwood and D. J. Harding, *J. Mater. Chem. C*, 2019, **7**, 12907–12917.

85 G. Ayala and R. D. Pike, *Polyhedron*, 2016, **115**, 242–246.

86 P. Worakajit, F. Hamada, D. Sahu, P. Kidkhunthod, T. Sudyoadsuk, V. Promarak, D. J. Harding, D. M. Packwood, A. Saeki and P. Pattanasattayavong, *Adv. Funct. Mater.*, 2020, **30**, 2002355.

87 F. Juvenal, A. Langlois, A. Bonnot, D. Fortin and P. D. Harvey, *Inorg. Chem.*, 2016, **55**, 11096–11109.

88 F. Juvenal, A. Bonnot, D. Fortin and P. D. Harvey, *ACS Omega*, 2017, **2**, 7433–7443.

89 A. Bonnot, F. Juvenal, A. Schlachter, D. Fortin and P. D. Harvey, *Chem. Africa*, 2018, **1**, 67–77.

90 F. Juvenal and P. D. Harvey, *J. Inorg. Organomet. Polym. Mater.*, 2020, **30**, 159–168.

91 F. Juvenal, D. Fortin and P. D. Harvey, *Inorg. Chem.*, 2020, **59**, 7117–7134.

92 A. Raghuvanshi, C. Strohmann, J. B. Tissot, S. Clément, A. Mehdi, S. Richeter, L. Viau and M. Knorr, *Chem. - A Eur. J.*, 2017, **23**, 16479–16483.